EFD-475

UNIVERSITY OF TWENTE

Master Thesis

Uncertainty Quantification in Conventional Acoustic Phased Array Beamforming for Aeroacoustic Measurements

MSc Mechanical Engineering — Aeronautics Specialisation

Faculty of Engineering Technology - Department of Thermal and Fluid Engineering

Nikolaos Katsantonis

Enschede, 1^{st} July 2025

Assessment Committee

prof. dr. ir. C.H.Venner
dr.ir. L. Hirschberg
dr.ir. M.P.J. Sanders
dr.ir. Y.H. Wijnant
dr. A.K. Singh

Abstract

This thesis investigated the uncertainty in Conventional Acoustic Phased Array Beamforming (CBF) using the Monte Carlo method. An analytical line source CBF model was made and an experimental CBF case was conducted in the wind tunnel at the University of Twente. Both models focused on uncertainties arising from the microphone phased array, as well as from environmental factors. The experimental case measured the sound power output of the turbulent boundary layer trailing edge noise generated by an airfoil, while the analytical model simulated it. The uncertainties were evaluated by perturbing variables within the beamforming algorithm. The perturbed variables that were related to the microphone array include the microphone phases, microphone sensitivities, microphone coordinates, and the array broadband distance. In addition to the microphone parameters, the environmental factors such as the temperature and the cross correlated spectral signals received from the microphones were also perturbed. The perturbation limits for each variable were defined by the gaussian distributions, which were based on the covariance of each variable. Afterwards, both the analytical and experimental models were simultaneously perturbed across all the variables which were previously mentioned and across a frequency spectrum. The error bounds were then defined around the frequency range, allowing the uncertainty in the beamforming method to be quantified in Sound Pressure Level (SPL) with 95% confidence level both analytically and experimentally.

The analytical studies suggested that the microphone sensitivity was the dominant perturbation mechanism. For sound waves emitted from the trailing edge at 2 kHz, the microphone sensitivity perturbations created a variation by ±0.16 dB in SPL at 10 percent perturbation of the nominal microphone sensitivity. Those were followed by the microphone phase perturbations, which were the second largest contribution of uncertainty to the CBF output. A standard deviation of 10 degree in phase caused a SPL variation by ±0.11 dB. The experimental result of the Thesis showed that the dominant perturbation mechanisms were the Cross Spectral Matrix (CSM) and the array's broadband distance perturbations. For sound waves emitted at 2kHz , for the perturbed CSM, the CBF outputted a SPL variation of ±6.69 dB. By increasing the amount of effective time segments used for the signal processing, it slightly reduced this uncertainty, with the variation decreasing to ±6.58 dB. This study indicated that with increasing the frequency of the sound wave to be analyzed for beamforming led to greater uncertainty in the sound pressure level estimation for both models.

Contents

1 Introduction

Aeroacoustics is the study of sound generated by flow. It combines the fields of aerodynamics and acoustics, and it examines how the pressure perturbations which are caused by sound waves propagate through a fluid medium at a speed c_0, which is dependent on the fluid's local properties. As an airplane flies, a boundary layer of air forms around its surface, there, interactions between the turbulent airflow and the aircraft structure create pressure fluctuations that afterwards they radiate as sound. That acoustic radiation can be captured using microphone phased arrays.

A microphone phased array is a carefully arranged set of microphones which are measuring pressure variations over space and time. Beamforming comes next where it processes that measured signal from the array and enables the generation of acoustic images, which provide insights into the spatial distribution of sound sources in a flow field such as around an aircraft. However, current practices in the Aeroacoustics community widely neglect uncertainty quantification in these measurements. This substantially impacts the confidence of acoustic far field beamforming results.

When using the microphone arrays and the beamforming process, real world, and noisy data must be processed and therefore requires a wind tunnel for the experiment to be conducted in a realistic flow condition. These experiment aims to replicate realistic uncertainty conditions that are very difficult to simulate accurately. The complexity of turbulent flows and that combined to a 3D complex geometry of an airfoil makes analytical approaches alone insufficient for evaluating the confidence and reliability of acoustic beamforming for a practical situation. The experimental data could however validate the computational models and help reduce the gap between them.

Several factors introduce uncertainty into the beamforming analysis, that includes the microphone positioning errors, the calibration inaccuracies of those microphones, the background noise, the flow variability, and the assumptions made to the beamforming algorithm. This paper will make use of an uncertainty quantification approach based on the method proposed by T. Yardibi [26], where uncertainties to those mentioned factors are propagated through the Conventional Beamforming algorithm using a Monte Carlo method. This technique accounts for multi variable uncertainty by consistently perturbing input parameters within defined ranges and applying statistical methods to quantify their impact to the CBF output.

1.1 Research objective

To improve reliability, this project focuses on the uncertainty analysis of the conventional beamforming (CBF) using the Monte Carlo method. This analysis will focus on uncertainties arising from microphone phased array, and on the uncertainties in the determination of integrated sound pressure levels through the source power integration technique used for quantifying sound sources.

A numerical study will first be conducted, incorporating both analytical models and experimental benchmark cases representing typical aeroacoustic measurements to validate the CBF algorithm. An uncertainty analysis framework will then be developed. Following this, an analytical line source CBF model will be made and an experimental CBF case will be conducted in the Aeroacoustics wind tunnel at the University of Twente. Both models will focus on uncertainties arising from the microphone phased array, as well as from environmental factors. The experimental case will measure the sound power output of the turbulent boundary layer trailing edge noise generated by an airfoil model, which is recognized as the dominant acoustic source for airfoils [22] , while the analytical model will simulate it. The uncertainty analysis framework will then be applied to that analytical model and experimental case. Through this work, confidence intervals can be calculated that quantify the uncertainty in microphone phased array measurements.

Ultimately, **The objective of this project is to develop an uncertainty quantification method and tool which will enhance the reliability and credibility of acoustic far-field beam forming results.** Additionally, it will serve as a valuable resource for guiding the design and planning of future experimental campaigns, enabling more informed decisions in planning an experimental approach.

2 Theoretical Background of Phased Array Beamforming

2.1 Time domain Conventional Beamforming

Beamforming is used to localize a sound source in the far field using an array of microphones. For Beamforming in the time domain, a sound source is emitting sound waves in time pressure signal format as seen in figure 1. A grid is constructed around the source location, and based on the time delay of the sound wave that took to reach each microphone, the source can be localized and its amplitude can be defined.

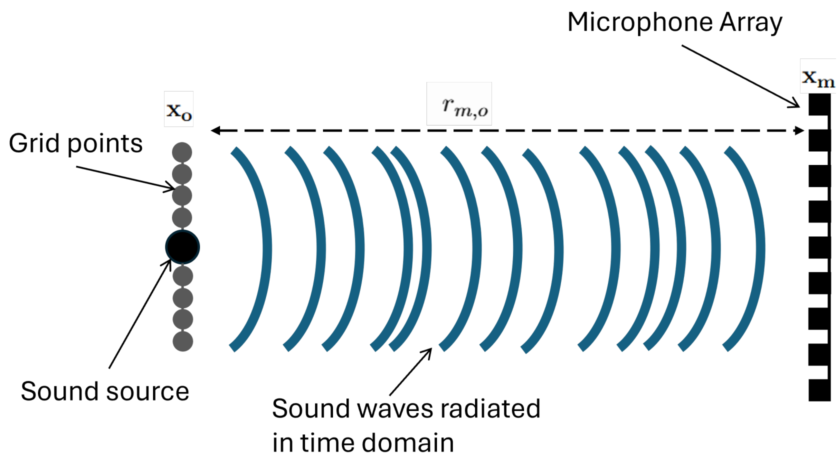

Figure 1: Schematic of Time domain Beamforming

The distance between the microphone coordinates $\mathbf{x_m}$ and the search grid coordinates $\mathbf{x_o}$ is the norm between those 2 vectors:

$$r_{m,o} = ||\mathbf{x_m} - \mathbf{x_o}|| \tag{1}$$

and the time taken for the wave to travel that distance is the distance $r_{m,o}$ divided by the speed of sound. It is also known as the signal delay received by each microphone m:

$$\delta t_{m,o} = \frac{r_{m,o}}{c_0} \tag{2}$$

The source power from the beamforming is expressed as the summation of all time phase shifted microphone signals $p_m(t_m - \delta t_{m,o})$ multiplied by their respective spherical spreading factor as seen in equation 3. The derivation leading to that beamforming equation, has been derived starting from the balance equations in the appendix A.

$$L_{(t,o)} = \sum_{m=1}^{N} v_{m,o} p_m(t_m - \delta t_{m,o}) \tag{3}$$

Where $v_{m,o}$ is the spherical spreading factor, for our case since we want to receive beamforming results to the center of the Acoustic array: $v_{m,o} = \frac{1}{4\pi r_{m,o}}$.

A simple example is created showcasing the time domain conventional beamforming (CBF). The example incorporates 5 microphones receiving each a sinusoidal sound pressure signal varying from -1 to 1 amplitude. The simulated pressure signal from the source without any phase delay is seen in figure 2a. In an ideal situation, each microphone will receive this signal with a unique time delay which is the delay taken for the sound wave to travel from the source to the microphones. By knowing each microphone coordinates $\mathbf{x_m}$ and by creating a 2 dimensional search grid with index notation o, the time shift of each microphone can be found. First by assuming that the sound source lies in that contained area (search grid) with each grid point having coordinates $\mathbf{x_o}$, it is possible to phase shift each received signal. That will lead to ideally align all of the received microphone signals with each other and add them all up by summation as seen in figure 2b.

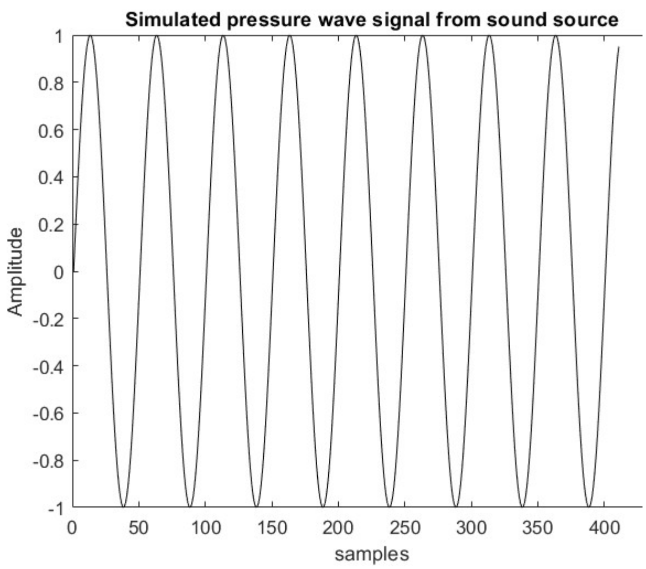

(a) Source pressure signal

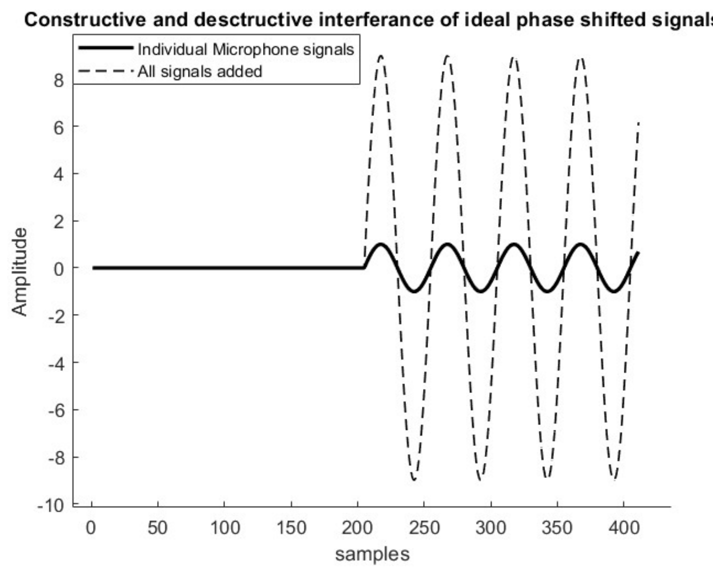

(b) Reconstructed and summed received signal

Figure 2: The time domain pressure signals which are captured by the microphone array are phase shifted and coherently summed, which produces constructive interference in the signal.

As can be seen, the figure 2b shows constructive interference indicating high peaks (high lobes). That will happen only when the correct or the closest selected gridpoint to the actual source location is used as a source location assumption. That leads to all signals aligning nicely. The constructive interference will reach its highest amplitude (all microphone signals nicely aligned) at the actual source location for the CBF output map which is visualised by the contour plot in figure 3b. As can be seen in figure 3b, the simulated source which was given with coordinates: $x = 0.2[m]$, $y = 0.5[m]$ and located $z = 1.3$ meters away from the microphone array is nicely mapped in the CBF output in red which highlights higher magnitude than the blue contour (lower magnitude). The spatial resolution is weak as only 9 microphones have been used in that example.

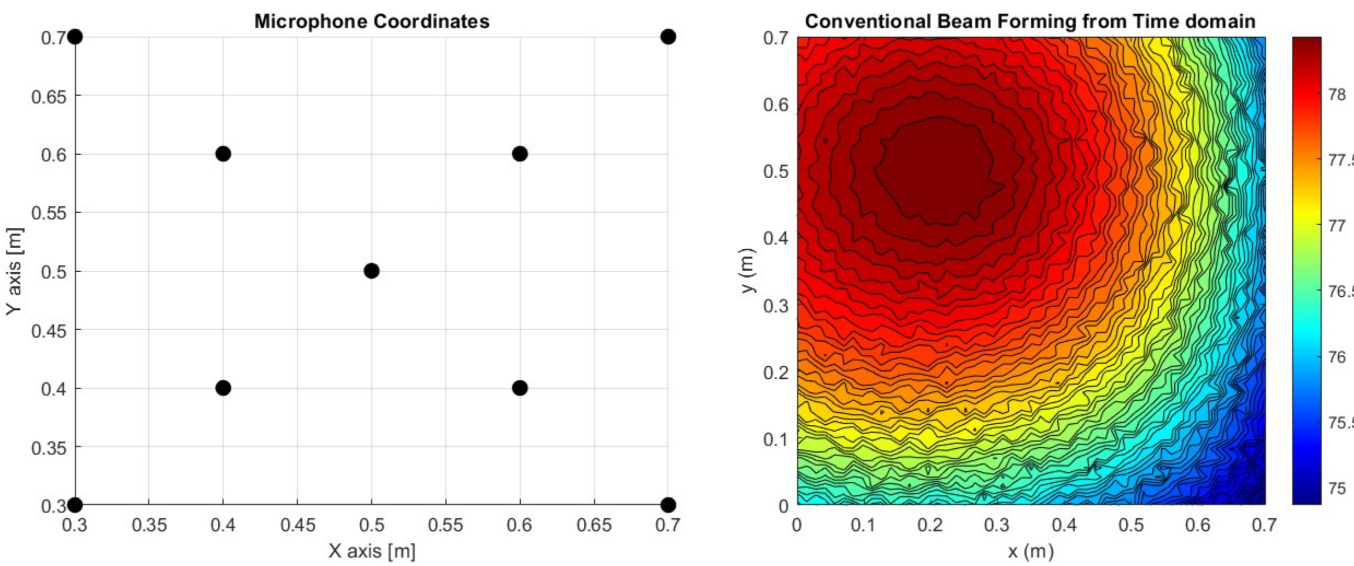

(a) (b)

Figure 3: Figure 3a shows the coordinates of the microphones used while figure 3b shows the Sound pressure level in dB units of the Conventional beamforming from the time domain pressure signal. A main lobe can be seen at x=0.2$[m]$, y=0.5$[m]$, z=1.3$[m]$ which is where the source is simulated to be.

2.2 Frequency domain Conventional Beamforming

Now going to the frequency spectrum. It is beneficial to convert the CBF method to frequency domain as it will reveal more information about the sound source. This would allow to categorize the frequencies of the emitted sound waves and perform CBF for various frequencies of interest as seen in figure 4.

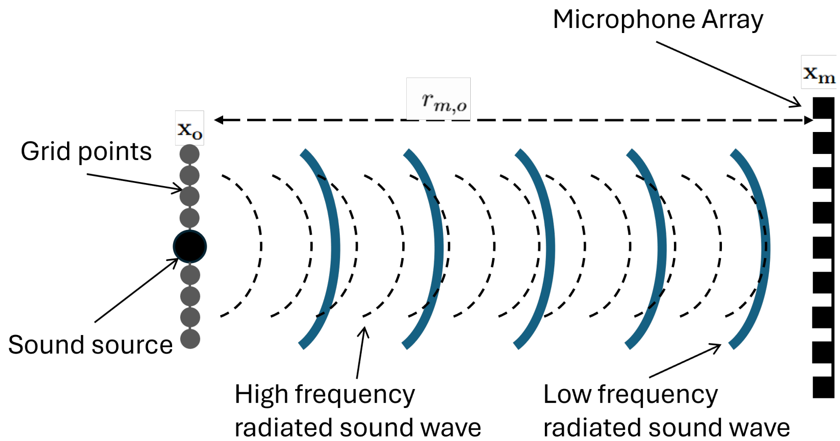

Figure 4: Schematic of Frequency domain Beamforming

To begin with, the same equation as the pressure in time domain is used from equation 2. The time domain equation is then transformed to the frequency spectrum by applying the Fourier transformation as seen in equation 79.

$$Z_o(f) = \sum_{m=1}^{N} v_{m,o} p_m(f) e^{-i\omega\delta t_{m,o}} \tag{4}$$

So far we have the output of the Conventional Beamformer $Z_o(f)$. To get the total power $L_o(f)$ of that output [8]:

$$L_o(f) = \frac{1}{2}|Z_o(f)|^2 = g_{m,o}^{\dagger}(\frac{1}{2}p_m p_m^{\dagger})g_{m,o} \tag{5}$$

Where $g_{m,o}(f)$ is the steering vector which is dependent on both the microphone with index notation m, grid search location with index notation o and on the frequency which the steering vector is operated at. The derivation of that equation can be found in appendix B.

The expression $(\frac{1}{2}p_m p_m^{\dagger})$ is a matrix and is called the Cross Spectral Matrix (CSM) (see equation 6). In the diagonal of the CSM, the auto power spectral is stored. The diagonal terms don't give correlation information between different microphones but only capture the squared magnitude of the resulting complex values (real and phase values of each individual microphone). Therefore the diagonal terms are the terms which capture mostly the background sound including the noise. Later, the diagonal terms will be removed to decrease the noise for both the analytical experimental case models (section 4 and 5 respectively). The off diagonal terms correlate all the possible combinations of the signal pairs received by the microphones. Those terms will be later used along with the steering vector to localize and quantify the sound sources.

$$CSM(f) = \frac{1}{2}\begin{bmatrix} p_1(f)p_1^*(f) & \cdots & p_1(f)p_N^*(f) \\ \vdots & \ddots & \vdots \\ p_N(f)p_1^*(f) & \cdots & p_N(f)p_N^*(f) \end{bmatrix} \tag{6}$$

By applying the steering vectors and the Cross spectral Matrix, the sound power expression is computed as:

$$L_o(f) = g_{m,o}^{\dagger}\ CSM(f)\ g_{m,o} \tag{7}$$

The steering vector captures only the relative phase shifts across the array. For diagonal removal, the steering vector is divided by the term [24]:

$$w_{m,o} = \frac{g_{m,o}}{\sqrt{\left((\sum_{n=1}^{N}|g_{m,o}|^2)^2 - \sum_{n=1}^{N}|g_{m,o}|^4\right)}} \tag{8}$$

Finally to convert the sound power, equations 6 to 8 are all assembled:

$$L_o(f) = w_{m,o}^*(f)CSM(f)w_{m,o}(f) \tag{9}$$

The sound power has units: (pa^2m^2).

The last step is to convert the beamformed expression $L_o(f)$ into sound pressure level (SPL) with decibel units (dB). It is generally preferred to use decibel units as it aligns with human hearing and therefore the CBF output can be easier interpreted. The sound pressure level, which is measured at a distance $R_{0,o}$ from the source is the distance between each grid point with index notation o to the center of all microphone arrays symbolized with index 0. Finally, p_{ref} is the pressure reference which is accounted for $p_{ref} = 2 \cdot 10^{-5}[Pa]$.

$$SPL_o(f) = 20^{10}log\left(\frac{\sqrt{L_o(f)}}{4\pi R_{0,o}}\frac{1}{p_{ref}}\right) \tag{10}$$

2.3 Cross Spectral Matrix with blocks, signal segmentation

In the previous section, the computation of the cross spectral matrix (equation 6) was shown. In this paper, a pressure signal will be used as input to the CSM. However, since the signal varies over time, its time dependent nature introduces uncertainty, and that will affect the accuracy of the beamforming results. To address this, the signal will be segmented in the time domain before being transformed into segments to the frequency domain [26]. By doing that, the covariance of the CSM (discussed later in section 3.2) will be determined and its uncertainty could be quantified. Therefore, in this section a new CSM using time segments will be formulated.

In order to perform a Beamforming, first the microphones record a pressure over a time range. This pressure for each one of those microphones is then converted to the frequency domain by first segmenting the signal into multiple blocks. Each of those blocks represent a time step which represents how the signal progresses over time. This is done to analyse a time unsteady signal. It will be really important for analysing the uncertainty of the Cross spectral matrix with using blocks (sections 4 and 5). Each of those time segments will then be converted to frequency domain by using discrete fourier transform (DFT).

To start with, the length of the window function is computed first by :

$$window\ length = \frac{Signal\ length}{Segments} \tag{11}$$

The window length defines the number of DFT points per time segment used. Afterwards a hanning window is used to that defined window length from equation 11. The hanning window is preferred as it fades in and out the edges of the signal and therefore making less spectral leakage, and leading to better side lobe suppression. An example of a hanning window is visualized in figure 5, with 100 samples.

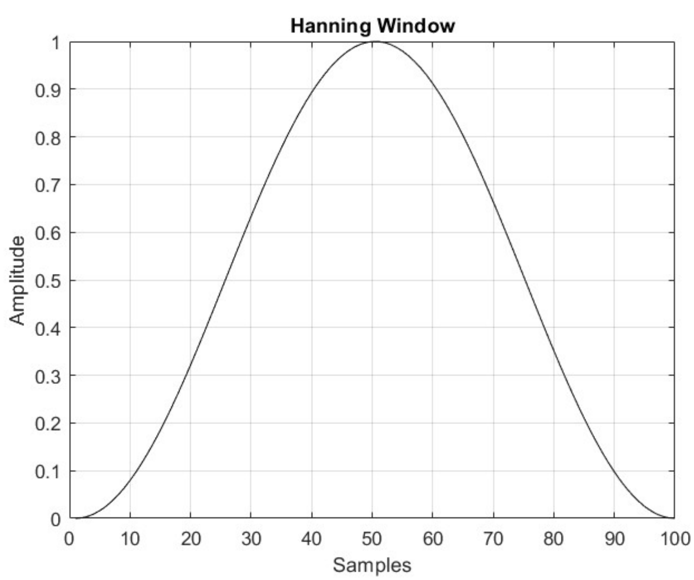

Figure 5: Hanning window example with 100 samples

Once the *window* is computed, it is used to the spectrogram as seen in equation 14.

An overlap is also going to be applied as it is used to ensure continuity between the windows. It improves the time frequency resolution and reduces artifacts. The time segments will incorporate also an overlap and will then be called effective segments. The effective segments are computed as:

$$Effective\ segments = \frac{signal\ length - \overbrace{(v \cdot window\ length)}^{overlap}}{\underbrace{window\ length - (v \cdot window\ length)}_{\tau}} \tag{12}$$

The effective segments will be indexed with the symbol s. In addition, v is the overlap ratio where $v = 0.5$ represents 50 percent of overlap. The more overleap there is, the smoother the transition between the windows ensuring that it will capture also the tapered sections (faded edges) of the window. Finally, as explained the window hopes over the original signal at intervals of τ samples. The more effective segments are used, the less the transformed frequency signal changes between each segment. However the resolution is worse due to the decreased window length per segment. In addition to that, adding more effective segments would make wider frequency bins (larger Δf). That imitatively means worse frequency resolution as can be visualized by the equations below:

$$\Delta f = \frac{fs}{window\ length} \tag{13}$$

Finally, the Short Time Fourier Transform is going to be used using the spectrogram [5] equation:

$$S_{s,m}(f) = \sum_{t=-\infty}^{\infty} p_m(t) window(t - s\tau) e^{-i2\pi ft} \tag{14}$$

where the variable: $window(t - s\tau)$ is the window function being applied to the pressure signal $p_m(t)$ by sliding through it. The window hopes over the signal $p_m(t)$ at intervals of τ samples for each iteration s. The spectrogram (equation 14) is a very important part of this paper as it shows how the beamforming algorithm is performed and analysed through time. The spectrogram is then used in a descritised version of that equation.

As a next step, $S_{s,m}(f)$ is normalized to account for the energy scaling introduced by the window. This is done by dividing the spectra by the total energy of the window and then dividing that by its root mean square (RMS):

$$\hat{S}_{s,m}(f) = \frac{S_{s,m}(f)}{\frac{\sum(window^2)}{RMS(window)}} \tag{15}$$

Next, the cross spectral matrix is formulated with using the STFT values of the pressure signal $\hat{S}_{s,m}(f)$. Since each of those variables contain segmented values s over the time domain, the mean is taken to average all of those effective segments:

$$CSM(f) = \frac{1}{2} \cdot \frac{\sum_{s=1}^{All} \hat{S}_{s,m}(f) \cdot \hat{S}_{s,m}(f)^*}{Effective\ segments} \tag{16}$$

The symbol * indicates the complex conjugate of the variable $\hat{S}_{s,m}(f)$.

2.4 Analytical beamforming, Line source method

In this section an analytical approach will be discussed about simulating a sound source and a microphone response. More specifically, the line source method is going to be applied where a linearly arranged amount of incoherent point sources are equally amplified and distributed along a line. That line will represent a trailing edge airfoil. The line source coordinates are given with vector coordinates $\boldsymbol{\xi} = (\xi, \eta, \zeta)$. In addition, $\xi_l = \zeta_l = 0$ meters and η_l is a column vector with non zero values which forms the line. Each source point is indexed by l.

A schematic example which will be later examined in this section is shown in figure 6.

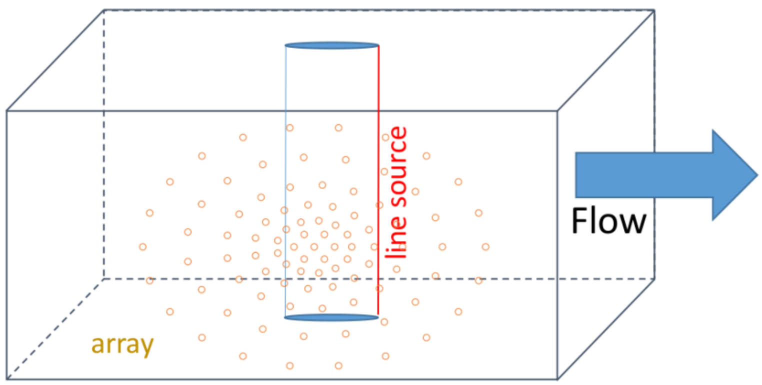

Figure 6: Schematic of Analytical Line source benchmark [24]

To represent those spaced sources, the acoustic pressure $p_m(t)$ is introduced (equation 20). The acoustic pressure formula satisfies the convective wave equation (equation 17) which is the time variant equation from the frequency domain Helmholtz [25] equation.

$$\nabla^2 p - \frac{1}{c}\left(\frac{1}{c}\frac{\partial}{\partial t} + \vec{M}\nabla\right)^2 p = \sigma(t)\delta(\mathbf{x} - \boldsymbol{\xi}) \tag{17}$$

In that equation, $\delta(\mathbf{x} - \boldsymbol{\xi})$ is the Dirac-delta function, k is the wave number and $\sigma(t)$ is the source amplitude.

To simulate the sound wave pressure of each source, a simulated wave will be created:

$$\sigma(t) = acos(2\pi f t) \tag{18}$$

Since the goal is to measure broadband noise coming from a far field, a sum of all frequencies needs to be taken [20], this is visualized with equation 19:

$$\sigma(t-\delta t_{m,l}) = \sum_{j=1}^{F} a_j cos(2\pi f_j(t-\delta t_{m,l})) \tag{19}$$

Where F is the maximum frequency of the broadband noise coming from the source. To simulate the pressure wave traveling all the way through each individual microphones, 3D vectorized sound sources are defined. Each source point location is indexed by l and denoted as vector $\boldsymbol{\xi}_l$. The distance between each sound source and each microphone, indexed by m, is represented by $\tilde{r}_{m,l}$ and is shown in equation 21. It is assumed that the sound propagates through a medium with a uniform flow replicating the wind tunnel flow with velocity and Mach vectors, $\mathbf{U}$ and $\mathbf{M}$ respectively.

For our simplified case, it is assumed that the source amplitude is independent of frequency. All sources are assumed to be distributed along a line and hence are all summed up to obtain the total pressure signal received at each microphone[20]. Therefore, the total pressure simulated and received for each microphone m is visualised with equation 20:

$$p_{m,l}(t) = \sum_{source=1}^{All} \frac{-\sigma(t-\delta t_{m,l})}{4\pi \tilde{r_{m,l}}} \tag{20}$$

where $\tilde{r}_{m,l}$ is:

$$\tilde{r_{m,l}} = \sqrt{\mathbf{M}\cdot(\mathbf{x_m}-\boldsymbol{\xi}_l) + \beta^2\Big((\mathbf{x_m}-\boldsymbol{\xi}_l)^2\Big)} \quad , \qquad \beta = \sqrt{1-norm(\mathbf{M})^2} \tag{21}$$

And $\delta t_{m,l}$ which represents the time delay for a sound wave leaving the source and arriving to each individual microphone is:

$$\delta t_{m,l} = \frac{1}{c\beta^2}\Big(-\mathbf{M}\cdot(\mathbf{x_m}-\boldsymbol{\xi}_l) + \sqrt{\Big(\mathbf{M}\cdot(\mathbf{x_m}-\boldsymbol{\xi}_l)\Big)^2 + \beta^2 r_{m,l}^2}\Big) \quad , \qquad r_{m,l} = ||\mathbf{x_m}-\boldsymbol{\xi}_l|| \tag{22}$$

The pressure wave equation has now been fully defined, as a next step the steering vector will have to be defined. The steering vector $g_{m,o}(f)$ is given as [25]:

$$g_{m,o}(f) = \frac{-e^{-2i\pi f \delta t_{m,o}}}{4\pi \tilde{r_{m,o}}} \tag{23}$$

and for the diagonal removal [24], the steering vector becomes :

$$w_{m,o}(f) = \frac{g_{m,o}}{\sqrt{((\sum_{n=1}^{N}|g_{m,o}|^2)^2 - \sum_{n=1}^{N}|g_{m,o}|^4)}} \tag{24}$$

For the beamforming process, a 3D vectorized search grid is defined, where each point is indexed by o and denoted with vector $\boldsymbol{\xi}_o$. It is assumed that the sound source is located in the region covered by this grid. The distance between each grid point o and each microphone m, is represented by $\tilde{r}_{m,o}$

and the corresponding time delay for a sound wave to travel from each grid point o to microphone m is given by $\delta t_{m,o}$. Both $\tilde{r}_{m,o}$ and $\delta t_{m,o}$ are computed in the same exact way as in equations 21 and 22, respectively. However, instead of using the source location vector $\boldsymbol{\xi}_l$, the grid coordinates $\boldsymbol{\xi}_o$ are used instead.

Next the pressure signal (equation 20) is converted via the SFT technique (equation 14) into frequency domain and in segments. The STFT of the line source is then normalised (equation 15) and is then plugged to equation 16 to form the cross spectral matrix. For the beamforming, the same method as depicted with equation 9 is done by using the steering vector from equation 24, and the cross spectral matrix of the analytical simulation. Finally, the sound power is converted to sound pressure level using equation 10.

An example is constructed using 93 microphones arranged in an array with a diameter of 1.8 meters, the microphone array is based from the research benchmark [24]. A schematic of that example is also shown in figure 6. A total of 20 equally distributed and amplified sources are used to form the line source. In figure 7, it can be seen that a vertically oriented line of discrete sources is detected at the exact coordinates $\boldsymbol{\xi}_l$ as specified ($\xi_l = 0, \zeta_l = 0$ and $-0.8 \leq \eta_l \leq 0.8$). A source amplitude of 1 $[Pa{\cdot}m]$ is used.

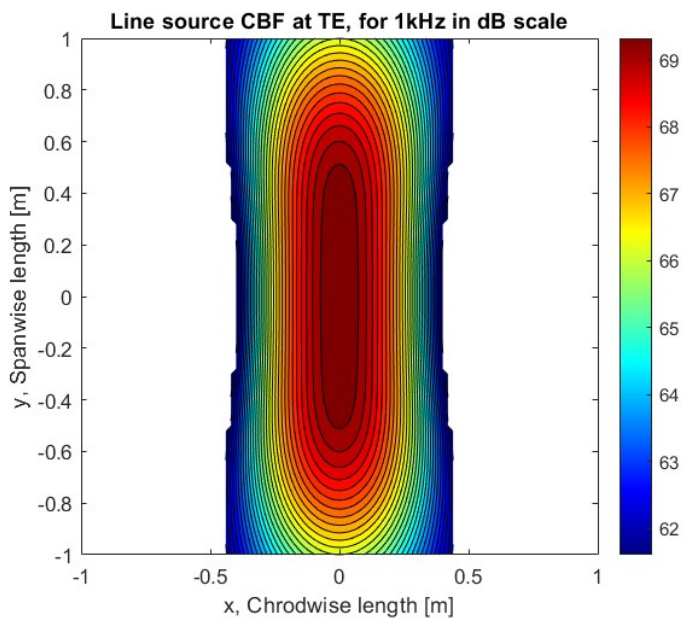

Figure 7: Line source by summation, representing trailing edge noise located at 1 meter from the microphone array for 1 kHz emitted waves.

2.5 Experimental case, beamforming

In this section an Experimental approach will be discussed. More specifically, an airfoil is placed inside a wind tunnel and a flow is simulated to flow around that airfoil. A sound will be emitted from the trailing edge and a microphone array placed in the far field will record its response. Since the objective is to first validate the CBF algorithm before experimenting with new equipment and hence dataset, an experimental benchmark from [24] will be analyzed in this section and validated in section 2.6.2.

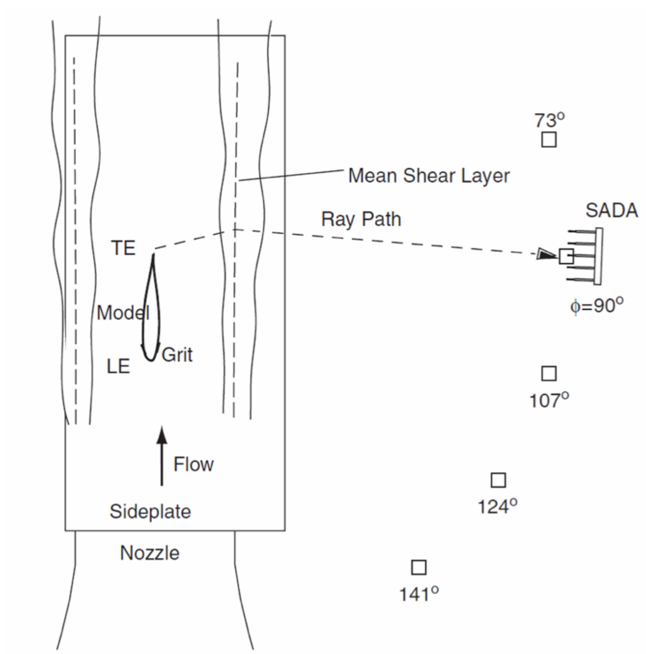

Figure 8: Leading Edge and Trailing edge schematic from NASA 2 Revision benchmark [24].

The beamforming algorithm for this experimental model follows the same steps as described in section 2.3 for computing the cross-spectral matrix. Additionally, equation 9 indicates the method used to determine the sound power and, consequently, the sound pressure level (equation 10). In Equations 82 and 8, for computing the steering vector, the shear layer corrected distances and time delays $R_{a_{m,o}}$ and $\delta t_{amiet_{m,o}}$ respectively should be used in place of $r_{m,o}$ and $\delta t_{m,o}$. Those shear layer corrected distances and time delays can be computed with the equations from the appendix of section C.

An example is constructed using 33 microphones arranged in an array with a diameter of 0.18 meters. The recorded aeroacoustic data is from a NACA 63-215 airfoil with a chord length of 0.406 meters and a span of 0.914 meters, mounted at an angle of attack of $-1.2°$, and tested in a flow at Mach 0.17. This setup is based on the NASA 2 (Revision 2) experimental data benchmark from [24].

In Figure 9, a vertically oriented line source is clearly detected at the exact location of the trailing edge. The airfoil's trailing edge generates sound waves at different frequencies. Figure 9 indicates the CBF output of that test case for emitted sound waves at 4kHz frequency.

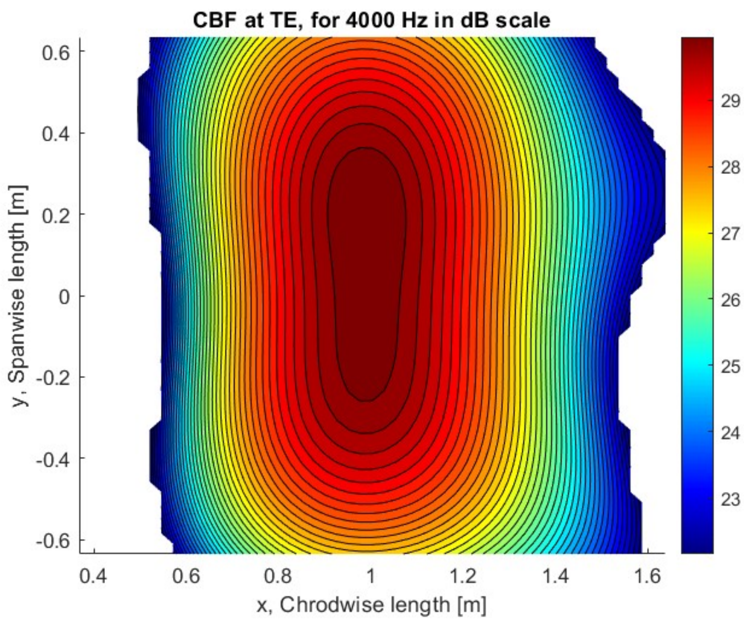

Figure 9: CBF result, indicating the sound source at the trailing edge of a NACA 63-215 airfoil, located 1.524 meters from the microphone array for 4 kHz emitted waves.

2.6 Source power integration

The conventional beamformer is suffering from overlapping main lobes and wide point spread functions, this causes inaccurate estimation of source strength and location in the acoustic map. To reduce the influence of these array induced artifacts and improve spatial resolution, the source power integration method is applied. This approach integrates the estimated acoustic power within a predefined region of interest (ROI) which is approximately where the source region is, leading to a more accurate CBF output.

In this paper, an airfoil will be tested both analytically by applying the line source summation method and experimentally by applying an actual airfoil. Therefore, for both situations, the region of interest would be the trailing edge of the airfoil. The source power integration technique will quantify the total source power over that area of interest (ROI) for a given frequency f.

The integrated sound power P_{int} given by [18], is computed with equation 25. In that equation, the maximum value of the simulated monopole's PSF is normalised and hence taken as one 1, $P_{sim} = 1$ $[Pa^2 m^2]$.

$$P_{int} = \frac{P_{sim} \sum_{r=1}^{G} L_r^{\exp}(f)}{\sum_{r=1}^{G} L_r^{\text{sim}}(f)} \tag{25}$$

where:

$$L_r^{\exp}(f) = \frac{w_{m,r}^{*}(f) CSM(f) w_{m,r}(f)}{4^2 \beta^2 \pi^2 R_{0,r}^2} \tag{26}$$

$$L_r^{\text{sim}}(f) = w_{m,r}^{*}(f) \Big(g_{m,r}(f) g_{m,r}^{*}(f) \Big) w_{m,r}(f) \tag{27}$$

As shown in the source power integration (SPI) equation (equation 25), the SPI technique sums all the sound power within the region of interest. Each gridpoint located in the region of interest is indexed with g while the symbol G represents the total number of gird points inside the ROI. To prevent contributions from source powers associated with side lobes, or sound powers which are significantly lower than the peak sound power in both the simulated and measured CBF outputs, their corresponding sound power levels, will be set to zero. $L_g^{\exp}(f)$ is computed by taking the beamformer output $L_g(f)$ and normalizing it by dividing that term by $4^2 \beta^2 \pi^2 R^2$. The later will remove the distance dependent scaling effect of the array in order to get a more accurate integration.

2.6.1 Source Power Integration, Line source analytical model

For the line source, based on the benchmark from section [24], a region of interest is drawn around the trailing edge, enclosing the majority of the line source in that area, as illustrated in figure 10a. The integrated sound powers within this ROI, converted to sound pressure levels are plotted against their corresponding frequencies to form a power spectral density plot as shown in figure 10b.

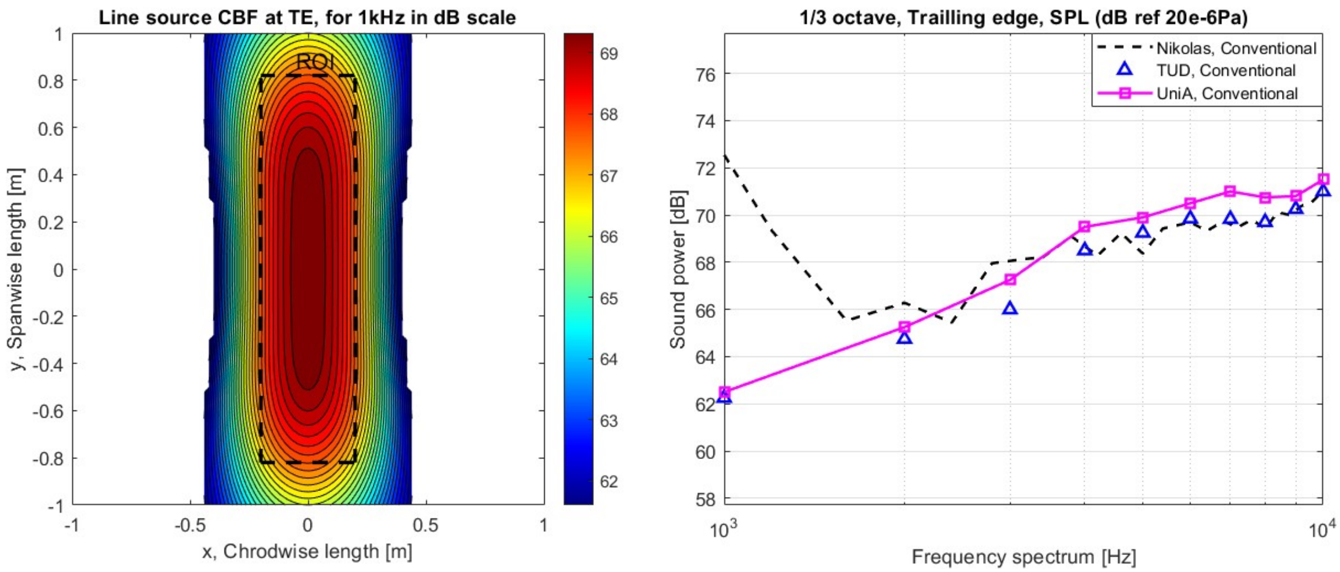

(a) (b)

Figure 10: Figure 10a shows the CBF output of the line source benchmark, where a region of interest is defined around the SPL of the trailing edge. Figure 10b shows the integrated sound power in SPL plotted against its corresponding frequency, forming a power spectral density plot.

As seen from figure 10b, the SPL of the integrated sound power from the analytical Benchmark [24] is computed and compared with TU Delft institution results (TUD, Conventional) and the University of Adelaide along with University of New South Wales, both Schools of Mechanical Engineering (UnIA, Conventional) [23]. The plotted line labeled as "Nikolas, Conventional" represents the SPL computed in this study, based from the line source theory explained in section 2.4. The SPL power from TUD is different by less than 1 dB from the results of Nikolas's study at 2 kHz, this SPL difference decreases as the frequency of the emitted wave increases. Similarly, the data from UniA also aligns well with the SPL from this study for 2 kHz and higher frequency range with approximately 1 dB difference across that frequency range. This study models a discretized amount of sources for computational efficiency to perform the Monte Carlo uncertainty simulation quicker in section 4. In contrast, both TUD and UniA have integrated their line source models by assuming an infinite number of infinitesimal sources distributed along the line. With this approach, TUD and UniA have captured a slightly higher SPL amplitude at frequencies of 3khz and higher. However at lower frequencies, the wavelength is large and hence the beamwidth is also large which causes the discretized model from this study to have the sound field of those sources to overlap with each other, overestimating the SPL to as much as 10 dB at 1 kHz. This overestimation drops quickly with increasing frequency.

2.6.2 Source Power Integration, Experimental Benchmark

For the experimental benchmark based on the NASA 2 (Revision 2) dataset from section [24], a region of interest was defined around the trailing edge, enclosing the majority of the line source in that area, as shown with figure 11a. The integrated sound powers within the ROI were then converted to sound pressure levels and plotted against their corresponding frequencies to form a power spectral density plot as shown in figure 11b.

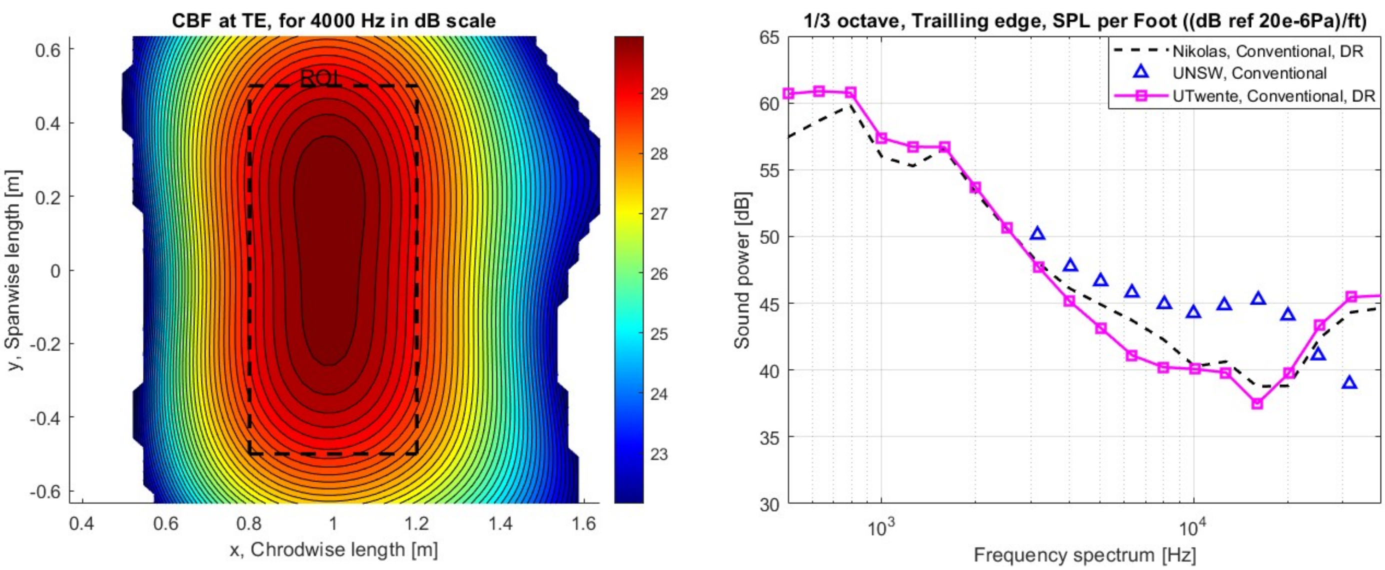

(a) (b)

Figure 11: Figure 11a shows the experimental benchmark based on the NASA 2 (Revision 2) dataset, where a region of interest is defined around the sound pressure level of the trailing edge. Figure 11b shows the integrated sound power in SPL per foot that is plotted against its corresponding frequency, forming a power spectral density plot for the NASA 2 (Revision 2) benchmark.

As shown in figure 11b, the plotted line labeled as "Nikolas, Conventional, DR" represents the SPL per foot from the integrated sound power computed in this study, based from the beamforming theory explained in section 2.5. Another line which is labeled as "UTwente, Conventional, DR" corresponds to results obtained by Dr. Ir. M.P.J. Sanders, Assistant Professor at the University of Twente. The computed results from this study closely enough match the UTwente data, with the SPL being mostly less than 1 dB different across the frequency spectrum. In addition, the data from the University of New South Wales (UNSW) [2] also matches sufficiently enough the SPL computed from this study, with deviations starting at 2.5 kHz and onward with around 3 dB difference. This figure validates the conventional beamforming algorithm used in this study. The difference in SPL between those 3 mentioned studies that occur could perhaps be due to the diagonal removal from the cross matrix used in Utwente and Nikolas (this paper's study) studies. A diagonal removal decreases the background noise and reduces the Sound pressure levels which is also observed in that figure (figure 11b). In addition, the SPL differences could also be in how the cross spectral matrix is computed, which in this study it is computed using time blocks, as discussed in section 2.3.

3 Uncertainty Quantification using the Monte Carlo Method

The Monte Carlo method is used in this paper to quantify the uncertainty of the CBF model. At each Monte Carlo iteration, random inputs are sampled from the standard normal Gaussian distribution and assembled into the matrix $\mathbb{X}$. Those random inputs from the matrix $\mathbb{X}$ are then scaled and dimensionalized for each variable to be perturbed V_{input} from the CBF algorithm by using the covariance matrix of those variables. Those variables which are subject for perturbation are discussed in section 3.1, and the Covariance method is discussed in section 3.2. The resulting perturbed variables V_{input} are then fed into the CBF model. After many iterations and convergence has occurred, the simulation leads to a full output distribution, which leads in capturing the uncertainty of the CBF response. With that approach, the CBF model can be also evaluated under multiple, simultaneously perturbed, nonlinear input variables V_{input}.

This paper uses the normal Gaussian distribution because it is nicely suited for modeling real world phenomena with large data samples. That is according to the Central Limit Theorem [21] which states that the sum of a large number of independent random variables forms a distribution which will get closer and closer to a normal Gaussian distribution, no matter what their original distributions were.

3.1 Input Variables

The input variables that affect beamforming include the cross spectral matrix, microphone locations, temperature, microphone sensitivity, microphone phase, and the array's broadband spacing [26]. These inputs will be examined by perturbing them using the Monte Carlo iteration method. The input variables V_{input} to be analyzed and perturbed are represented as follows:

The microphone position input vector consists of the x,y, and z coordinate values for each of the microphones.

$$\mathbf{V_{x_m}} = [\mathbf{x_1}, ..., \mathbf{x_M}] \tag{28}$$

The microphone phase input matrix consists of an individual phase value to each microphone.

$$V_m^{\text{phase}} = [ph_1 ... ph_M] \tag{29}$$

The microphone sensitivity input matrix consists of an individual sensitivity value to each microphone.

$$V_m^{\text{sensitivity}} = [se_1 ... se_M] \tag{30}$$

For the room temperature input matrix, the matrix is composed of 1 element:

$$V_{Temp} = [T_0] \tag{31}$$

The Array broadband distance input matrix consists of an individual broadband distance value to each microphone.

$$V_m^{\text{array}} = [z_1, ... z_M] \tag{32}$$

For the cross spectral matrix input , since the CSM is already a matrix, its input matrix differs from the others. First, the diagonal elements of the CSM are extracted as input elements. Then, the real parts of the elements from the upper triangular CSM matrix are taken, followed by the imaginary parts of the upper triangular elements. The reason for only considering the upper triangular elements of the CSM is that the CSM is a Hermitian matrix ($CSM = CSM^{\dagger}$). Therefore, the input vector becomes:

$$V_{CSM} = \Big[CSM_{11}, ..., CSM_{MM}, Re[CSM_{12}], ..., Re[CSM_{1M}], ..., Re[CSM_{23}], ..., Re[CSM_{M-1,M}] \tag{33}$$

$$, Im[CSM_{12}], ..., Im[CSM_{1M}], ..., Im[CSM_{23}], ..., Im[CSM_{M-1,M}]\Big] \tag{34}$$

3.2 Covariance matrix and Cholesky decomposition

The variables to be perturbed for the beamforming process have been categorized as uncorrelated and correlated input variables as seen in sections 3.3 and 3.4 respectively. An example of a correlated variable is the cross spectral matrix , where perturbations to one of its non diagonal elements affects the others. This is because the CSM captures the correlation between all microphones, making its components dependent to each other.

On the other hand, uncorrelated input variables include microphone sensitivities and phase responses, since disturbances to each microphone are assumed to be independent. Similarly, variables such as room temperature and array broadband distance are treated as uncorrelated, as they are singular values and not influenced by other parameters. The microphone positions present a more complex case. If one microphone is moved, others in the same branch of the array may also shift, introducing potential correlation. Simulating those kind of dependencies would require to dynamically track the position of each microphone over time, which would significantly increase the model's complexity. To avoid this, the simulation modeled individual microphone position perturbations independently, and therefore it was assumed that the microphone position disturbances to be as uncorrelated. For the uncorrelated variables, a standard deviation will be given initially. This will be used to construct a diagonal covariance matrix, where each diagonal element represents the variance of the corresponding input. The covariance matrix for the uncorrelated perturbed inputs is computed as: $\Gamma_{diagonal} = std_{input}^2$, where std_{input} represents the standard deviation of an input variable.

The situation differs for correlated inputs. As defined in section 3.4, the cross spectral matrix elements to be perturbed are dependent to each other. The CSM elements will be transformed into a full covariance matrix, where the off diagonal elements of the full covariance matrix represent the correlation between element pairs of the CSM, while the diagonal elements of the full covariance matrix represent the variance of each CSM element.

An example of a correlated matrix is given with an example of a variable v constituting of 3 inputs (v_1, v_2 and v_3).

The covariance sample matrix of the variable v becomes:

$$\Gamma = \begin{pmatrix} v_{11} & v_{12} & v_{13} \\ v_{21} & v_{22} & v_{23} \\ v_{31} & v_{32} & v_{33} \end{pmatrix} \tag{35}$$

Each input (element of the covariance matrix, equation 35) is the covariance of 2 elements (element z_{ij} and z_{kj}) of the variable v with index i and k respectively [12]:

$$v_{ik} = \frac{1}{(n-1)} \sum_{j=1}^{n} (z_{ij} - x_i)(z_{kj} - x_k) \tag{36}$$

Here, n is the number of samples used for the covariance elements. In the case of this research, it refers to the number of effective segments of the CSM matrix. Additionally, x_i and x_k represent the mean values of the elements v_i and v_k which are the pair of elements selected for the covariance calculation at indices i and k respectively:

$$x_i = \frac{1}{n} \sum_{j=1}^{n} z_{ij} \tag{37}$$

$$x_k = \frac{1}{n} \sum_{j=1}^{n} z_{kj} \tag{38}$$

The sample covariance matrix captures the relationships between all elements which are included in the matrix V_{input}. To apply this defined correlation structure to the randomly generated inputs $\mathbb{X}$ at each Monte Carlo iteration, the covariance matrix needs to be first decomposed using the Cholesky decomposition [27]. The Cholesky decomposition produces a triangular matrix L as seen from equation 39. It is a simplified form of the covariance matrix Γ and captures the correlations between the elements of the matrix V_{input} to be perturbed.

$$\Gamma = LL^T \tag{39}$$

The Cholesky decomposition is used to impose the desired correlation structure on the inputs from the variable to be perturbed. Random values which are drawn from the standard normal Gaussian distribution are assembled into the matrix $\mathbb{X}$. Those values are generated in MATLAB with mean 0 and standard deviation 1, and they are initially uncorrelated. By multiplying the matrix $\mathbb{X}$ with the Cholesky matrix, the perturbation term is formed. With this, the perturbation term is added to the nominal variable V_{input} to form the perturbed variable V'_{input}. This process is illustrated in Equation 40:

$$V'_{input} = \underbrace{V_{input}}_{nominal\ input} + \underbrace{\mathbb{X}L'}_{perturbation\ term} \tag{40}$$

For each iteration, the simulation computes a perturbed variable V'_{input} and incorporates it as an input variable to the beamforming algorithm. After the simulation has converged, a beamforming output map with all possible variations of sound pressure level SPL'_o is generated.

3.3 Method for Perturbing Variables with Uncorrelated Elements

To analyse the uncertainty of the beamforming algorithm, different types of perturbations are incorporated to the conventional beamforming model. In particular, the temperature which affects the speed of sound and consequently the Mach number, the cross spectral matrix which affects the localization and amplitude of the source. In addition, the microphone phases also affect the localization especially at higher frequencies where phase differences correspond to shorter wavelengths. In addition, the microphones sensitivity is also perturbed as that directly affects the amplitude of the actual source . Finally, the microphones coordinates as well as the array broadband distance will also be perturbed as those variables greatly impact the beamforming output in general. The variables selected for perturbation are divided into uncorrelated and correlated input types. In this section, the uncorrelated input variables will be discussed.

More specifically the:

Temperature:
During the wind tunnel testing, the temperature ranged from 18 to 21 degree. For that reason, a standard deviation of 1 and then of 3 kelvin will be assumed to the uncertainty model. Since the temperature variable consists of only 1 input, the covariance matrix is only consisted of a diagonal where its element is the square root of the mentioned temperature standard deviation. The covariance matrix is then converted using the Cholesky decomposition as explained in section 3.2. Afterwards, a random value within the defined distribution is generated and added with the nominal temperature $V'_{Temp} = \underbrace{V_{Temp}}_{nominal\ value} + \underbrace{\mathbb{X}L'_{Temp}}_{perturbation\ term}$. A perturbed temperature T' for each Monte Carlo iteration is then defined. Afterwards, a 95 percent uncertainty interval is used to define the error bounds around the mean of the perturbed sound pressure level SPL'_o.

Microphone position:
During wind tunnel testing, the microphones vibrated and deviated from their origin due to the flow produced by the wind tunnel. Consequently, the theoretical distances from the microphones origin to the source is not equal to the actual distances of the deviated microphones position to the source during the testing. Therefore, 2 cases will be examined where a standard deviation of 1mm and of 10mm will be introduced to each microphone coordinate as a perturbation input. For the covariance matrix, again only a diagonal will be created as it is assumed that each input (x,y,z coordinates for each of the microphones) is uncorrelated. The process afterwards is explained in section 3.2. Each microphone coordinate is then perturbed for each Monte Carlo iteration and is depicted as: ${\mathbf{V_{x_m}}}' = \underbrace{\mathbf{V_{x_m}}}_{nominal\ value} + \underbrace{\mathbb{X}\mathbf{L'_{x_m}}}_{perturbation\ term}$.

Microphone phase:
A unique random phase is also introduced to each of the microphone signals as part of the variables to be perturbed for the Monte Carlo simulation. Each of the 112 microphones used (see section 5.1) may introduce a small phase delay when receiving a signal. This delay adds up to the phase shift already caused by the varying distances between the sound source and each microphone. For this reason, a phase standard deviation of 1 and later 10 degree will be used for each microphones as input variables to be perturbed. That is modeled by applying random phase shifts to the signal in the frequency

domain, which was previously obtained with equation 15 by converting the time domain signal using a spectrogram. The phase shift is represented as: $e^{i\theta_m}$ and is an element of the input matrix V_m^{phase}. The radian angle θ is the phase angle.

After performing the same process as explained in section 3.2, the signal $\hat{S}_{s,m}$ (from equation 15) with the phase perturbation term $\mathbb{X}L'_{phase_m}$ for each microphone m becomes: $\hat{S}'_{s,m} = \hat{S}_{s,m} \quad \underbrace{\mathbb{X}L'_{phase_m}}_{perturbation\ term}$.

Microphone sensitivity:

The nominal sensitivity of each microphone is around 11.4 mV/Pa [28], that means that if the sound pressure level is 1 pa, the microphone outputs 11.4 mV. However due to manufacturing, calibration, temperature and other situations, the sensitivity of the microphones may be different. To account for this uncertainty, a perturbed sensitivity will be applied to each microphone signal.

The standard deviations to be tested will be 10 and 5 percent of the nominal sensitivity. That accounts to 1.14 and 0.57 mV/Pa respectively.

The perturbed signal $\hat{S}'_{s,m}$, resulting from the microphone sensitivity perturbation term $\mathbb{X}L'_{sensitivity_m}$, is given as:

$$\hat{S}'_{s,m} = \hat{S}_{s,m} \frac{\overbrace{\mathbb{X}L'_{sensitivity_m}}^{perturbation\ term}}{\underbrace{V_m^{\text{sensitivity}}}_{nominal\ value}} \tag{41}$$

This perturbed microphone sensitivity is applied in the Monte Carlo simulation with a different sensitivity assigned to each microphone. That means that there will be 112 input signals for the covariance matrix, each of which is uncorrelated. The process is performed in the same way as to the other perturbations described above.

Array broadband distance:

Similar to the microphone coordinate perturbations, this time only the z axis of the microphone positions is perturbed. That affects the distance from the microphone array to the source. The nominal array broadband distance is 1.801 meters. A standard deviation of 5 and 2.5 percent of the nominal array broadband distance will be used. That corresponds to 90 and 45 mm respectively.

Each microphone z axis coordinate is then perturbed for each Monte Carlo iteration as shown: $V'_{array_m} = \underbrace{V_m^{\text{array}}}_{nominal\ value} + \underbrace{\mathbb{X}L'_{array_m}}_{perturbation\ term}$.

3.4 Method for Perturbing Variables with Correlated Elements

The cross spectral matrix, is the only considered correlated input variable.

Cross spectral matrix:
The cross spectral matrix is harder to perturb as it is derived from the spectrogram (equation 15).That being said, the spectrogram transforms the signal into the frequency domain, where it is represented over a wide range of frequencies. For each frequency, the signal is divided into time segments (effective segments). By applying the beamforming to each of those time segments separately, it becomes clear that the results of the beamforming vary over time segment. That makes the beamforming output to be a time dependent uncertainty. To measure the uncertainty of that variation, a covariance matrix is constructed by applying and relating all the elements of the cross spectral matrix as explained also in section 3.2. Each of the CSM elements are spectra between microphones and hence they are dependent to each other. Therefore the Covariance matrix will be consisted of both diagonal and off diagonal terms. The amount of effective segments used determines the amount of samples to be used for each element of the covariance matrix. This is called a Sample Covariance matrix.

The sample covariance matrix contains estimation errors. Ledoit and Wolf [15] suggest using the matrix obtained from the sample covariance matrix through a transformation called shrinkage. This results in getting the most extreme coefficients towards more central values, therefore it reduces the estimation error where it is very important. The paper of Ledoit and Wolf describe the optimal shrinkage intensity and they give the formula (see equation 42). The shrinking method applied is called the Ledoit Shrinkage.

Ledoit gives an expression for the shrinkage of the Covariance matrix which is defined as:

$$\Gamma_{Shrink} = \hat{\delta}^{*} F + (1 - \hat{\delta}^{*})\Gamma_{CSM} \tag{42}$$

In order to solve the above expression, many terms first need to be addressed. Those terms have already been derived and therefore only their final form will be given in this paper.

Starting first with the Shrinkage intensity $\hat{\delta}^{*}$, Ledoit proposes:

$$\hat{\delta}^{*} = max\{0, min\{\frac{\hat{\kappa}}{eff\ segm}, 1\}\} \tag{43}$$

This is just to assure that $\frac{\hat{\kappa}}{eff\ segm}$ is always within 0 and 1. The consistent estimator for $\hat{\kappa}$ is related to the consistence estimators $\hat{\gamma}$ and $\hat{\rho}$ as:

$$\hat{\kappa} = \frac{\hat{\pi} - \hat{\rho}}{\hat{\gamma}} \tag{44}$$

Those consistent estimators are equal to:

$$\hat{\pi} = \sum_{i=1}^{N}\sum_{j=1}^{N}\hat{\pi}_{ij} \tag{45}$$

where

$$\hat{\pi}_{ij} = \frac{1}{eff\ segm}\sum_{s=1}^{eff\ segm}\{(V_{CSM_{i,s}} - \overline{V_{CSM_i}}.)(V_{CSM_{j,s}} - \overline{V_{CSM_j}}) - \Gamma_{CSM_{i,j}}\}^2 \tag{46}$$

$eff\ segm$ is short for total effective segments. $V_{CSM_{i,s}}$ is the input variable containing as inputs the elements of the CSM matrix to be sampled for the covariance. The overline symbol represents the mean of the variable overlined with respect to the amount of effective segments. For instance, $\overline{V_{CSM_j}}$ is the mean of the variable $V_{CSM_{j,s}}$. The index of the elements of the covariance sampled matrix is denoted as i and s is the effective segment index. In addition, $\Gamma_{CSM_{i,j}}$ is an element of the sample covariance matrix of CSM.

The consistent estimator $\hat{\rho}$ is equal to:

$$\hat{\rho} = \sum_{i=1}^{N}\hat{\pi}_{ii} + \sum_{i=1}^{N}\sum_{j=1,j\neq i}^{N}\frac{\overline{r}}{2}\left(\sqrt{\frac{\Gamma_{CSM_{j,j}}}{\Gamma_{CSM_{i,i}}}}\hat{\theta}_{ii,ij} + \sqrt{\frac{\Gamma_{CSM_{i,i}}}{\Gamma_{CSM_{j,j}}}}\hat{\theta}_{jj,ij}\right) \tag{47}$$

where $\hat{\theta}_{ii,ij}$ and $\hat{\theta}_{jj,ij}$ elements contained in the consistent estimator $\hat{\rho}$ are:

$$\hat{\theta}_{ii,ij} = \frac{1}{eff\ segm}\sum_{s=1}^{eff\ segm}\{(V_{CSM_{i,s}} - \overline{V_{CSM_i}})^2 - \Gamma_{CSM_{i,i}}\}\{(V_{CSM_{i,s}} - \overline{V_{CSM_i}})(V_{CSM_{j,s}} - \overline{V_{CSM_j}}) - \Gamma_{CSM_{i,j}}\} \tag{48}$$

and

$$\hat{\theta}_{jj,ij} = \frac{1}{eff\ segm}\sum_{s=1}^{eff\ segm}\{(V_{CSM_{j,s}} - \overline{V_{CSM_j}})^2 - \Gamma_{CSM_{j,j}}\}\{(V_{CSM_{i,s}} - \overline{V_{CSM_i}})(V_{CSM_{j,s}} - \overline{V_{CSM_j}}) - \Gamma_{CSM_{i,j}}\} \tag{49}$$

Finally, the consistent estimator $\hat{\gamma}$ is given as:

$$\hat{\gamma} = \sum_{i=1}^{N}\sum_{j=1}^{N}(f_{ij} - \Gamma_{CSM_{i,j}})^2 \tag{50}$$

$\overline{r}$ is the sample correlation and is expressed as:

$$\overline{r} = \frac{2}{(N-1)N}\sum_{i=1}^{N-1}\sum_{j=i+1}^{N}\frac{\Gamma_{CSM_{i,j}}}{\sqrt{\Gamma_{CSM_{i,i}}\Gamma_{CSM_{j,j}}}} \tag{51}$$

Then the shrinkage target F is defined as the matrix F which is basically a sample constant correlation matrix. f_{ii} elements denote its diagonal and represent the sample variances:

$$f_{ii} = \Gamma_{CSM,ii} \tag{52}$$

and the off diagonal elements: f_{ij} represent its average sample correlation:

$$f_{ij} = \bar{r}\sqrt{\Gamma_{CSM_{i,i}}\Gamma_{CSM_{j,j}}} \tag{53}$$

Where $\Gamma_{CSM,ii}$ are the diagonal elements of the sample covariance matrix Γ_{CSM}. After this process has been performed, the shrank sampled covariance matrix Γ_{Shrink} is defined. This method minimizes errors to that uncertainty estimation.

While performing this process, it is important to note that the covariance matrix only consists of real numbers. The elements of the cross spectral matrix used as inputs of the variable V_{CSM} to construct the covariance matrix are extracted as real values $\mathbb{R}$, specifically $Re[V_{CSM}] \in \mathbb{R}$ and $Im[V_{CSM}] \in \mathbb{R}$. After its construction, it is shrank as shown above and then decomposed using the Cholesky decomposition method. During each Monte Carlo iteration, a random value is used to scale the decomposed triangular matrix L'_{CSM}.

The perturbed CSM is computed as $V'_{CSM} = \underbrace{V_{CSM}}_{nominal\ value} + \underbrace{\mathbb{X}L'_{CSM}}_{perturbation\ term}$.

Afterwards, during the reconstruction of the perturbed cross spectral matrix V'_{CSM} in the original $M \times M$ form (M representing the total amount of microphones used), the imaginary components are multiplied by the imaginary unit i, while the real parts are preserved. The real and imaginary parts are then summed together to reconstruct the complex elements of the perturbed CSM.

3.5 Monte Carlo Convergence

For the Monte Carlo simulation, a fixed number of iterations will be used for each different perturbation input variable into the CBF model. To determine if the amount of Monte Carlo iterations is sufficient enough, the standard deviation divided by the mean of the computed perturbed sound pressure levels at the source location is evaluated. The model will be evaluated at increasing iteration counts, starting from 10 iterations and continuing in steps of 10 up to 1000 iterations. As the amount of iterations is increased, if the standard deviation over the mean no longer show significant changes, it will indicate that the number of iterations is sufficient enough.

3.6 Uncertainty interval of Monte Carlo Simulation

After the Monte Carlo simulation is completed, the CBF outputs of all iterations are processed to define the uncertainty interval of the perturbed sound pressure level SPL'_o. An aleatoric uncertainty approach will be used in this work [17]. Aleatoric uncertainty is a type of uncertainty that comes from natural randomness in the system's output, in our case that is the the perturbed sound pressure level SPL'_o. This type of uncertainty cant be decreased or removed by having more data, but what can change is that its estimation could become more stable with an increased number of simulation iterations. The uncertainty interval (see equation 54) derived from this aleatoric uncertainty approach quantifies the range in where the output is expected to fall, given the randomness in the inputs. For most experimental methods, using 95% confidence is generally considered sufficient and therefore to be used in this paper [26]. That means that there is a 95 % chance that the CBF output to fall in that band region. Finally, this interval visualizes the spread of possible CBF outcomes from the perturbed variables used in the Monte Carlo.

$$95\% U_b = \mu(SPL'_o) \pm t std(SPL'_o) \tag{54}$$

where $std(SPL'_o)$ is the standard deviation of the perturbed sound pressure level SPL'_o computed after performing several Monte Carlo iterations. In addition, looking to the above equation, t is the critical value which is multiplied by the standard deviation in order to form the uncertainty bound. Also, μ is the mean from all Monte Carlo iterations of the perturbed sound pressure level SPL'_o. To define the critical value t, the standard normal distribution p_y [11] needs to be plotted using equation 55:

$$p_y = \frac{1}{std\sqrt{2\pi}} e^{-\frac{(x-\mu)^2}{2std^2}} \tag{55}$$

Figure 12a shows the standard normal distribution using equation 55. For a two tailed 95 % uncertainty interval, the critical value t corresponds to the normal distribution curve where 97.5 % of the total area lies to the left [4]. Next, a numerical Matlab function that computes the area of 97.5 percent from the figure is applied. Applying the Matlab function: norminv(97.5%), the value of t is found to be 1.96 standard deviations as seen from figure 12b.

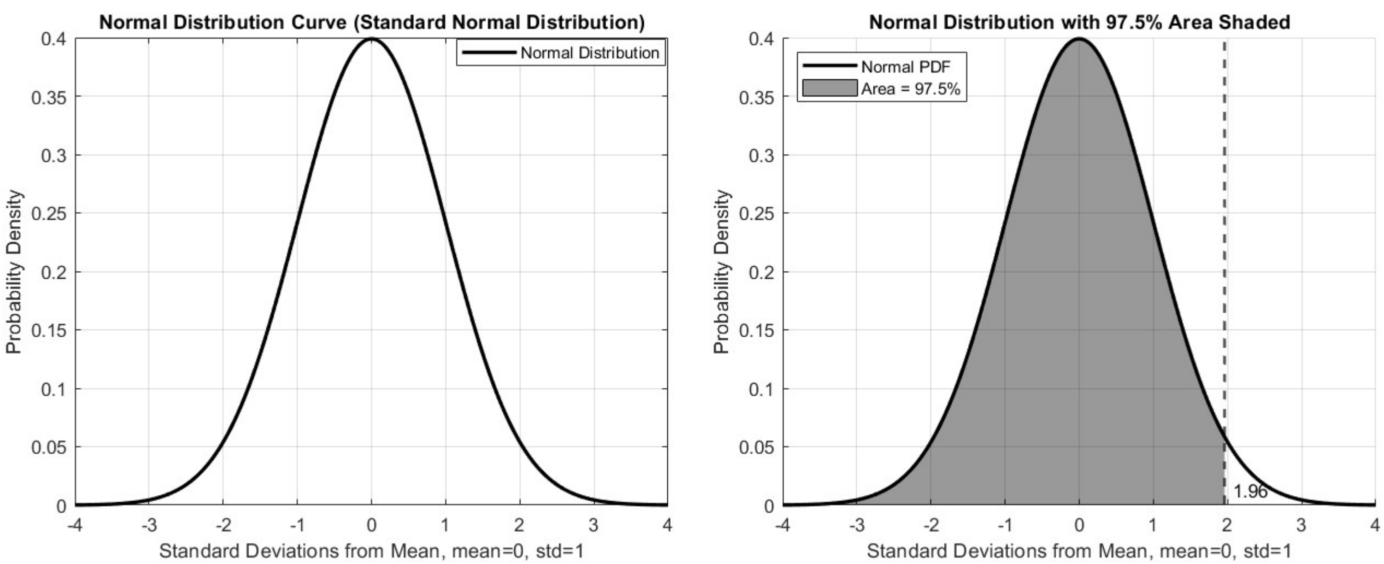

(a) Normal distribution curve

(b) Critical value t defined with Norminv function

Figure 12: Figure 12a shows the normal distribution density curve against the standard deviation. Figure 12b shows again the normal distribution density against the standard deviation at 97.5 percent of the area using the Matlab function Norminv.

Hence the uncertainty interval equation becomes:

$$95\% U_b = \mu(SPL'_o) \pm 1.96 std(SPL'_o) \tag{56}$$

3.7 Uncertainty Schematic Summary

Figure 13 visualizes the total process for an uncorrelated input variable to be perturbed while figure 14 visualizes the total process for a correlated input variable to be perturbed.

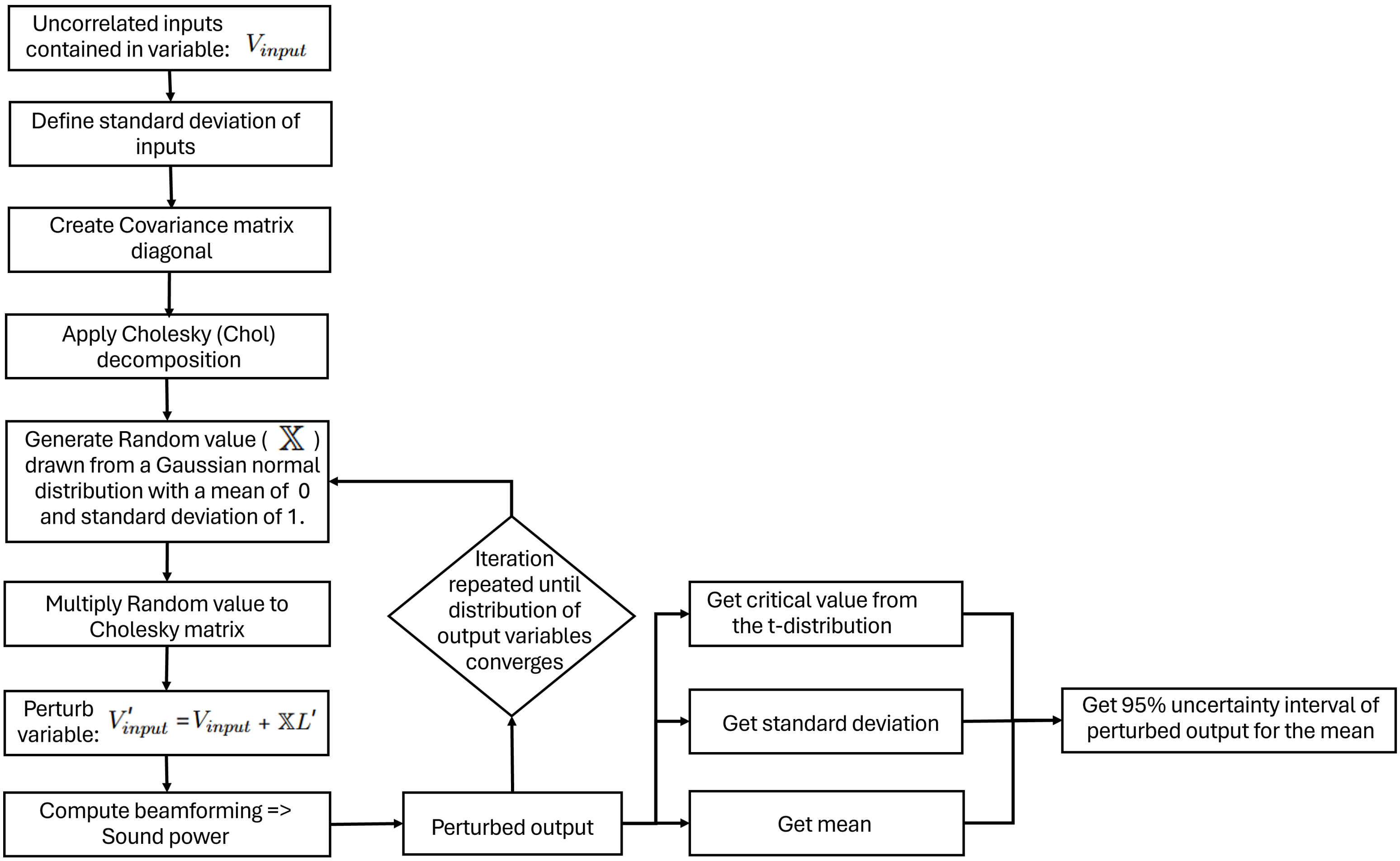

Figure 13: Monte Carlo model in Matlab for uncorrelated variables

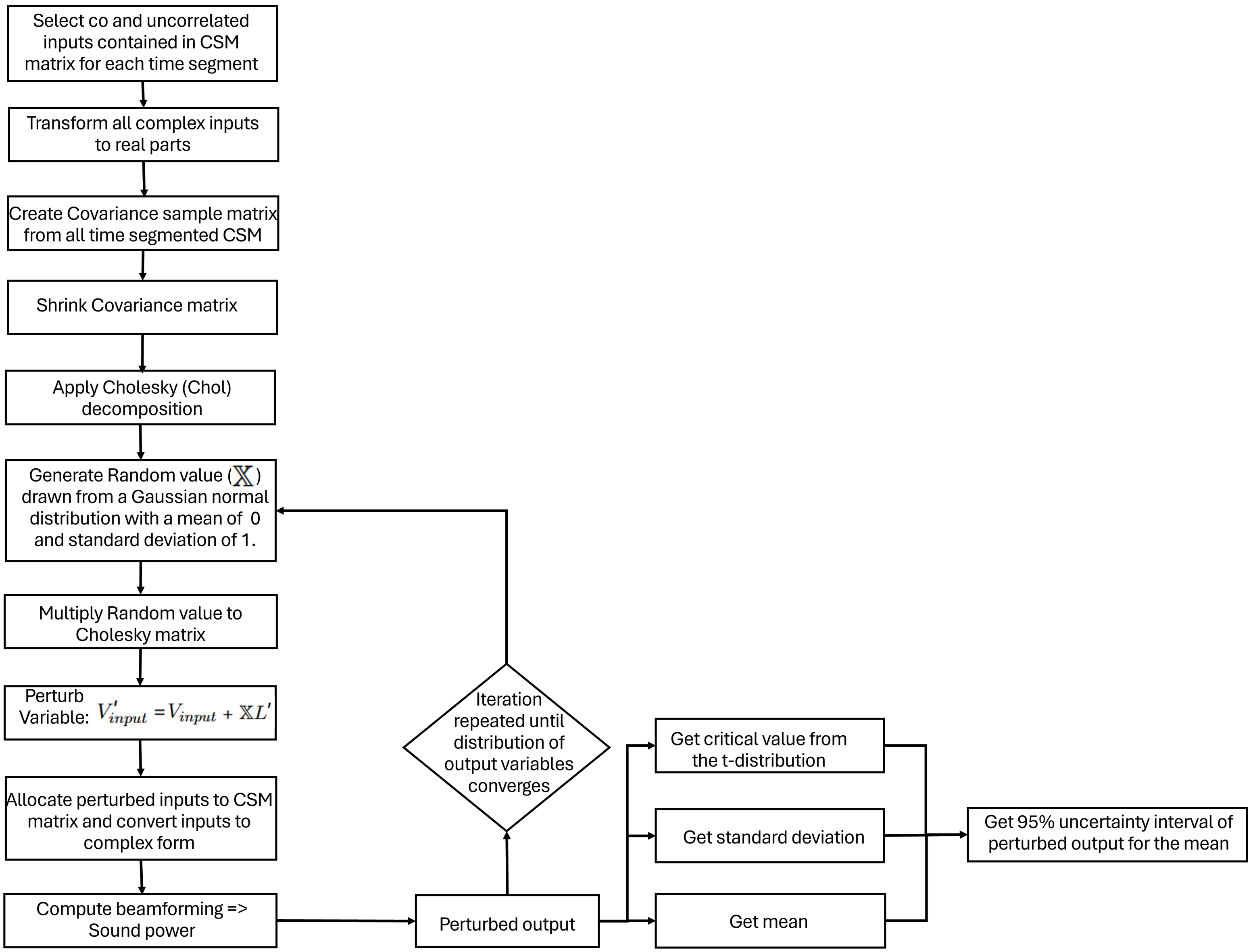

Figure 14: Monte Carlo model in Matlab for correlated variables

4 Parameter Study, Analytical Beamforming Uncertainty

4.1 Analytical model set up

The model is created based from the line source summation theory (section 2.4), it will be used as a parametric study to quantify its uncertainty in section 4.3. The microphone coordinates, grid coordinates and the airflow specifications are the same ones used from the experimental parametric study as seen in section 5. The line source is simulated along a line with vector coordinates $\boldsymbol{\xi} = (\xi, \eta, \zeta)$, with $\xi_l = 0$ and $\zeta_l = 1.801$ [m]. In addition, $-0.345 \le \eta_l \le 0.345$, forming the line source. The schematic of this model is seen in figure 15a, while figure 15b shows the conventional beamforming output with the region of interest being drawn, encircling the simulated trailing edge (line source). The flow is simulated to travel parallel to the x axis moving from the negative to the positive x direction at Mach 0.17.

In addition, for the line source model to match the same sound power magnitude at the trailing edge of the airfoil as observed in the experiment, first the experimental model is evaluated at 2 kHz (see section 5.2). Then afterwards, the amplitude of the line source model is adjusted so that it matches the same sound power magnitude as from the evaluated experimental CBF output.

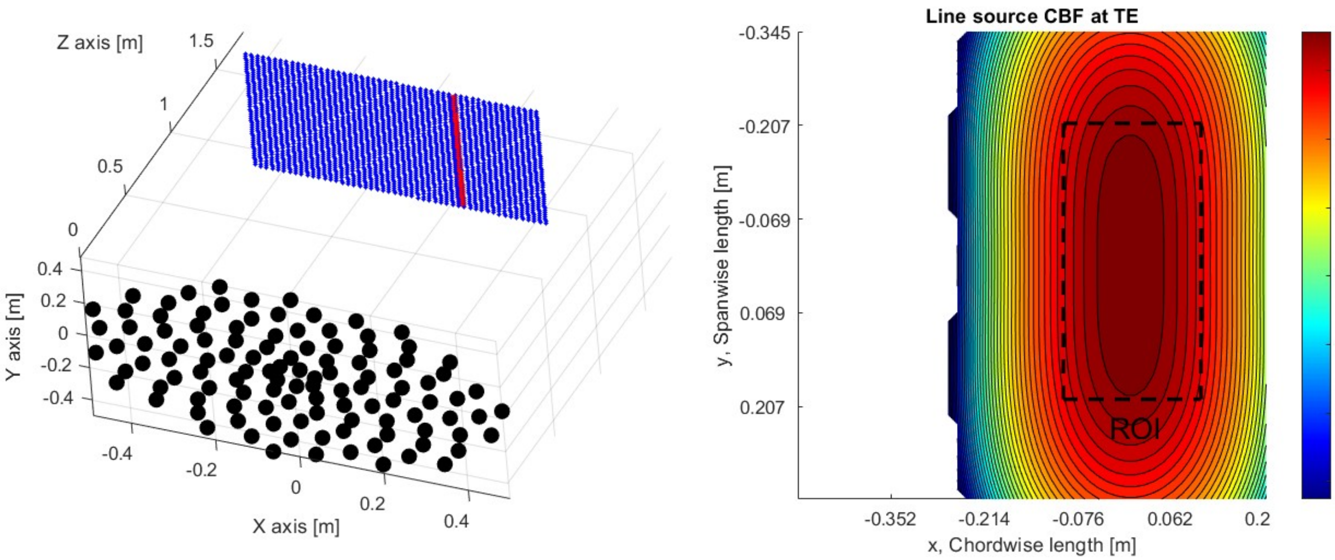

(a) (b)

Figure 15: Figure 15a shows a schematic of the analytical set up, while figure 15b shows the unperturbed Beamforming output of the analytical model for 2 kHz emitted waves.

4.2 Monte Carlo Simulation Set Up

In this section, the Monte Carlo setup will be explained prior to conducting the actual simulation. The Monte Carlo uncertainty theory described in section 3 will be applied to evaluate the analytical model introduced in section 4.1, with its associated uncertainty to be quantified in section 4.3. During the Monte Carlo simulation, 1000 iterations will be performed for each of the variables to be perturbed from the CBF algorithm for sound waves emitted at 2 kHz. The variables to be perturbed are: First, the microphone's phases will be perturbed by 1 degree standard deviation and then by 10 degree in section 4.3.1. Afterwards, the microphone's sensitivities will be perturbed by 5% and 10% of the nominal microphone sensitivity in section 4.3.2. Then, the microphone coordinates will be perturbed with standard deviations of 1 mm and 10 mm in section 4.3.3. Following this, the array broadband distance which is the distance from the center of the array to the trailing edge will be perturbed by 2.5 % and 5% of the nominal value of 1.801 meters in section 4.3.4. Afterwards, the temperature will be perturbed with standard deviations of 1 K and 3 K in section 4.3.5. Then, the Cross Spectral Matrix will be perturbed based on its segmentation, using 500 and 1000 effective segments in section 4.3.6. Finally, the model will include multiple simultaneous input perturbations (all variables mentioned above) across the entire frequency spectrum ranging from 500 Hz to 5000 Hz with 500 Hz increment as presented in section 4.3.7. Through out the entire uncertainty quantification analysis, a confidence interval of 95% is used.

Table 1 gives more details of the settings used for simulation.

Amount of sources :	20
Source Amplitude:	0.1187
Mach number:	0.1712
Room Temperature:	293.05K
Segment overlap:	50 percent
Signal length:	70000 samples
Signal time:	0.7 seconds
Sampling Frequency:	48kHz

Table 1: Line source simulation settings

4.3 Monte Carlo Results

4.3.1 Microphone phase perturbation

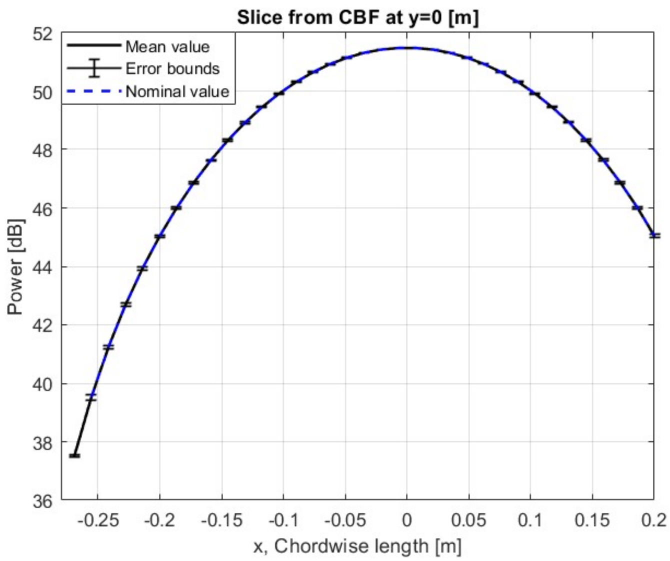

(a)

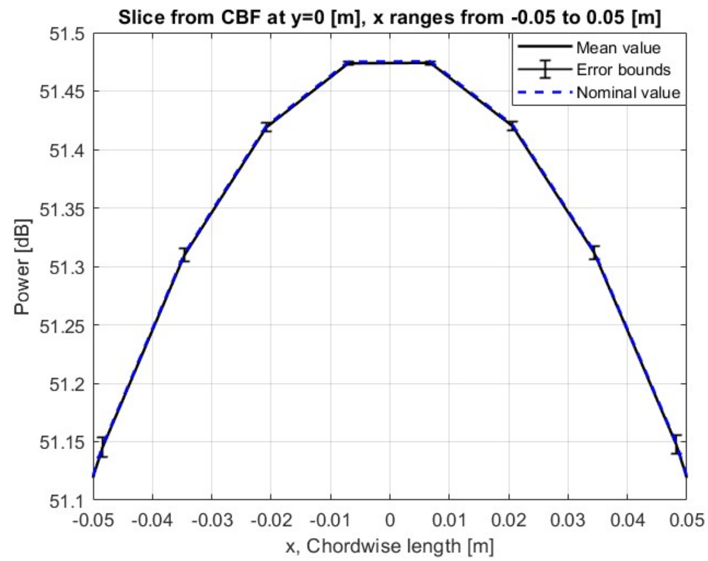

(b)

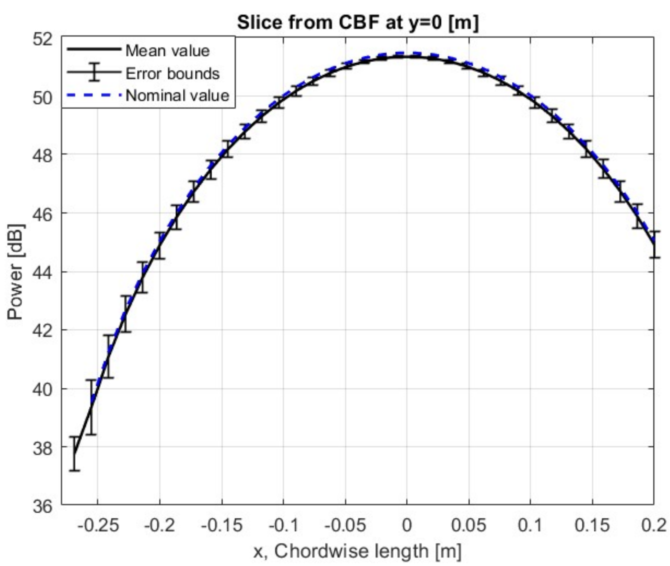

(c)

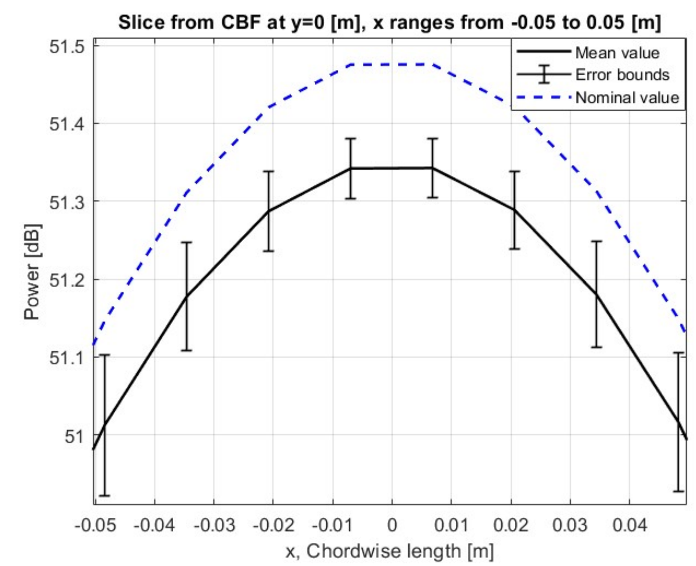

(d)

Figure 16: Quantified Uncertainty of CBF output, more specifically: Figure 16a shows microphone phase perturbations with a standard deviation of 1 degree, and figure 16b presents a closeup view of these perturbations. Similarly, figure 16c illustrates microphone phase perturbations with a standard deviation of 10 degree, while figure 16d shows a closeup view of that case.

Looking at figures 16a and 16b, it can be seen that a 1 degree perturbation in the microphone phases has very small impact to the CBF output. Especially at the source origin ($x = y = 0$), where the standard deviation is only 0.005 dB. With 95 % confidence level, the upper and lower bounds vary by only around 0.02 dB. A bit further away from the source ($x = -0.2$), the effect of the phase perturbation becomes more noticeable. The standard deviation increases to around 0.02 dB, which enlarges the uncertainty interval and results in a variation of the mean of approximately 0.1 dB.

When the phase perturbation is increased to 10 degree per microphone, as shown in figures 16c and 16d, the uncertainty of the CBF output increases. At the source location, the sound pressure level varies between the upper and lower bounds by around 0.22 dB. Farther from the source ($x = -0.2$), the variation increases to around 0.9 dB.

The statistical results from the Monte Carlo simulation of the phase perturbation are also seen in table 11a and 11b which corresponds to the 1 and 10 degree perturbations respectively. Finally, the Gaussian distributions for both cases are also plotted in the appendix, in tables 43a and 43b respectively.

4.3.2 Microphone sensitivity perturbation

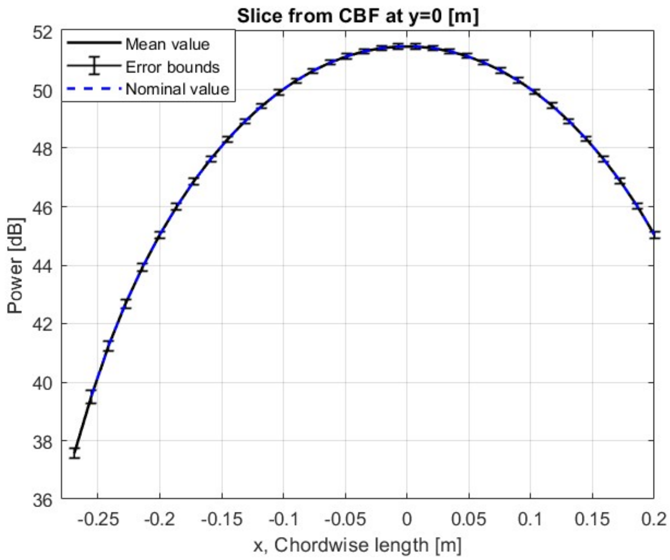

(a)

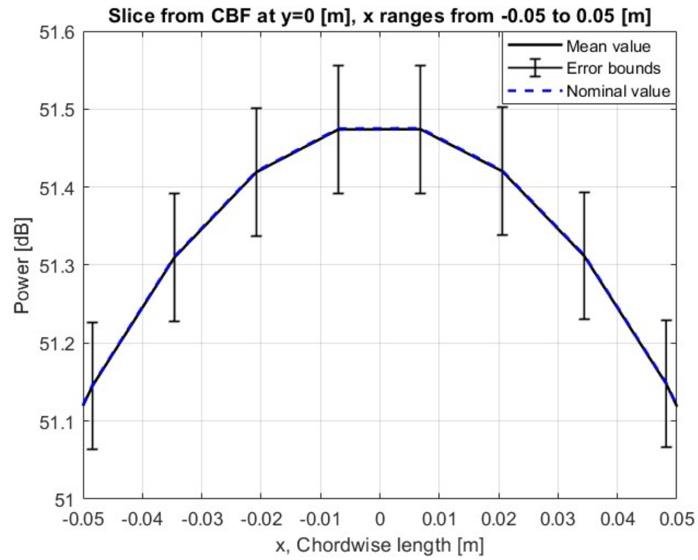

(b)

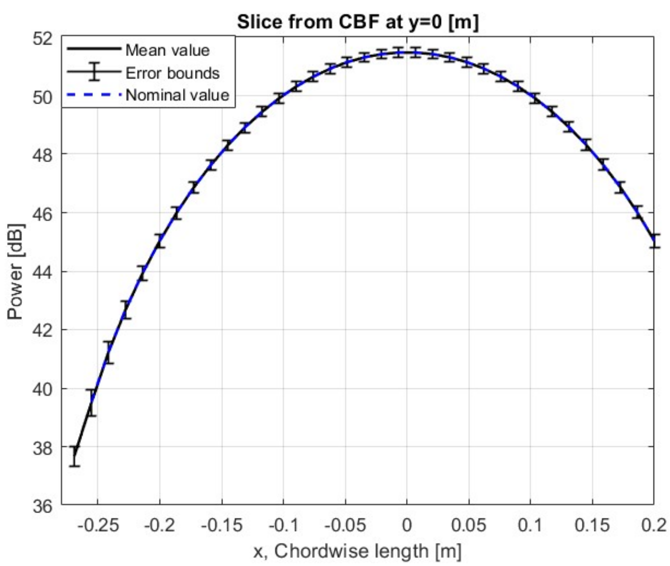

(c)

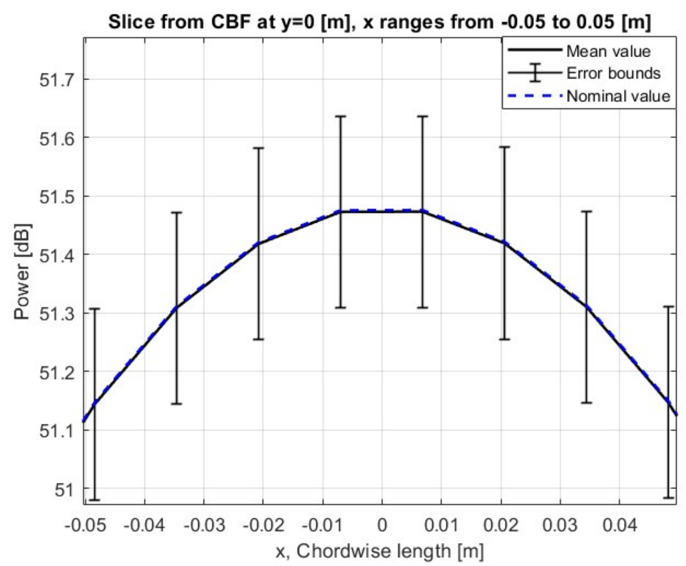

(d)

Figure 17: Quantified Uncertainty of CBF output, more specifically: Figure 17a shows microphone sensitivity perturbations of 5 %, and figure 17b presents a closeup view of these perturbations. Similarly, figure 17c illustrates microphone sensitivity perturbations of 10 %, while figure 17d shows a closeup view of that case.

For the microphone sensitivities, looking at figures 17a and 17b, it can be seen that a 5 percent perturbation in the microphone sensitivities has a larger impact to the CBF output than the phase perturbations. Especially at the source origin ($x = y = 0$), where the standard deviation is at around 0.04 dB. Using a 95 % confidence level, the upper and lower bounds vary by around 0.2 dB. Looking at a bit further away from the source ($x = -0.2$), the effect of the sensitivity perturbation becomes even more noticeable. The standard deviation increases to around 0.06 dB leading to the mean varying by about 0.2 dB.

When the sensitivity perturbation is increased to 10 percent for all microphones, as shown in figures 17c and 17d, the uncertainty of the CBF output increases. At the source location, the SPL varies between the upper and lower bounds by around 0.32 dB. Farther from the source ($x = -0.2$), the variation increases to around 0.45 dB.

The statistical results from the Monte Carlo simulation of the sensitivity perturbation are also seen in table 12a and 12b which corresponds to the 5 and 10 percent perturbations respectively. Finally, the Gaussian distributions for both cases are also plotted in the appendix, in tables 44a and 44b respectively.

4.3.3 Microphone location perturbation

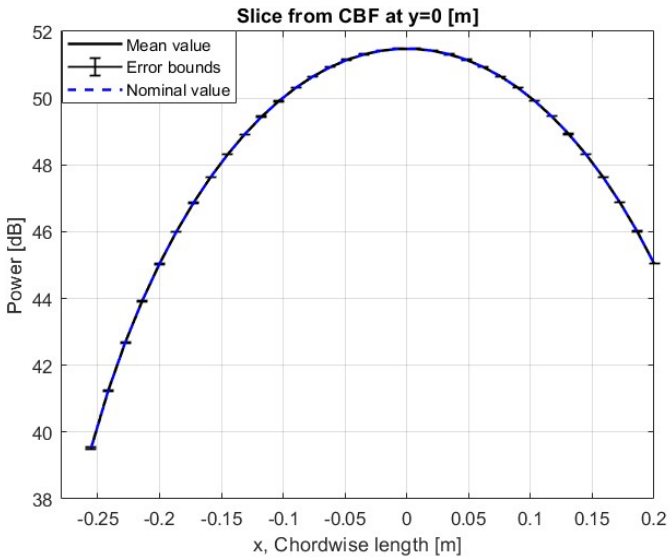

(a)

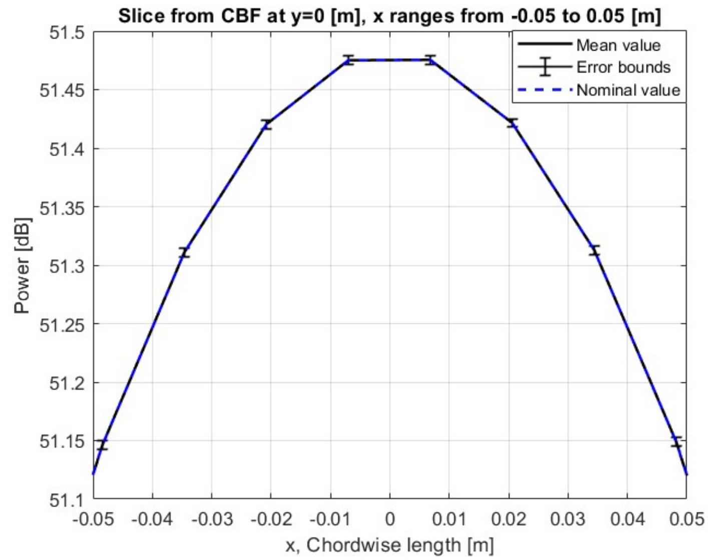

(b)

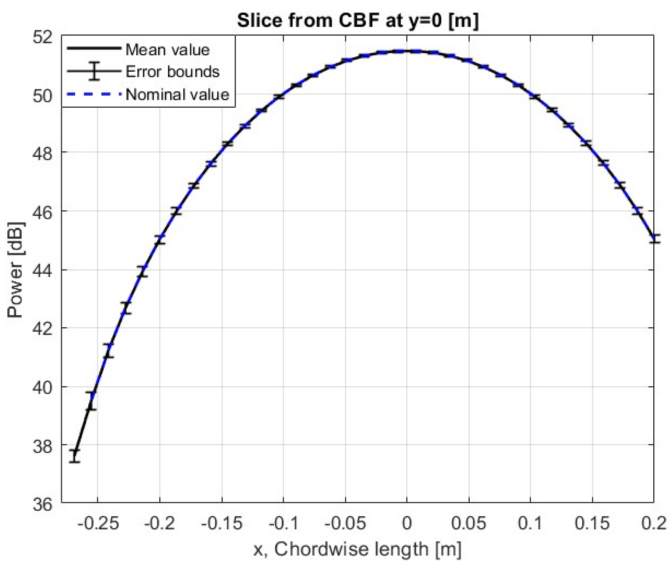

(c)

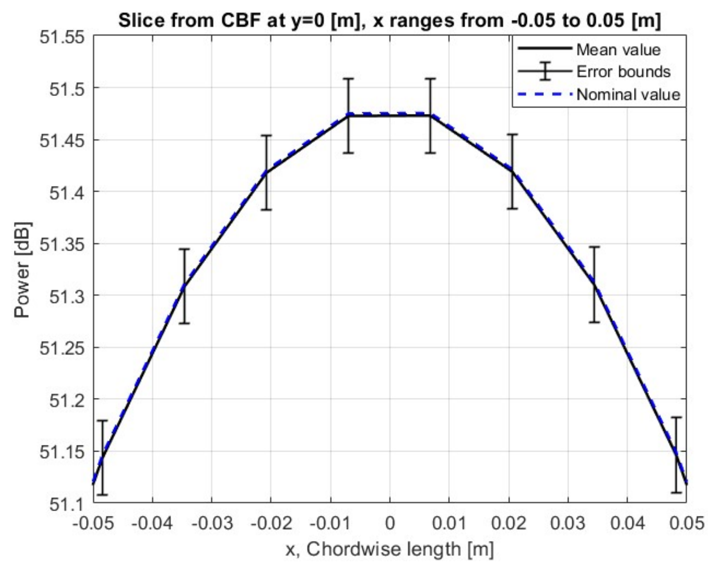

(d)

Figure 18: Quantified Uncertainty of CBF output, more specifically: Figure 18a shows microphone location perturbations of 1mm, and figure 18b presents a closeup view of these perturbations. Similarly, figure 18c illustrates microphone location perturbations of 10 mm, while figure 18d shows a closeup view of that case.

For the microphone coordinates being perturbed, looking at figures 18a and 18b, it can be seen that a 1 mm perturbation in the microphone coordinates doesn't affect much the CBF output. At the source origin ($x = y = 0$), the standard deviation is only around 0.002 dB. Looking at a bit further away from the source ($x = -0.2$), the effect of the microphone location perturbation becomes slightly more noticeable but still doesn't affect much the CBF output. More specifically, the standard deviation slightly increases to around 0.006 dB

When the coordinates perturbation is increased to 10 mm for all microphones, as shown in figures 18c and 18d, the uncertainty of the CBF output increases. At the source location, the sound pressure level varies between the upper and lower bounds by around 0.08 dB. Farther from the source ($x = -0.2$), the variation increases to around 0.25 dB.

The statistical results from the Monte Carlo simulation of the microphone coordinate perturbations are also seen in table 13a and 13b which corresponds to the 1 and 10 mm perturbations respectively. Finally, the Gaussian distributions for both cases are also plotted in the appendix, in tables 45a and 45b respectively.

4.3.4 Array broadband distance perturbation

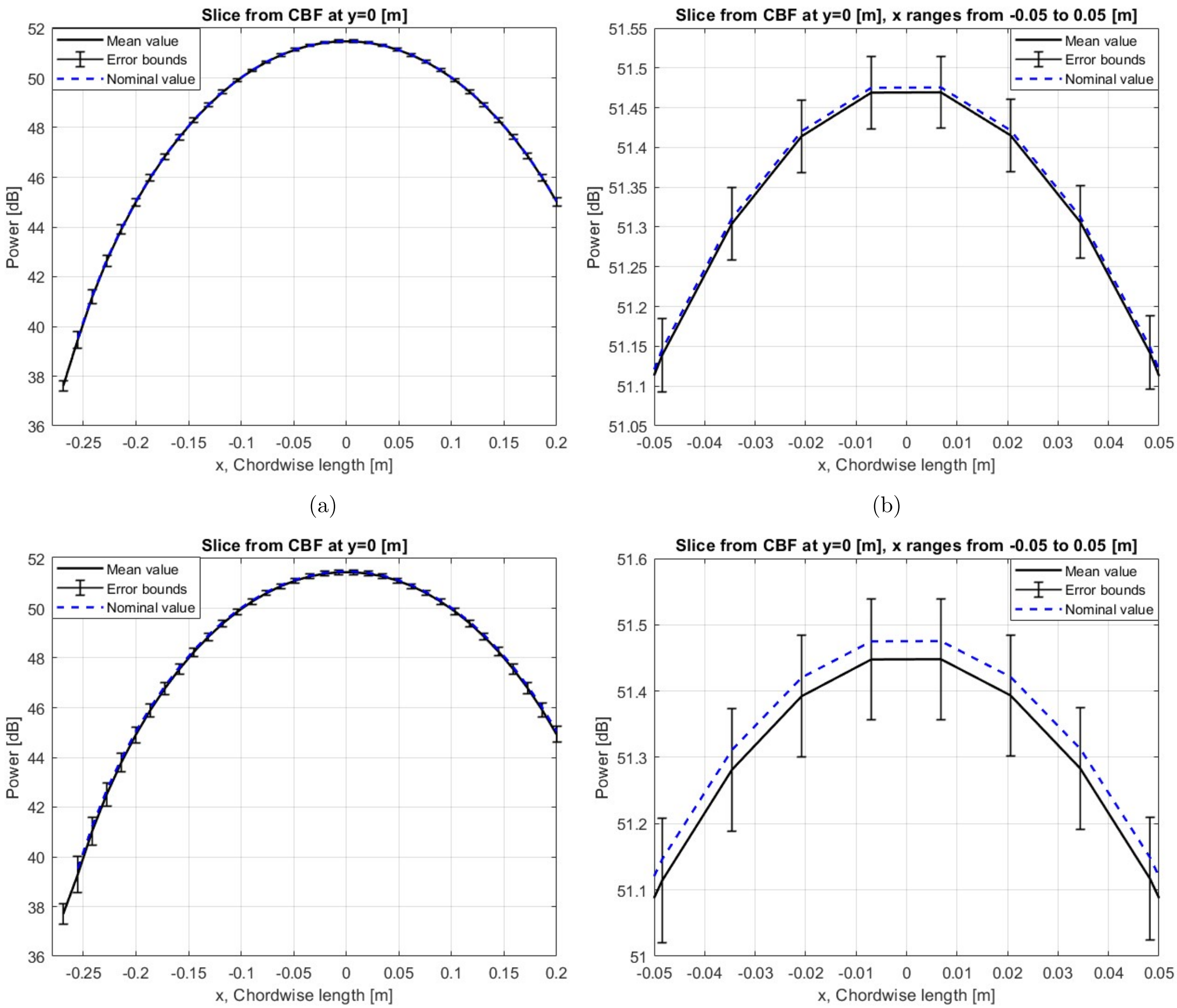

(a) (b) (c) (d)

Figure 19: Quantified Uncertainty of CBF output, more specifically: Figure 19a shows the array broadband distance perturbed with a standard deviation of 45mm (2.5%), and figure 19b presents a closeup view of these perturbations. Similarly, figure 19c illustrates the array broadband distance perturbed with a standard deviation of 90 mm (5%), while figure 19d shows a closeup view of that case.

In this section, the Array broadband distance is perturbed, looking at figures 19a and 19b, it can be seen that a 2.5 percent perturbation in the array distance does affect the CBF output. At the source origin ($x = y = 0$), the standard deviation is around 0.02 dB. That makes the sound pressure level to vary by 0.08 dB. Looking at a bit further away from the source ($x = -0.2$), the effect of the array perturbation becomes slightly more noticeable. More specifically, the standard deviation slightly increases to around 0.08 dB, increasing the sound pressure level variation to around 0.2 dB.

However, when the array distance perturbation is increased to 5 percent, as shown in figures 19c and 19d, the uncertainty of the CBF output increases to a considerable level. At the source location, the sound pressure level varies between the upper and lower bounds by around 0.2 dB. Farther from the source ($x = -0.2$), the variation increases to around 0.7 dB for always a 95 percent confidence, with a standard deviation of 0.16 dB.

The statistical results from the Monte Carlo simulation of the array broadband distance perturbations are also seen in table 14a and 14b which corresponds to the 45 and 90 mm perturbations respectively. Finally, the Gaussian distributions for both cases are also plotted in the appendix, in tables 46a and 46b respectively.

4.3.5 Temperature perturbation

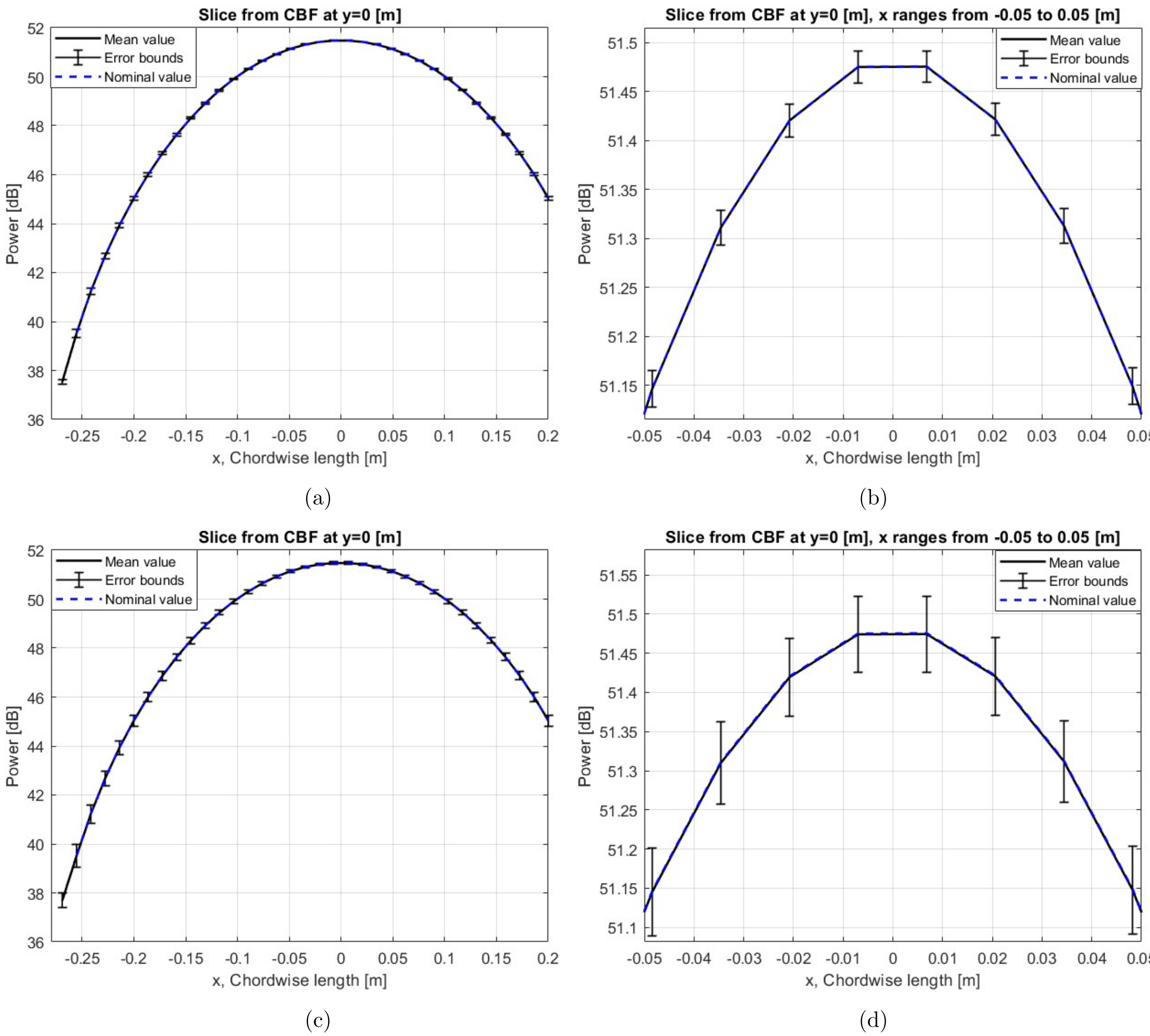

Figure 20: Quantified Uncertainty of CBF output, more specifically: Figure 20a shows the Temperature perturbed with a standard deviation of 1 kelvin, and figure 20b presents a closeup view of these perturbation. Similarly, figure 20c illustrates the Temperature perturbed with a standard deviation of 3 kelvin, while figure 20d shows a closeup view of that case.

The temperature is a very important parameter for the beamforming as the speed of sound is dependent on it which directly impacts the beamforming amplitude and localization. Here, the temperature is perturbed. From figures 20a and 20b, it can be seen that a 1 kelvin perturbation in the Temperature is applied. As seen, it doesn't greatly impact the CBF output. More specifically, at the source origin ($x = y = 0$), the standard deviation is around 0.01 dB. That makes the sound pressure level to vary by 0.04 dB. Looking at a bit further away from the source ($x = -0.2$), the effect of the temperature perturbation increases. More specifically, the standard deviation only slightly increases to around 0.04 dB.

For the second case, the temperature perturbation is increased to 3 kelvin, as shown in figures 20c and 20d. At the source location, the sound pressure level varies between the upper and lower bounds by around 0.12 dB. Farther from the source ($x = -0.2$), the variation of the sound pressure level increases to around 0.45 dB, with a standard deviation of 0.03 dB.

The statistical results from the Monte Carlo simulation of the temperature perturbations are also seen in table 15a and 15b which corresponds to the 1 and 3 kelvin perturbations respectively. Finally, the gaussian distributions for both cases are also plotted in the appendix, in tables 47a and 47b respectively.

4.3.6 Cross spectral matrix perturbation

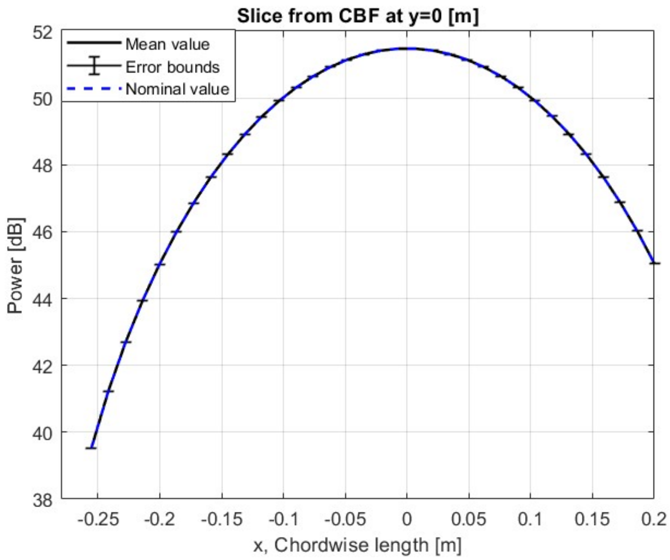

(a)

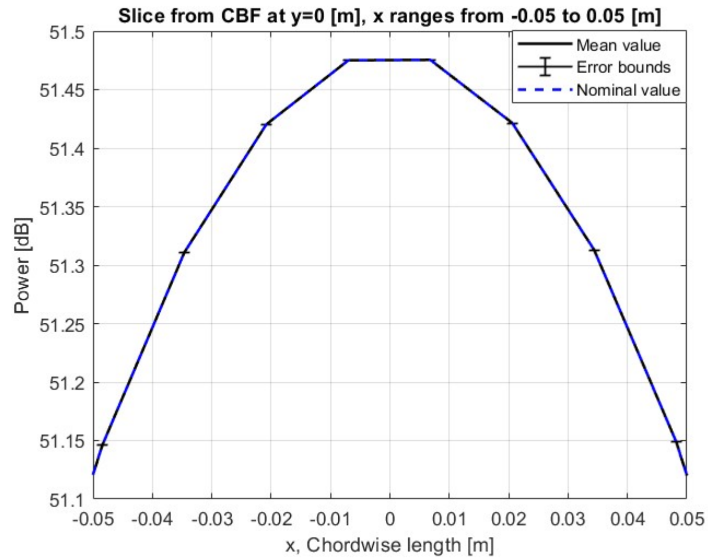

(b)

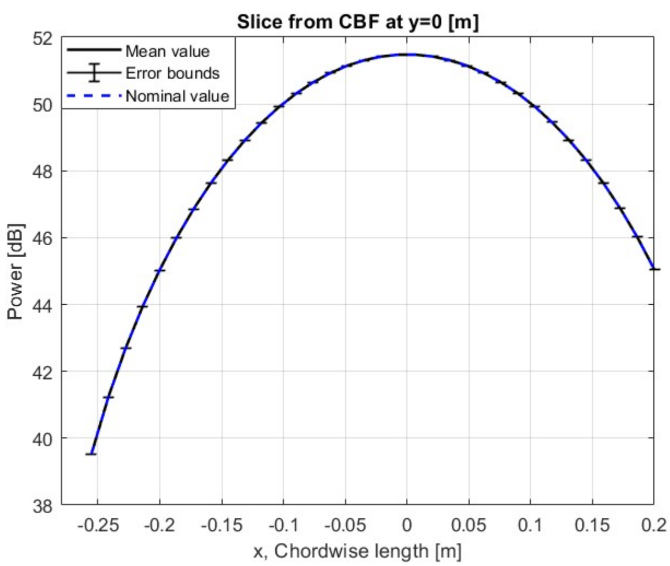

(c)

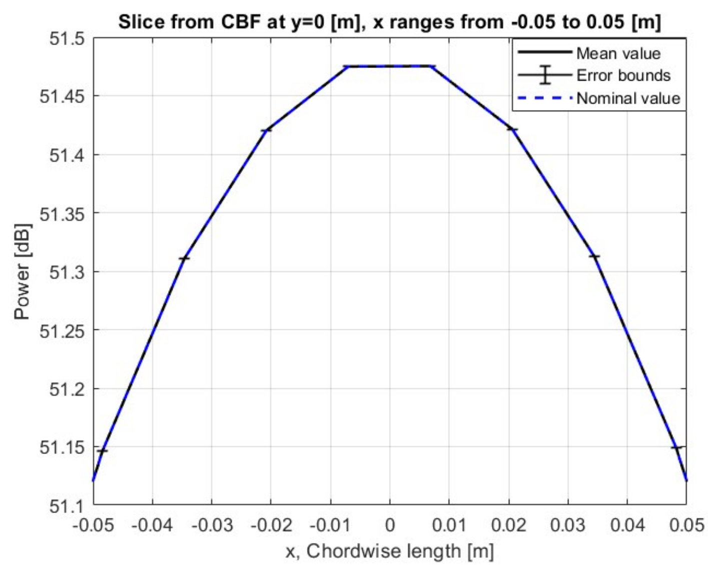

(d)

Figure 21: Quantified Uncertainty of CBF output, more specifically: Figure 21a shows the CSM perturbed with 500 effective segments, and figure 21b presents a closeup view of these perturbations. Similarly, figure 21c illustrates the CSM perturbed with 1000 effective segments, while figure 21d shows a closeup view of that case.

For the Cross Spectral Matrix perturbation, the uncertainty results are as expected. The uncertainty is very small and almost negligible. This happens because the analytical model uses an ideal, cosine varying sound source. The microphones capture a signal that varies periodically. When segments of that signal are transformed into frequency domain, the resulting CSM across each of the effective segments (time segments) are nearly identical. They are nearly identical and not fully due to some rounding errors in the analytical model made by Matlab. therefore, the CSM still has a very small amount of uncertainty, with the standard deviation at the source measured to be only $4.00e-5$ dB. Figures 21a and 21b show the CSM uncertainty results for 500 segments and figures 21c and 21d show the CSM uncertainty for 1000 segments. Consequently, by varying the effective segments, wont affect the CSM as also seen from the statistical summary (tables 16a and 16b). For the experimental model, where each microphone captures a sound source with lots of background noise, the resulting uncertainty will differ and have a major impact on the CBF output, as discussed later in section 5.3.6.

4.3.7 Multi variable perturbation

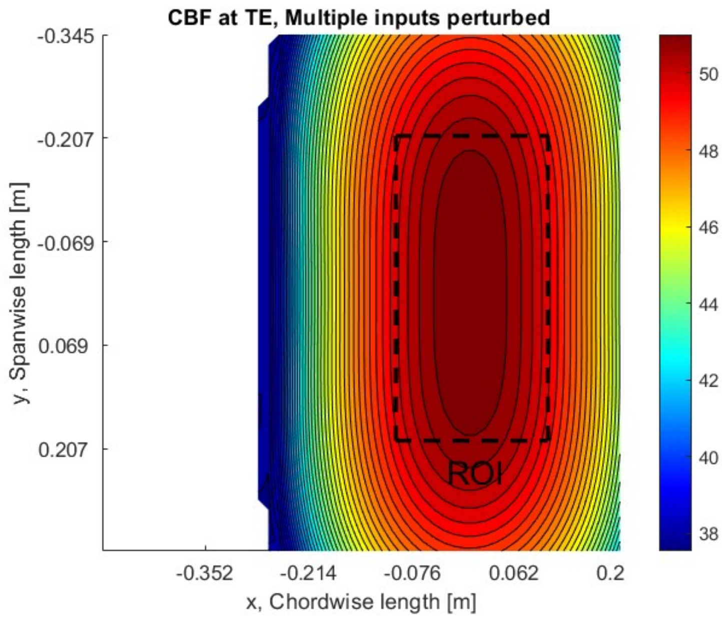

Figure 22: CBF output of the Monte Carlo simulation with multiple perturbed inputs for sound waves emitted at 2 kHz frequency.

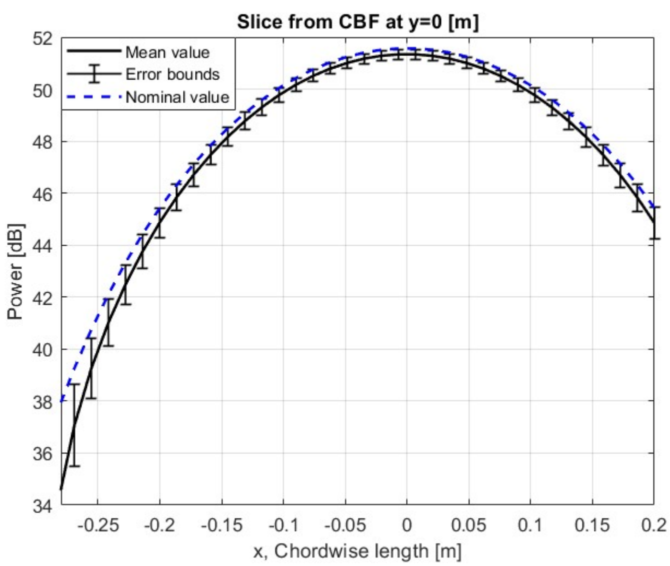

(a)

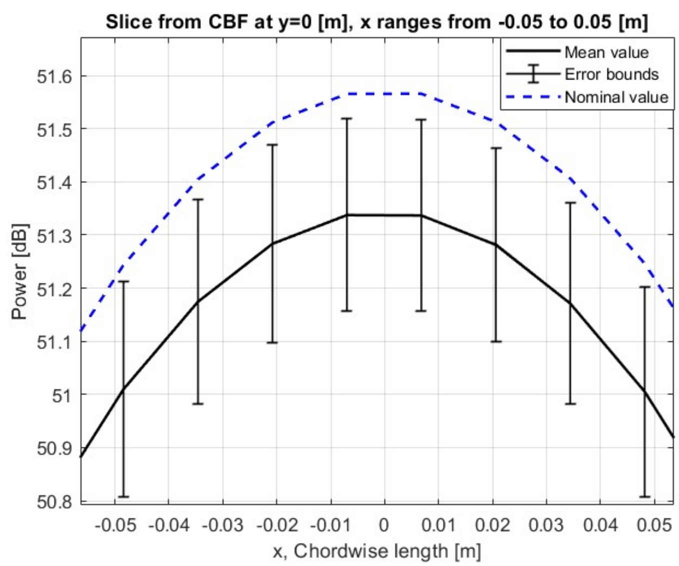

(b)

Figure 23: Figure 23a illustrates the error bounds of the CBF output for 2 kHz waves, while figure 23b illustrates a closeup view of the same case.

In this section, all individually perturbed variables are now simultaneously perturbed throughout the frequency spectrum using 500 Monte Carlo iterations. Specifically, the microphone phase is perturbed with 10 degree, microphone sensitivity with 10 percent, microphone position with 10 mm, array broadband distance with 2.5 percent, and the temperature with 3 kelvin standard deviations. In addition, the CSM is perturbed. All perturbations are done with using 500 effective segments. For 2 kHz, the CBF output is visualized in figure 22. At this frequency, the uncertainty error bounds around the mean of the 500 Monte Carlo iterations are showed in figures 23a and 23b. Specifically, at the source location ($x = y = 0$ [m]), the standard deviation is approximately 0.10 dB, and the sound pressure level varies by ±0.19 dB. As we increase the frequency to 5 kHz, the SPL varies approximately by ±0.24 dB. A statistical summary of the analytical multivariate Monte Carlo simulation is given in table 9.

In addition, the power spectral density is performed by integrating the sound power over a region of interest as explained in section 2.6 and then converting it to logarithmic dB scale with using equation 10. The PSD is presented in figure 24. Starting from a sound pressure level variation of approximately 0.23 dB at 2 kHz, the variation increases with frequency, as expected. The sound pressure level of the integrated sound power uncertainty reaches approximately 1.38 dB at 5 kHz.

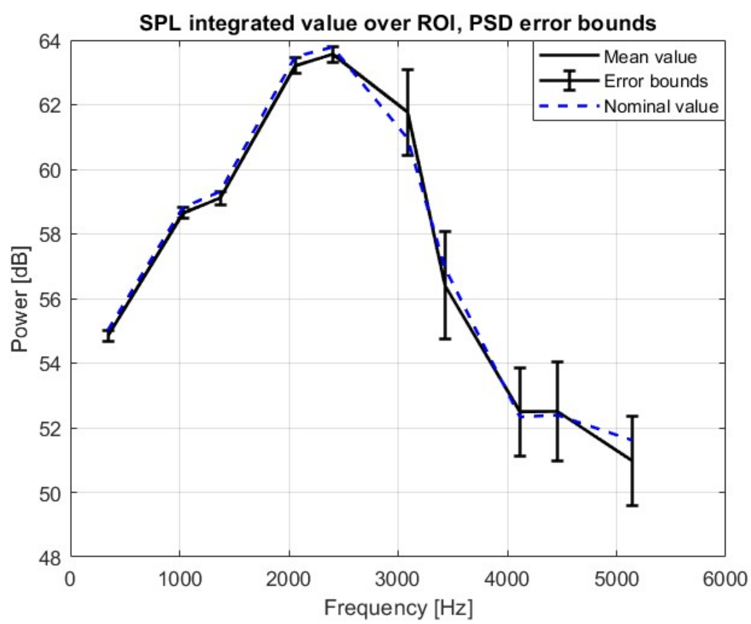

Figure 24: SPL of the integrated sound power across the frequency spectrum defined from section 4.2, along with its error bounds, computed from the Monte Carlo multivariate perturbation simulation.

A statistical summary of the SPL of the integrated sound power of the analytical multivariate Monte Carlo simulation is provided in table 10 for all frequencies tested during the experiment (500 to 5000 Hz).

5 Parameter Study, Experimental Beamforming Uncertainty

Section 5 will analyze the uncertainty of the acoustic Beamforming during an experiment. The noise mechanism to be examined will be the sound produced by the interaction of fluid particles to the airfoil, more specifically the sound emitted from the turbulent eddies while leaving the trailing edge to enter the free field [14].

5.1 Experimental set up

The experiment will be performed at the wind tunnel of Twente University. A microphone phased array will be assembled and used (discussed in more detail in section 5.1.2) with the goal to capture pressure variations of the airfoil's trailing edge, situated in the far field. After the experiment is performed, the data will be processed and artificial perturbation inputs (discussed in section 3.1) will be incorporated to the beamforming algorithm.nThe test set up to be conducted is first visualized with a top view drawing as seen in figure 25a. The experiment is then set up in the wind tunnel, as shown in figure 25b.

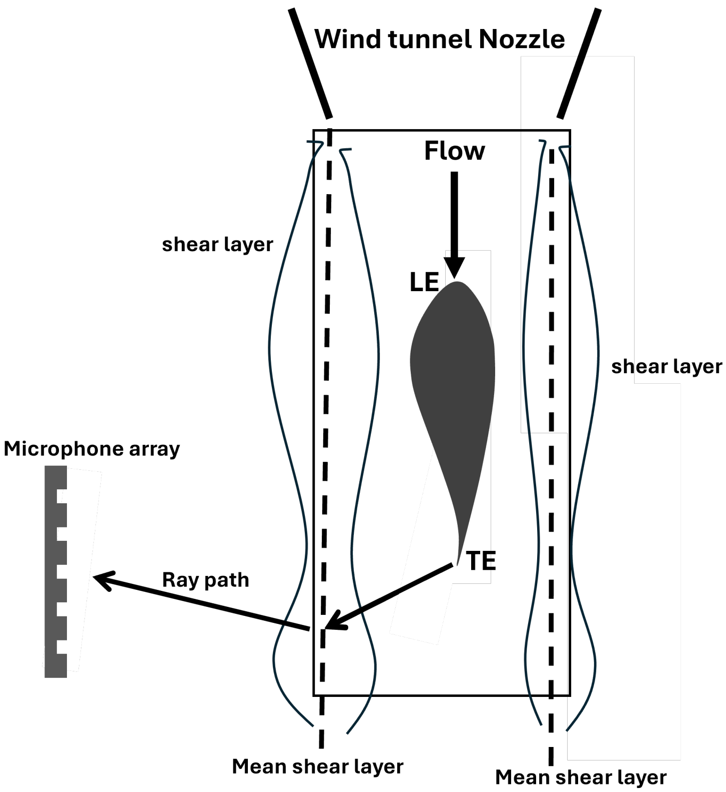

(a)

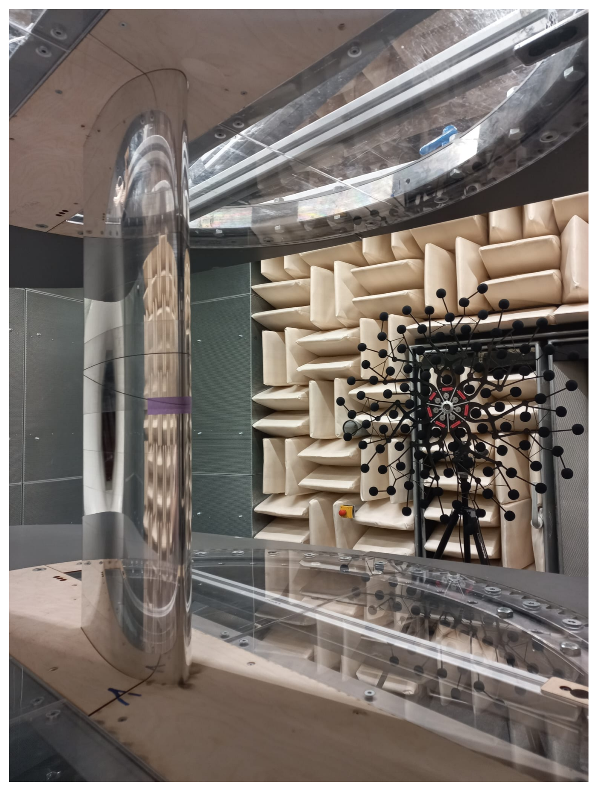

(b)

Figure 25: Figure 25a shows a schematic of the experimental set up while figure 25b shows the actual experimental setup including the airfoil and the microphone array. The airfoil can be seen without any tripping device installed yet.

5.1.1 Microphone Array and Search grid set up

The microphone array is required to be as close as possible to the airfoil to achieve the highest spatial resolution possible, while still remaining in the far field, as explained in section 5.1.2. In this experiment, the array was positioned 1.8 meters from the trailing edge because the wind effects were already noticeable to the array at that distance. Moving the array any closer would have made the microphones to vibrate due to the airflow, potentially resulting in small but important displacements of a few millimeters. That could lead to measurement inaccuracies, and therefore it was decided to keep the array at that distance.

The airfoil spans 0.345 meters in both directions from its center as seen from section 5.1.4. Therefore, a search grid was created at the trailing edge location, extending 0.345 meters in y spanwise direction from the center. The grid and array positions are shown in Table 2.

Table 2: **Search grid and Microphone array positions**

Trailing edge position (x):	z = 1.801 meters
Microphone array center position (x,y,z):	(0,0,0) meters
Plane search grid position (y):	−0.345 to 0.345 meters
Plane search grid position (x):	−0.49 to 0.2 meters
Sampling rate of array:	48000 Hz
Individual microphone positions (x,y,z):	See appendix E

The microphone array is assembled inside the anechoic chamber and mounted on a tripod. To ensure stability, the tripod is weighted to prevent it from tipping over. A laser distance meter is used to precisely position the microphone array at 1.801 meters perpendicular to the airfoil's trailing edge.

5.1.2 Array Point Spread Function

The array point spread function (PSF) returns the microphone response. The PSF measures how much the pressure signal coming from the source is spread into the neighboring locations at each grid point. A wide PSF means that the beamformer has poor spatial resolution due to the fact that the energy is more spread around the neighboring grid points. The goal is to get a sharp PSF peak which is visible at the source location. This section gives the PSF of the experimental microphone array setup, that is to provide reference for the beamforming resolution that can be used in future research aiming to replicate this experiment.

To perform the PSF, the source is simulated at the center of the span, at the trailing edge location, by placing a speaker and recording the sound via the microphones array. After getting the PSF of the microphone array, a main slope around the source will be visible. That is the array's response to the source. By normalizing the beamforming output so that the maximum value is 0 dB, the -3 dB location can be found as seen in figure 26a. These points define the beam width, which is the spatial resolution in meters.

Figure 26a shows the PSF of the array at 2kHz. More specifically, a 3-dB beam width of that array can be seen plotted against its relative frequency at an array broadband distance d_{array} of $z = 1.801$ meters. In addition, the PSF is plotted in Figure 26b for all test frequencies ranging from 0.5 to 10 kHz, with an array broadband distance of 1.801 meters.

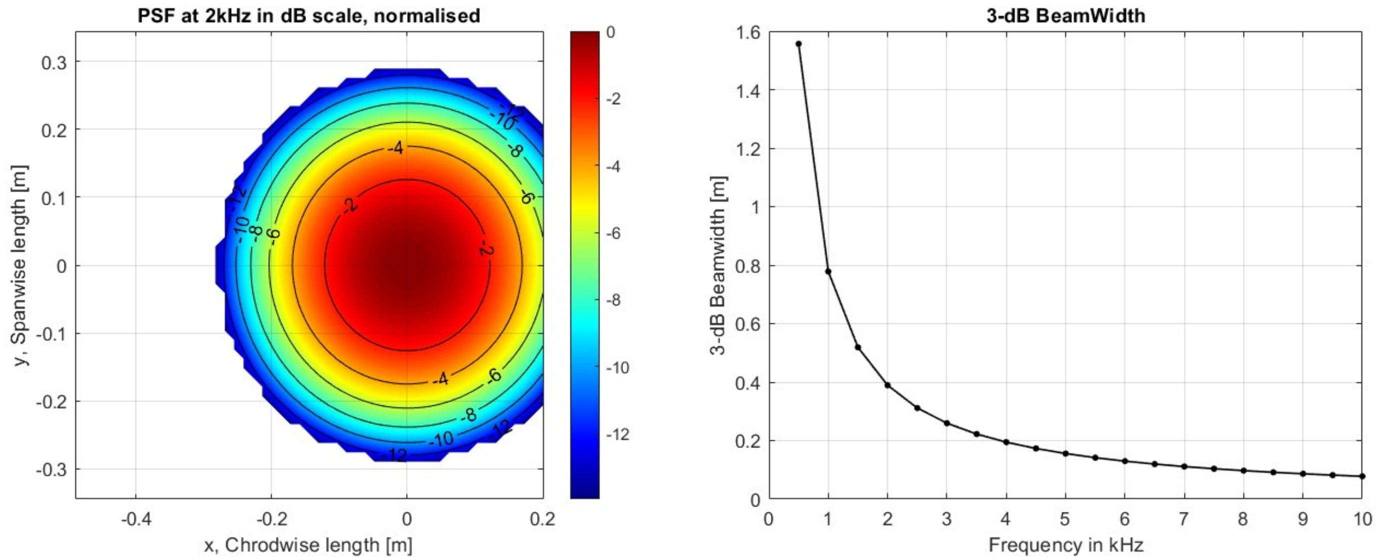

(a) (b)

Figure 26: Figure 26a shows the point spread function at 2kHz. Figure 26b shows the PSF at a frequency range from 500 to 10000 hz. Both figure's PSF are taken from a array broadband distance of 1.801 meters.

The beam width which is also called the spatial resolution can also be computed analytically by using the Rayleigh criterion [16]:

$$beam\ width = 1.22\frac{\lambda D_{array}}{d_{array}} \tag{57}$$

The near field is defined as within one wavelength of the source [13]. In acoustic beamforming, the goal is to estimate the sound field in the far field. In addition, for better beamforming performance, it is necessary to maximize the spatial resolution as much as possible. According to equation 57, the only way to physically improve the spatial resolution without changing the diameter of the array D_{array} is to reduce the array broadband distance d_{array}. However, the minimum possible distance was limited to around 1.8 meters due to concerns that the wind tunnel flow could cause the array to tip over if it was placed any closer.

5.1.3 Wind Tunnel and Flow Conditions

To generate an airflow around the airfoil inside the wind tunnel, multiple sensors were used. The axial flow velocity U_x was measured using a Pitot tube, which defines the velocity by computing the pressure difference. Additionally, three thermometers were placed next to each other just outside the test section (next to the nozzle wall where the flow exits) to measure the temperature at three different vertical positions. An average of all of them was taken to define the temperature T_0.

First, a preliminary flow calibration was performed by running the wind tunnel at different power percentages and recording their corresponding flow velocities. Once a target velocity of approximately 58.8 $[m/s]$ (to reach around 0.17 Mach) was achieved, the corresponding power level was recorded. The pitot tube was then removed to avoid flow disruption around the airfoil which could impact the aeroacoustic results. The actual experimental aeroacoustic test was then performed using the recorded power level found during the calibration. Each test run lasts 25 seconds and records around 1200000 data points per run, with a 48 kHz sampling frequency. Finally, the data captured by the microphones is saved in Lab view CAE software. The flow conditions during the experiment are showed in table 3 where the Reynolds numbers are calculated using equation 58, the speed of sound is determined with equation 59 and the Mach number is found by dividing U_x by the speed of sound c_0.

$$Re_c = \frac{\rho U_\infty c}{\mu} \tag{58}$$

$$c_0 = \sqrt{\frac{\gamma_{gas} R_{gas} T_0}{Moll_{mass}}} \tag{59}$$

Table 3: Flow conditions

Speed of sound (c_0) :	343.3173 $[m/s]$
Density (ρ):	1.2148 $[kg/m^3]$
Dynamic viscosity: μ	$18.1e-6$ $[kg/(ms)]$
Re_c:	$1.1982e+6$
Mach number:	0.1712
U_x:	58.7847 $[m/s]$
Specific gas constant of air (R_{gas}):	8.3140 $[J/(molK)]$
Room Temperature (T_0):	293.05 [K]
$Moll_{mass}$:	0.02897 $[kg/mol]$
Ratio of specific heat of air (γ_{gas}):	1.401

The flow velocity and angle of attack of the airfoil (the later discussed in section 5.1.4) are selected based on the NASA and DLR benchmark studies, which most often use a Mach number of 0.17 and an angle of attack of -1.2 degree. These values are chosen because at Mach 0.17, the flow is in the low subsonic regime, which has still low compressibility effects and generates significant trailing edge sound. In addition, the small negative angle of attack minimizes the lift generated by the cambered airfoil. The negative angle of attack prevents flow separation and stall from happening, which could otherwise introduce other unwanted sound mechanisms such as vortex shedding [22].

5.1.4 Airfoil and Tripping Device

Since the objective is to create sound from the trailing edge, a tripping device with a specific thickness will be applied near the leading edge of the airfoil. This leads to the boundary layer to transition to turbulence earlier, resulting in a more turbulent flow over the trailing edge. The increased turbulence increases the sound generated at the trailing edge, making it more easily to be detected by the microphone array during the beamforming process. A zigzag tape is used as the tripping device to force the transition in the boundary layer. In this section, the thickness and placement location of the tripping device around the airfoil will be examined. The airfoil profile used is the DU97-W-300 as can be also seen from figure 40a. The roughness Reynolds number R_{ek} (see equation 60) defines the roughness thickness k required to transition the flow from laminar to turbulent. Vortices begin to appear at $R_{ek} = 300$ and as R_{ek} increases, the flow bypasses linear transition and instead, turbulent flow develops rapidly downstream of the roughness tripping device [3]. To define the roughness Reynolds number R_{ek}, a computational analysis using XFOIL is performed with forced transition. Next, the velocity distribution along the boundary layer throughout the surface of the airfoil is defined and used to solve the roughness Reynolds R_{ek} equation. The airfoil's characteristics from table 4 are used as inputs in XFOIL to compute the turbulent boundary layer.

Table 4: Xfoil inputs

Angle of attack to be tested:	-1.2 [°]
Chord length(b):	0.25 [m]
Span length (d):	0.695 [m]

Xfoil indicates that for the upper and lower section of the airfoil, the boundary layer thickness is starting to rapidly increase from 10 percent chordlength and onward. Placing a tripping device near the leading edge, below 10 percent of chordlength, would be effective as the boundary layer is smaller in height at that location and thus the tripping device would have a larger impact on that boundary layer. For this reason, the boundary layer velocity profile is computed for 8% of the chord length along the airfoil. The turbulent boundary layer is computed and shown in the appendix, section D by using method of Pohlhausen [6] along with Xfoil. The results indicate that with a roughness thickness k of 0.3 mm (which was readily available in large quantities), the computed velocity at 0.3 mm perpendicular to the surface of the airfoil was found to be 33 m/s, therefore the roughness Reynolds number is calculated as follows:

$$R_{ek} = \frac{\rho u(y) k}{\mu} = \frac{1.214 * 33 * 0.0003}{18.1e-6} = 664.01 \tag{60}$$

$R_{ek} = 664.01$, which is higher than 300, and will ensure flow transition starting at 8 % chordlength. As a result, table 5 presents the tripping device characteristics to be used on the airfoil.

Table 5: Test conditions

Tripping device thickness:	0.3mm
Tripping device position:	8 percent chordlength

In addition, Figure 27a shows a cross sectional drawing of the airfoil with the tripping device installed at 8% chord on both the upper and lower surfaces. Figure 27b displays the actual airfoil with the zigzag tripping tape of 0.3 mm thickness applied. And finally, Figure 27c presents the airfoil with the tripping device installed inside the wind tunnel room.

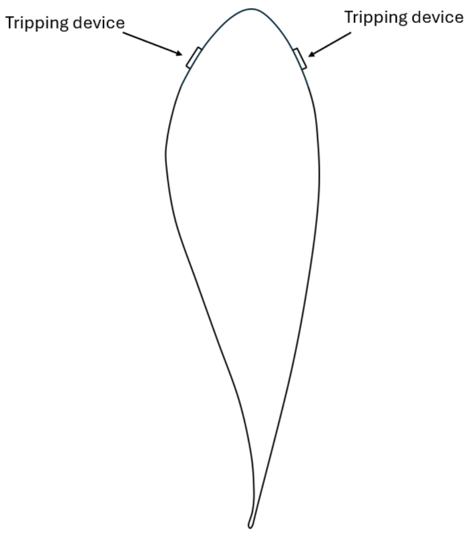

(a)

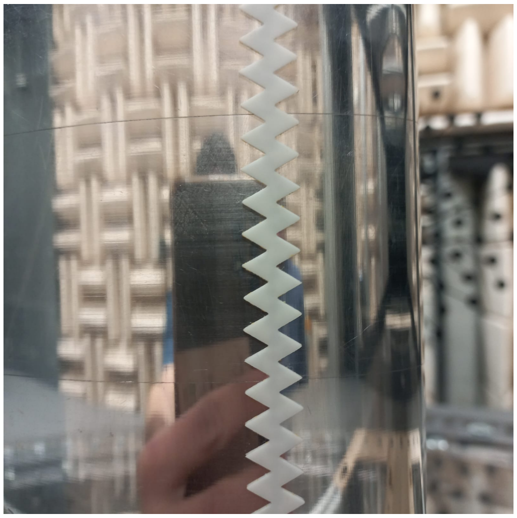

(b)

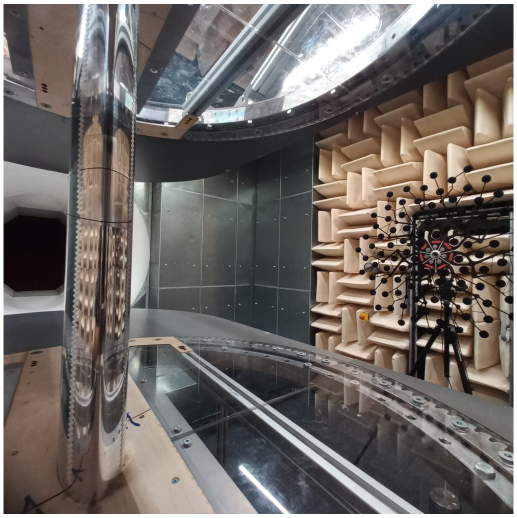

(c)

Figure 27: Figure 27a shows a schematic of the airfoil with the tripping device. Figure 27b shows the actual airfoil with the tripping device installed. Figure 27c shows the complete experimental setup prepared for the aeroacoustic testing.

5.1.5 Signal to noise ratio

The signal to noise ratio SNR is defined [26] by first converting the SPL of the integrated sound powers P_{int} to linear scale before dividing the SPL of the integrated sound power of the airfoil SPL_{int} with the background SPL integrated sound power SPL_{int}^{noise}:

$$SNR(f) = 10log10\left(\frac{10^{\frac{SPL_{int}(f)}{10}}}{10^{\frac{SPL_{int}^{\text{noise}}(f)}{10}}}\right) \quad , units\ in\ [dB] \tag{61}$$

The wind tunnel was initially powered on under the same flow conditions used for testing the airfoil, but without the airfoil installed. This allowed to measure the background noise generated within the wind tunnel chamber. Afterwards, the airfoil was installed, and the total Sound Pressure Level which includes both the background noise and the noise produced by the airfoil was measured. For both cases, the diagonal of the cross spectral matrix was removed in order to further reduce the background noise. Figure 28 shows the SPL of the integrated sound power in dB units, measured with and without the airfoil installed.

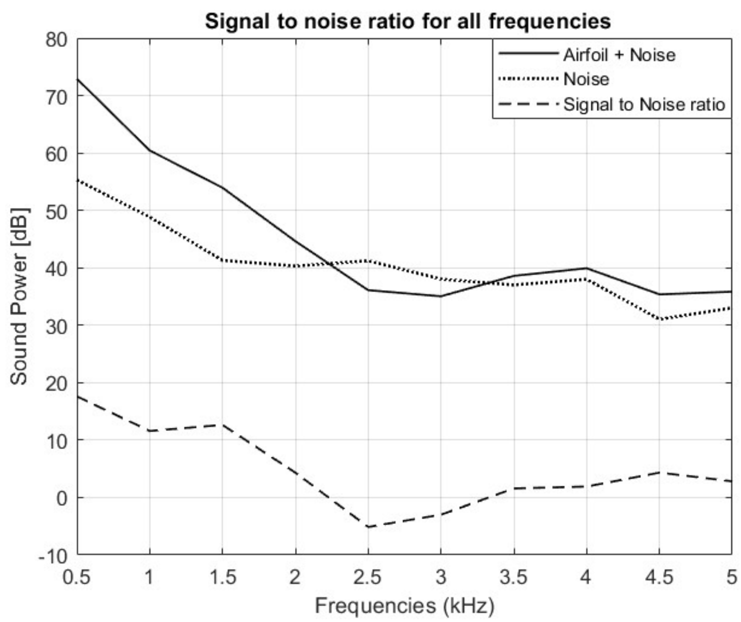

Figure 28: SPL of the integrated sound power of the airfoil, including the background noise, compared to the SPL of the integrated sound power of the background noise alone across all frequencies.

Unfortunately, as can also be seen from figure 28, higher than 2500 Hz leads to lots of background noise and the airfoil can not be localized anymore. For this reason the experiment will be evaluated till 2500 Hz. The analytical model which doesn't incorporate background noise is extended up to 5000 Hz as seen from section 4.1.

5.2 Monte Carlo Simulation Set Up

In this section, the Monte Carlo setup will be explained prior to conducting the actual simulation. The experimental model is evaluated using the Monte Carlo uncertainty analysis explained in section 3. The simulation is performed using the same simulation parameters and setup as those used in the analytical simulation described in section 4.1. Table 6 gives the model and signal processing settings used for the Monte Carlo simulation.

Uncertainty confidence level used:	95%
Overlap segment:	50 percent
Signal length:	1200000 samples
Signal time:	25 seconds
Mach number:	0.1712
Room Temperature:	293.05K
Frequency used for individual perturbed variables:	2kHz
Frequency Spectrum used for multivariate perturbations:	500Hz - 2.5kHz
Sampling Frequency:	48kHz
Monte Carlo iterations:	1000 and 500 for the multivariate perturbations
Effective segments used :	500 and 1000 for the CSM perturbation

Table 6: Experimental model simulation settings

The unperturbed nominal CBF output is shown in figure 29b. The region of interest is taken as such to avoid the near wall emitted sounds at $y = -0.345$ [m] and $y = 0.345$ [m].

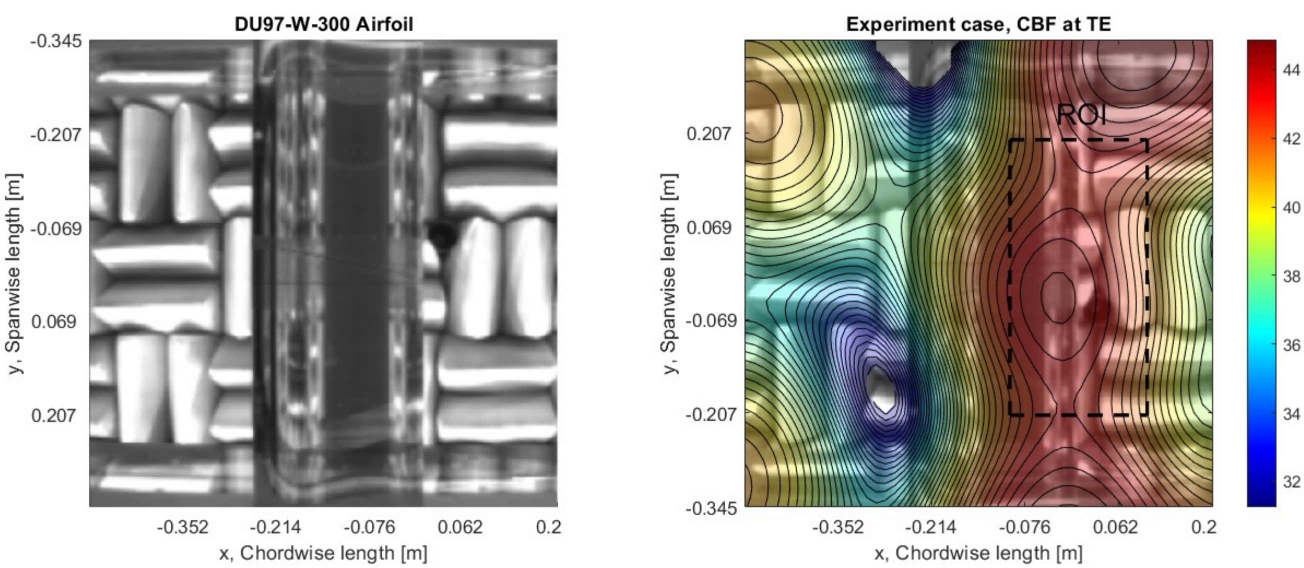

(a) (b)

Figure 29: Figure 29a shows the airfoil view from the array while figure 29b shows the CBF output result from the array for emitted sound waves of 2 kHz.

5.3 Monte Carlo Results

5.3.1 Microphone phase shift perturbation

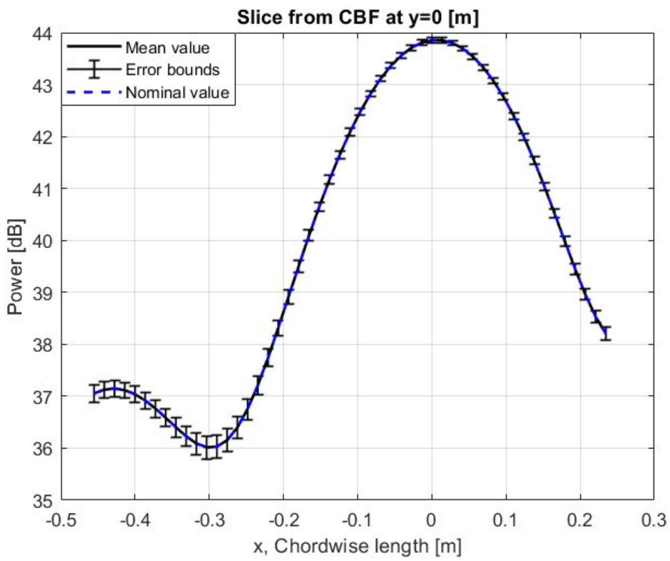

(a)

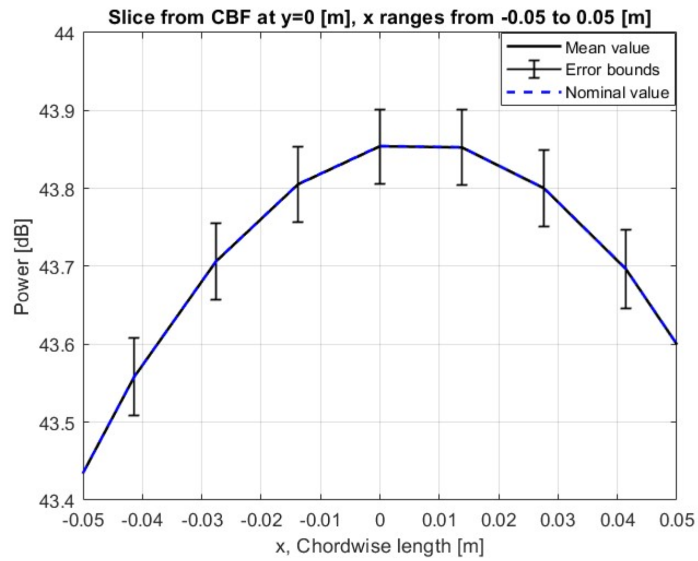

(b)

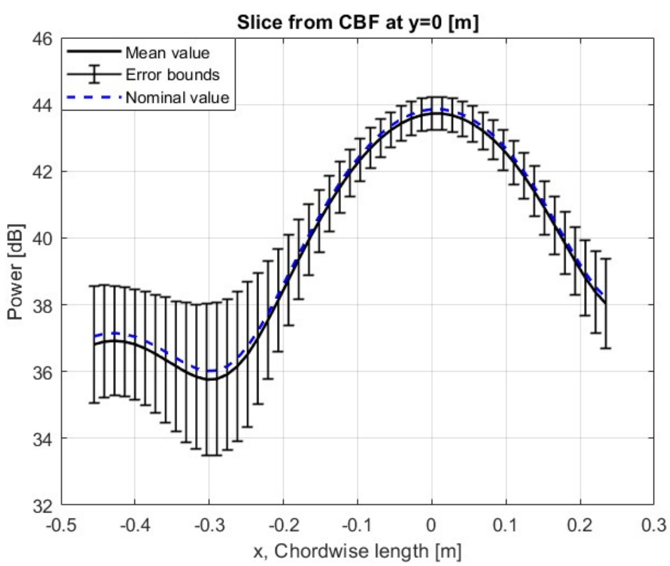

(c)

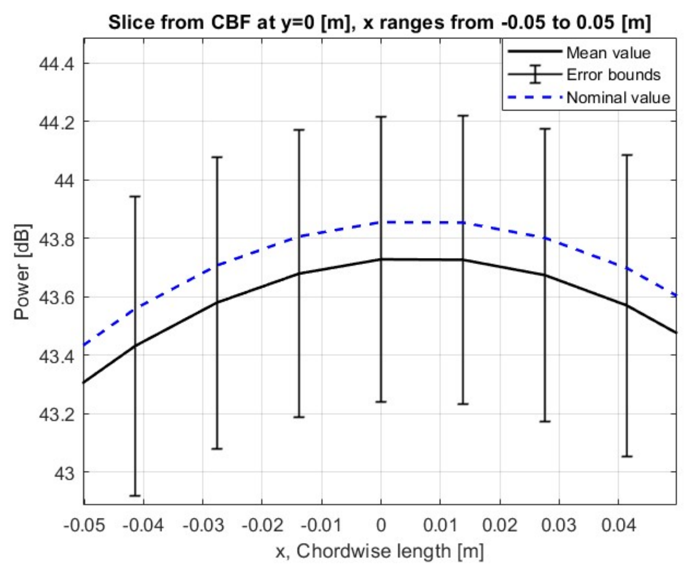

(d)

Figure 30: Quantified Uncertainty of CBF output, more specifically: Figure 30a shows microphone phase perturbations with a standard deviation of 1 degree, and figure 30b presents a closeup view of these perturbations. Similarly, figure 30c illustrates microphone phase perturbations with a standard deviation of 10 degree, while figure 30d shows a closeup view of that case.

In this section, the impact of microphone phase shifts is analyzed using a Monte Carlo simulation with 1000 iterations. As shown in figures 30a and 30b, a phase perturbation of 1 degree makes the CBF output to vary within 0.1 dB at the source location ($x = y = 0$ [m]) with 95 % confidence, where the standard deviation is 0.02 dB. Moving away from the source to $x = -0.2$ [m], the standard deviation increases to around 0.05 dB, and the CBF output varies by approximately 0.2 dB, that can be seen in more detail with the statistical summary in table 19a.

In addition, increasing the phase perturbation to 10 degree results in a standard deviation of 0.25 dB at the source location, with the sound pressure level varying by approximately 1 dB, as shown in figures 30c and 30d. Moving farther away from the sound origin, at $x = -2$ [m], the standard deviation increases significantly to around 0.54 dB, with the sound pressure level variation reaching to 1.12 dB. These results are detailed in the statistical summary shown in table 19b.

For both CBF Monte Carlo simulations corresponding to the 1 and 10 degree phase perturbations, the SPL gaussian distribution of those simulations can be seen with figures 50a and 50b respectively.

5.3.2 Microphone sensitivity perturbation

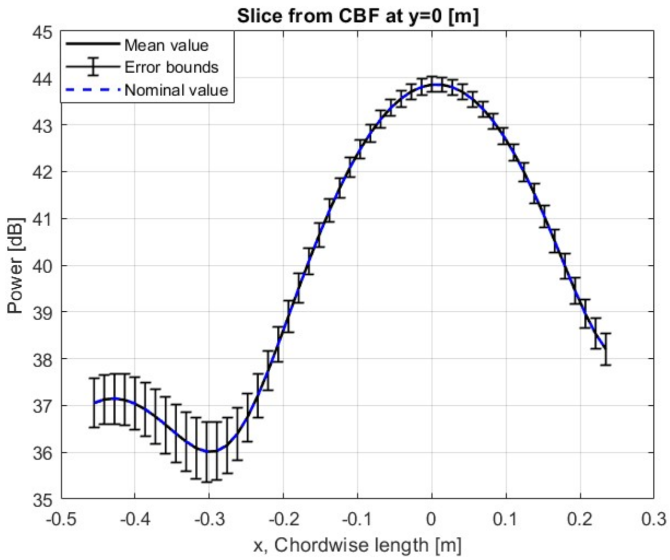

(a)

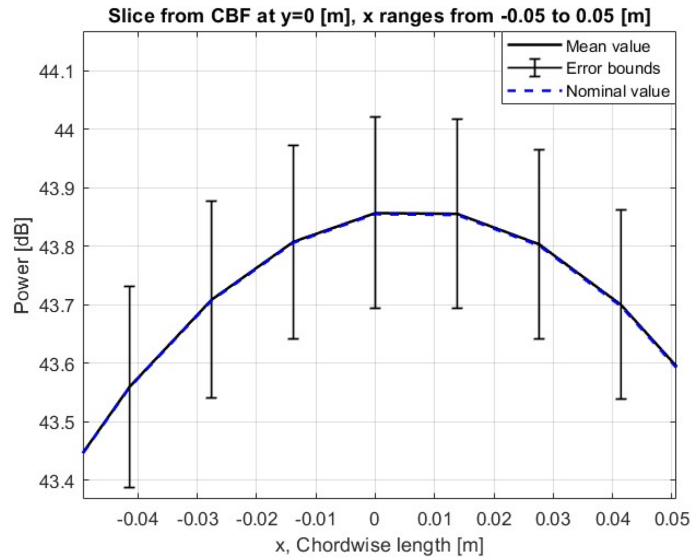

(b)

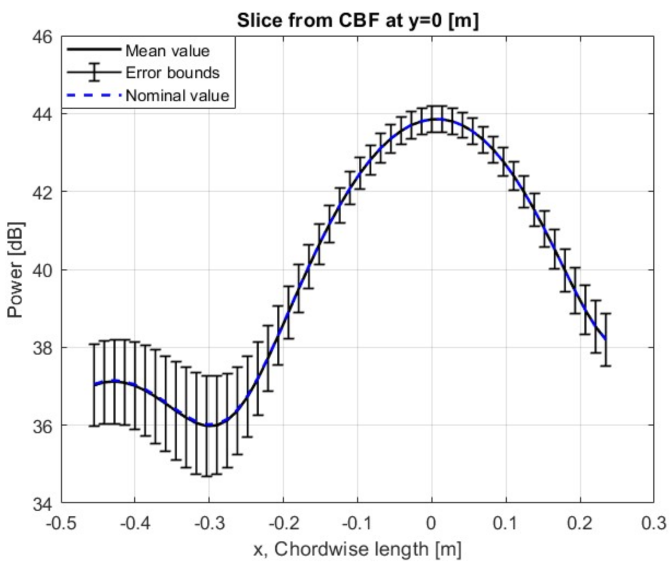

(c)

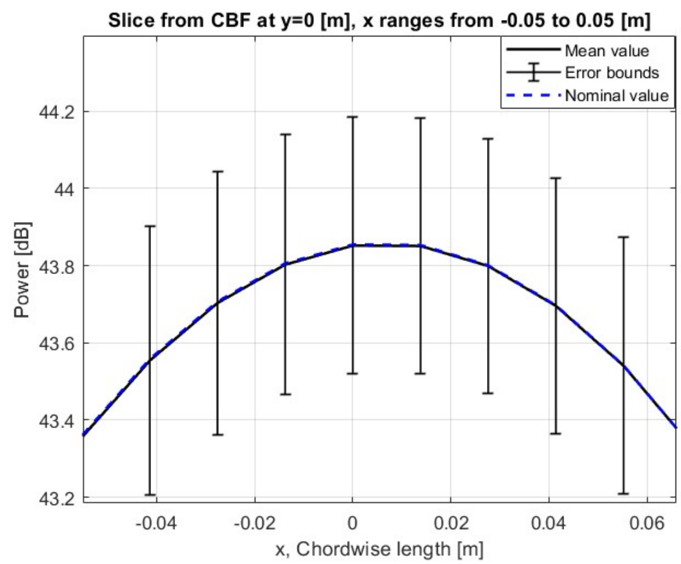

(d)

Figure 31: Quantified Uncertainty of CBF output, more specifically: Figure 31a shows microphone sensitivity perturbations of 5 %, and figure 31b presents a closeup view of these perturbations. Similarly, figure 31c illustrates microphone sensitivity perturbations of 10 %, while figure 31d shows a closeup view of that case.

In this section, the impact of microphone sensitivity perturbations is analyzed. As shown in figures 31a and 31b, a sensitivity perturbation of 5% of the nominal microphone sensitivity is applied independently to each microphone. This causes the CBF output to vary within 0.32 dB at the source location ($x = y = 0$ [m]), with a standard deviation of approximately 0.08 dB. Moving away from the source to $x = -0.2$ [m], the standard deviation increases to about 0.14 dB, and the SPL variation reaches approximately 0.5 dB. These results are further detailed in the statistical summary from table 20a.

Furthermore, increasing the sensitivity perturbation to 10% of the nominal microphone sensitivity, results in a standard deviation of 0.17 dB at the source location, with the sound pressure level varying by approximately 0.7 dB, as shown in figures 31c and 31d. Moving farther away from the sound source, at $x = -2$ [m], the standard deviation increases slightly to 0.29 dB, with the variation in SPL reaching 1.3 dB. These results are detailed in the statistical summary shown in table 20b.

For both CBF Monte Carlo simulations corresponding to the 5 and 10 % sensitivity perturbations, the SPL gaussian distribution of those simulations can be seen with figures 51a and 51b respectively.

5.3.3 Microphone location perturbation

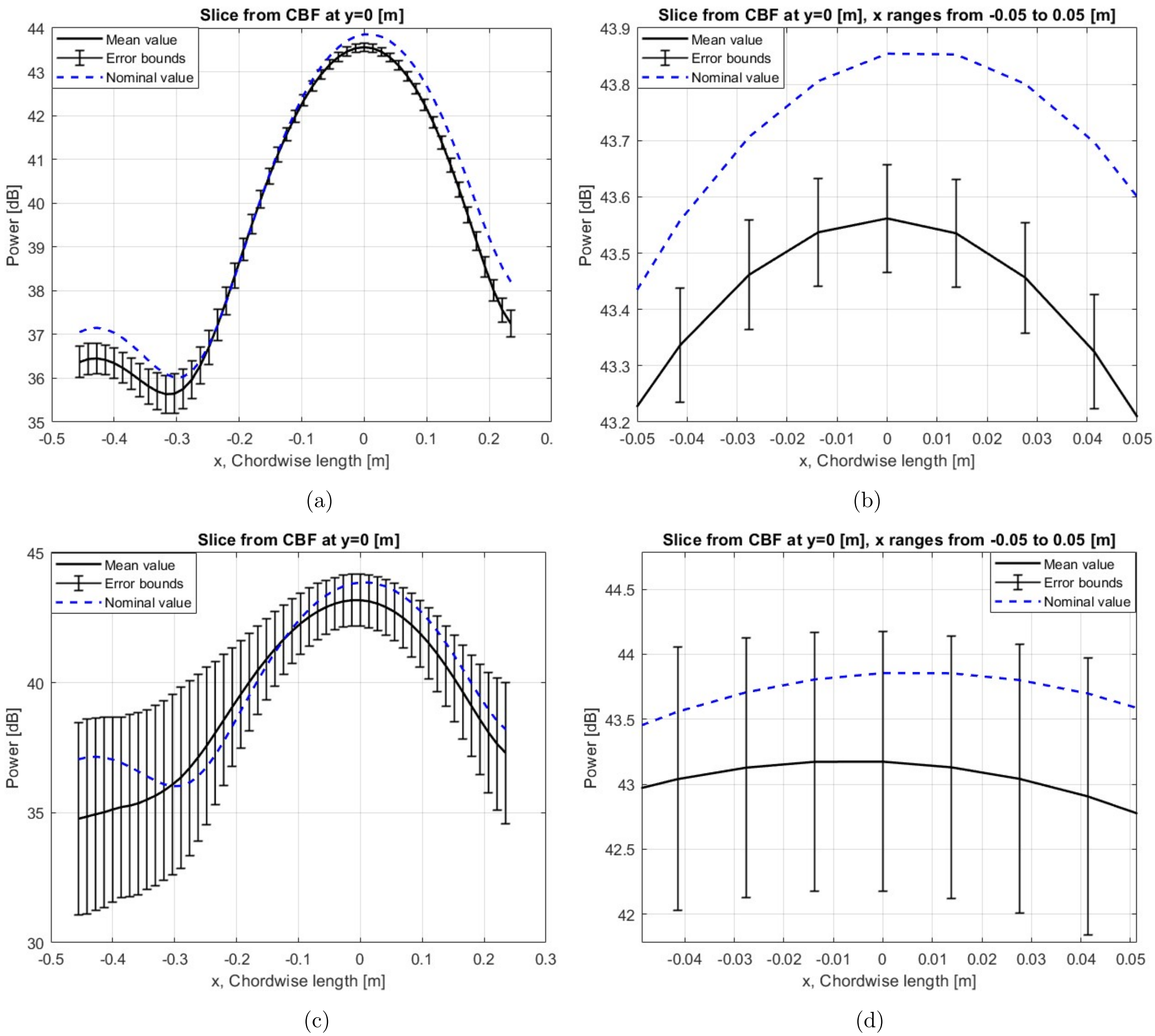

Figure 32: Quantified Uncertainty of CBF output, more specifically: Figure 32a shows microphone location perturbations of 1mm, and figure 32b presents a closeup view of these perturbations. Similarly, figure 32c illustrates microphone location perturbations of 10 mm, while figure 32d shows a closeup view of that case.

In this section, the impact of microphone coordinate perturbations is analyzed. As shown in Figures 32a and 32b, each microphone coordinate is individually perturbed by 1 mm relative to its nominal position. This causes the CBF output to vary within 0.2 dB at the source location ($x = y = 0$ [m]), with a standard deviation of approximately 0.05 dB. Its important to note that the nominal value at the sound source is 0.25 dB above the mean of the perturbed sound pressure level and 0.15 dB above the upper bound at 95 % confidence. This could be due to the fact that perturbing the microphones, increases sidelobes, and therefore reducing the energy in the main lobe. Moving away from the source to $x = -0.2$ [m], the standard deviation increases to about 0.1 dB, and the CBF output variation reaches approximately 0.4 dB. These results are further detailed in the statistical summary from table 21a.

Moreover, increasing the position perturbations to 10 mm of the nominal microphone positions, results in a standard deviation increasing significantly to around 0.5 dB at the source location, with the sound pressure level varying by approximately 2 dB, as shown in figures 32c and 32d. Moving farther away from the sound source, at $x = -2$ [m], the standard deviation increases even more to 0.87 dB, with the variation in sound pressure level reaching 3.4 dB. The perturbation of microphone locations is the largest impact on the CBF output observed till now. These results are detailed in the statistical summary shown in table 21b.

For both CBF Monte Carlo simulations corresponding to the 1 and 10 mm position perturbations, the SPL gaussian distribution of those simulations can be seen with figures 52a and 52b respectively.

5.3.4 Array broadband distance perturbation

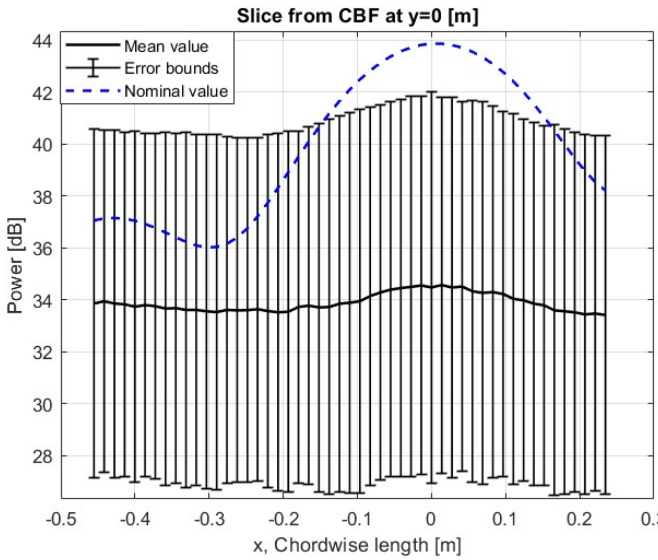

(a)

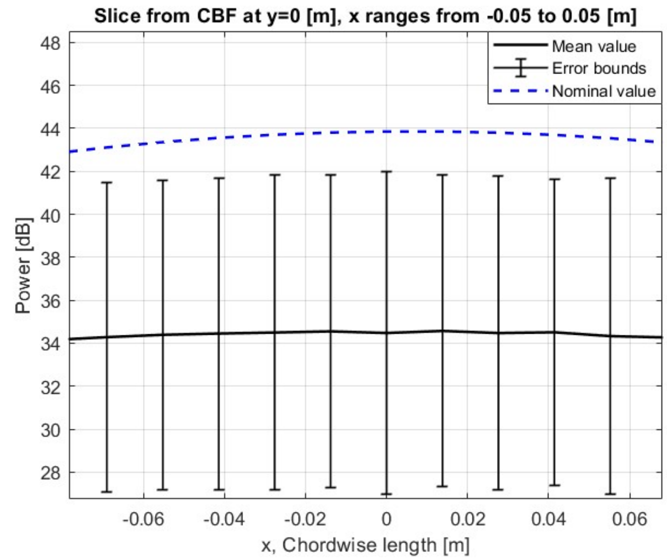

(b)

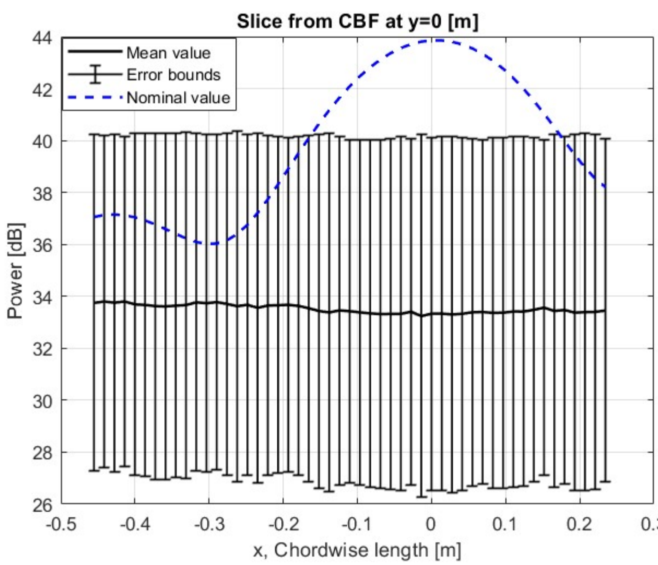

(c)

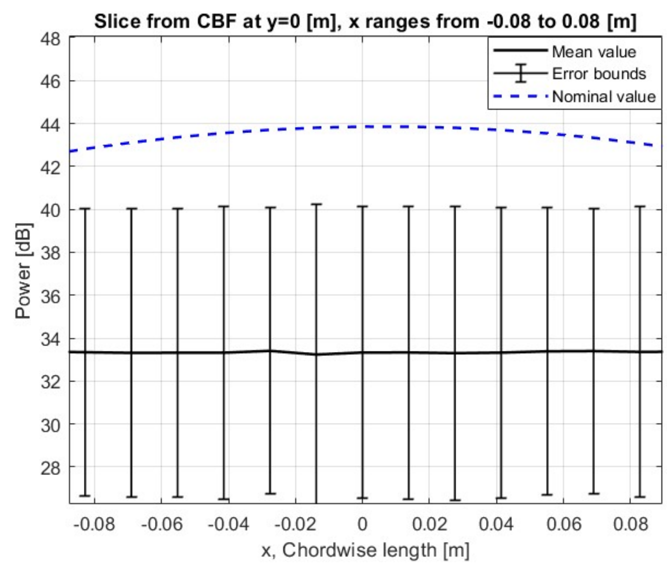

(d)

Figure 33: Quantified Uncertainty of CBF output, more specifically: Figure 33a shows the array broadband distance perturbed with a standard deviation of 45mm (2.5%), and figure 33b presents a closeup view of these perturbations. Similarly, figure 33c illustrates the array broadband distance perturbed with a standard deviation of 90 mm (5%), while figure 33d shows a closeup view of that case.

Here, the impact of array broadband distance perturbations is analyzed. As shown in Figures 33a and 33b, each microphone's z axis coordinate is individually perturbed with 2.5 % of the nominal array distance (1.801m) to the trailing edge. That causes the CBF output to vary significantly with a range of 14.62 dB at the source location ($x = y = 0$ [m]), with a standard deviation of around 3.73 dB. The error bounds do not change significantly with increasing distance from the source as can be seen from the statistical summary from table 22a.

Increasing the array broadband perturbations to 5% of the nominal array distance (1.801m) to the trailing edge, results in a standard deviation slightly decreasing to around 3.39 dB at the source location as shown in figures 33c and 33d. For both the 2.5 and 5 % perturbations, the uncertainty in the CBF output remains high. From the figures corresponding to the 2.5 % perturbations, it can be seen that the source can still be localized. However, with the increased perturbations of 5 %, the source cant be localized anymore. This indicates that not using the exact broadband distance of the array into the beamforming algorithm can introduce significant uncertainty into the CBF output. A detailed statistical summary is provided in Table 22b.

For both CBF Monte Carlo simulations corresponding to the 2.5 % and 5 % perturbations, the SPL gaussian distribution of those simulations can be seen with figures 53a and 53b respectively.

5.3.5 Temperature perturbation

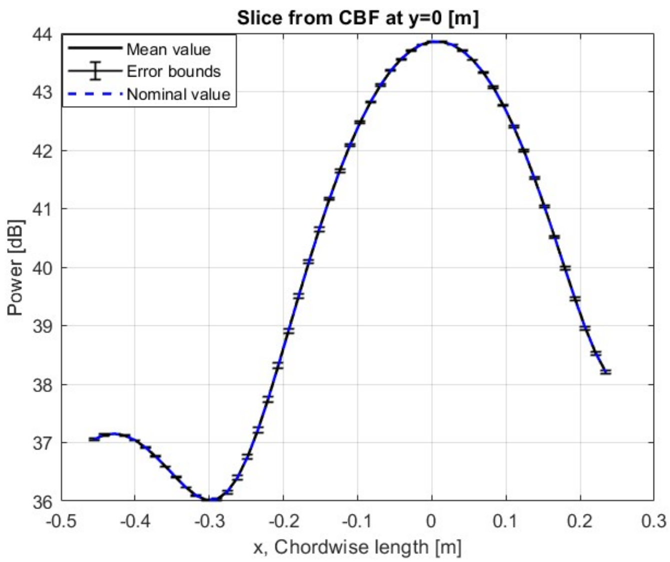

(a)

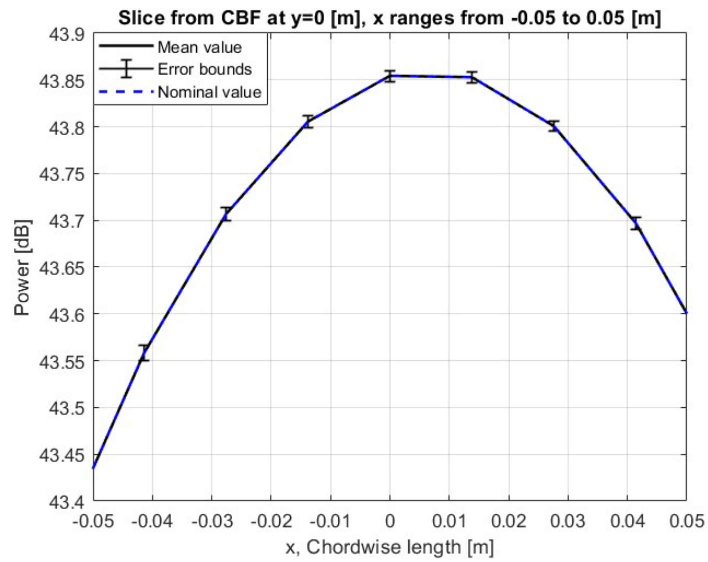

(b)

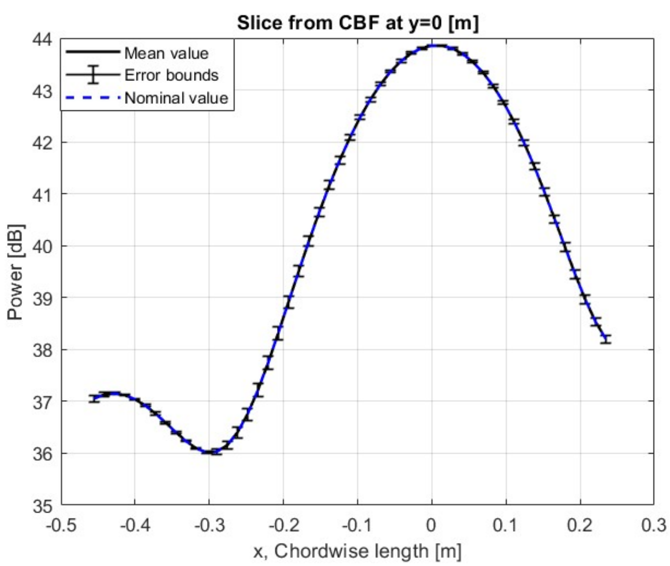

(c)

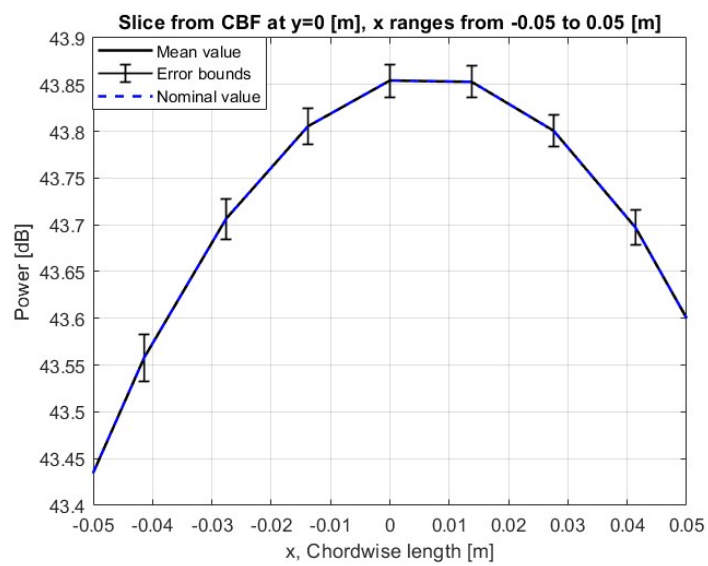

(d)

Figure 34: Quantified Uncertainty of CBF output, more specifically: Figure 34a shows the temperature perturbed with a standard deviation of 1 kelvin, and figure 34b presents a closeup view of these perturbation. Similarly, figure 34c illustrates the temperature perturbed with a standard deviation of 3 kelvin, while figure 34d shows a closeup view of that case.

In this section, the impact of the temperature perturbation is analyzed. As shown in Figures 34a and 34b, by perturbing the temperature within 1 kelvin, the CBF output doesn't significantly vary. The sound pressure level varies within a range of 0.02 dB at the source location ($x = y = 0$ m), with a standard deviation of approximately 0.004 dB. The error bounds don't change significantly with increasing the distance from the source in chordwise direction, where the sound pressure level varies within a range of 0.08 dB. A more detailed overview of the temperature uncertainty in the CBF output within a range of x axis chordwise selected points from the CBF output map is provided in the statistical summary, table 23a.

Increasing the Temperature perturbations to 3 kelvin of the nominal temperature, results into the standard deviation increasing to around 0.01 dB at the source location as shown in figures 34c and 34d. Specifically, the sound pressure level varies within a range of 0.04 dB. Going further away from the source at $x = -0.2[m]$, it can be seen that the sound pressure level varies within a range of 0.2 dB, with a standard deviation of around 0.05 dB. A detailed statistical summary is provided in table 23b.

For both CBF Monte Carlo simulations corresponding to the 1 and 3 kelvin perturbations, the SPL gaussian distribution of those simulations can be seen with figures 54a and 54b respectively.

5.3.6 Cross spectral matrix perturbation

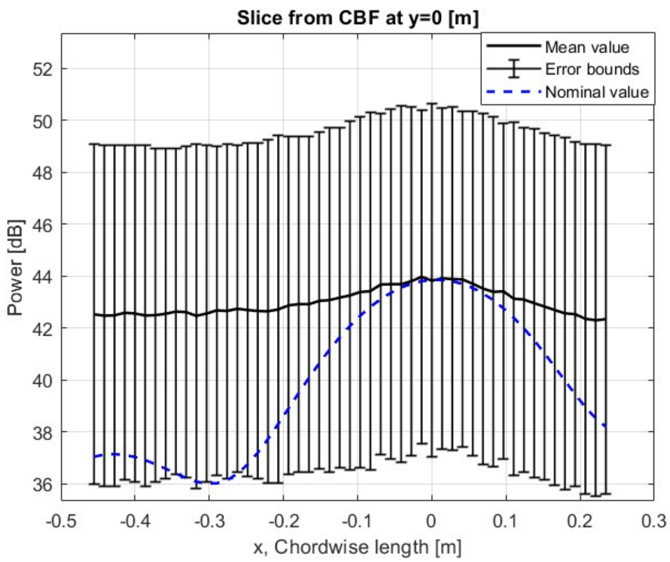

(a)

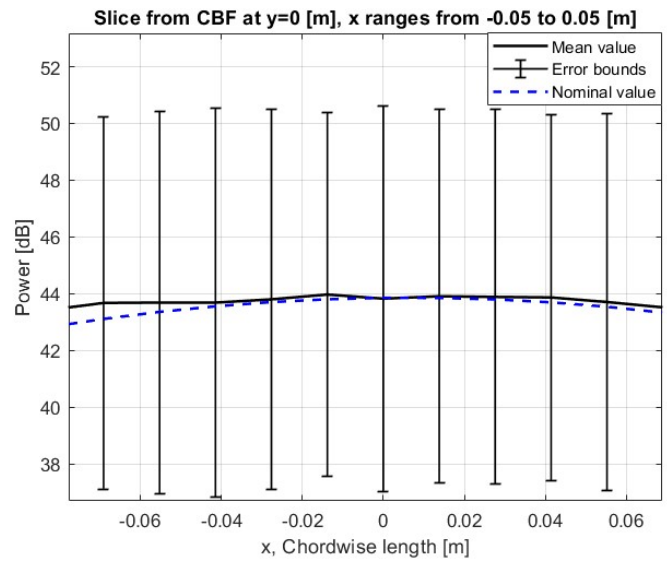

(b)

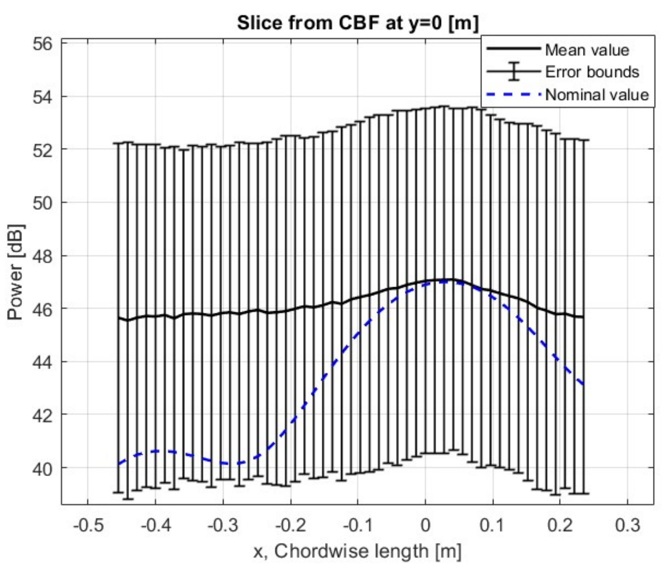

(c)

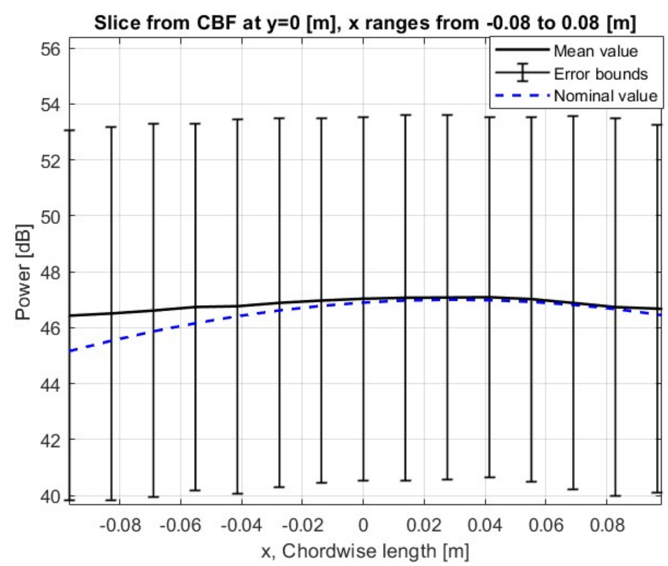

(d)

Figure 35: Quantified Uncertainty of CBF output, more specifically: Figure 35a shows the CSM perturbed with 500 effective blocks, and figure 35b presents a closeup view of these perturbations. Similarly, figure 35c illustrates the CSM perturbed with 1000 effective blocks, while figure 35d shows a closeup view of that case.

Finally, the cross spectral matrix is perturbed in this section. As shown in figures 35a and 35b, by perturbing the CSM with using 500 effective segments, the CBF output significantly varies. The sound pressure level varies within a range of 13.42 dB at the source location ($x = y = 0$ m), with a standard deviation of approximately 3.42 dB. It can be observed that the CBF output with the perturbed CSM still localizes the sound source, as shown by the existence of a lobe in figure 35a, which also aligns with the main lobe of the nominal value. The error bounds don't change significantly with increasing the distance from the source in chordwise direction, where the sound pressure level still varies within a range of 13 dB. A more detailed overview of the CSM uncertainty in the CBF output is provided in the statistical summary in table 24a.

Increasing the number of effective segments to 1000 for processing and perturbing the CSM, the perturbed CBF output is seen in figures 35c and 35d. That results in a slight decrease in standard deviation to 3.36 dB at the source location. Specifically, the sound pressure level varies within a range of 13 dB. Further away from the source, at $x = -0.2$ m, the sound pressure level varies within a range of 12.8 dB, with a standard deviation of 3.28 dB. As observed, by increasing the amount of effective segments increases the amplitude at the source location and also reduces the uncertainty. A detailed statistical summary is provided in table 24b.

For both CBF Monte Carlo simulations corresponding to the CSM perturbations using 500 and 1000 effective segments, the SPL gaussian distribution of those simulations can be seen with figures 55a and 55b respectively.

5.4 Multi variable perturbation

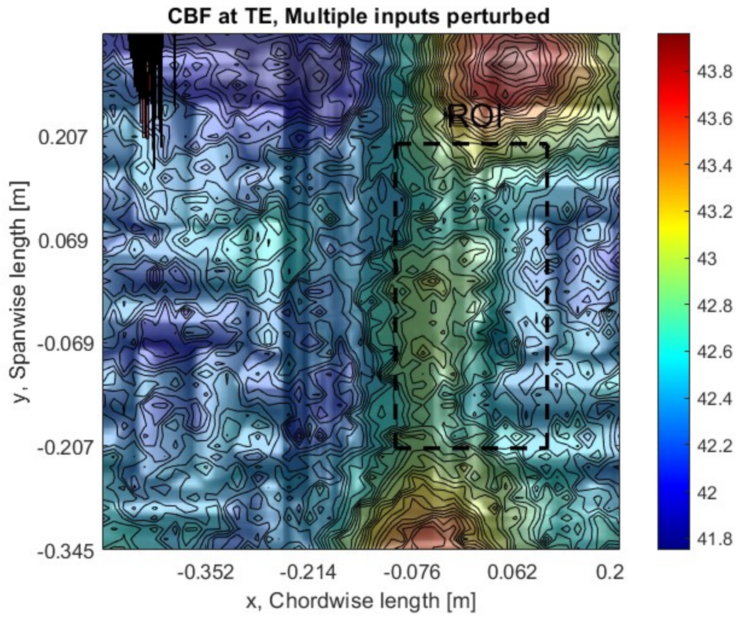

Figure 36: CBF output of the Monte Carlo simulation with multiple perturbed inputs for sound waves emitted at 2 kHz frequency

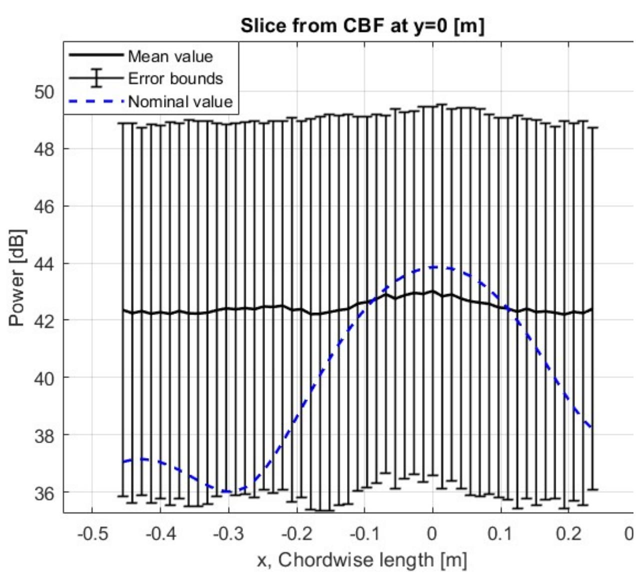

(a)

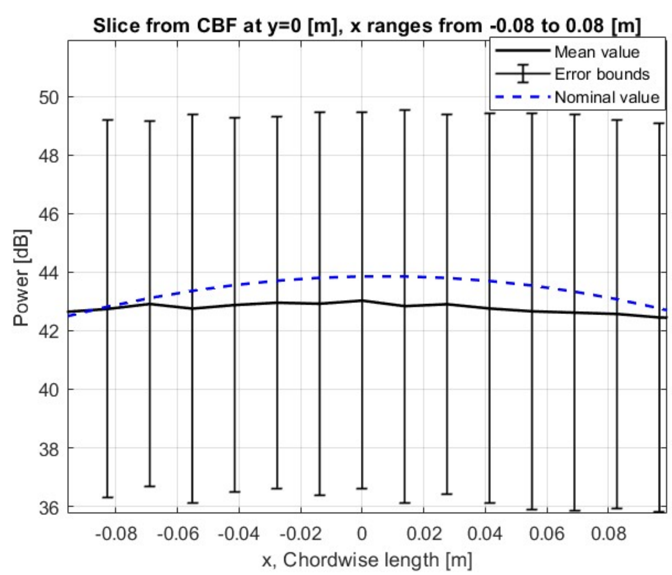

(b)

Figure 37: Figure 37a illustrates the error bounds of the CBF output, while figure 37b illustrates a closeup view of the same case.

In this section, all the variables are now simultaneously perturbed throughout the frequency spectrum using 500 Monte Carlo iterations. It was clear that perturbing the array broadband distance would create significant uncertainty in the CBF output. Therefore, a smaller perturbation amplitude of 10 mm was used for the array broadband distance. That was done by using the microphone location perturbation mechanism for all axis with a 10 mm standard deviation. This value comes from the fact that a laser distance meter is used to position the array with an accuracy of within 1 mm. However, due to the spiral shaped array, the branches which hold the microphones may deviate from the z axis and hence 10 mm is considered as worst case. The perturbation settings that are used are the same as those applied in the analytical line source model from section 4.3.7. All perturbations are performed using 500 effective segments. For emitted sound waves from the TE at 2 kHz, the CBF output is shown in figure 36. At this frequency, the uncertainty bounds around the mean of the 500 Monte Carlo iterations are illustrated in figures 37a and 37b. Specifically, at the source location ($x = y = 0$ m), the standard deviation is approximately 3.28 dB, and the sound pressure level varies by about 12.85 dB. From all perturbation mechanisms, the CSM perturbation has the largest impact on the CBF uncertainty results. A statistical summary of the Monte Carlo simulation is provided in table 17 for all frequencies tested during the experiment (500 to 2500 Hz). Finally, the power spectral density is performed by integrating the sound power over a region of interest as explained in section 2.6, the sound power is then converted to logarithmic dB scale with equation 10. The PSD is presented in figure 38. Starting from a SPL variation of approximately 1 dB at 0.5 kHz, the variation increases with frequency, as expected. The SPL uncertainty reaches approximately 6.8 dB at 2.5 kHz. A statistical summary of the Monte Carlo simulation for the integrated sound power is provided in table 18 for all frequencies tested during the experiment (500 to 2500 Hz).

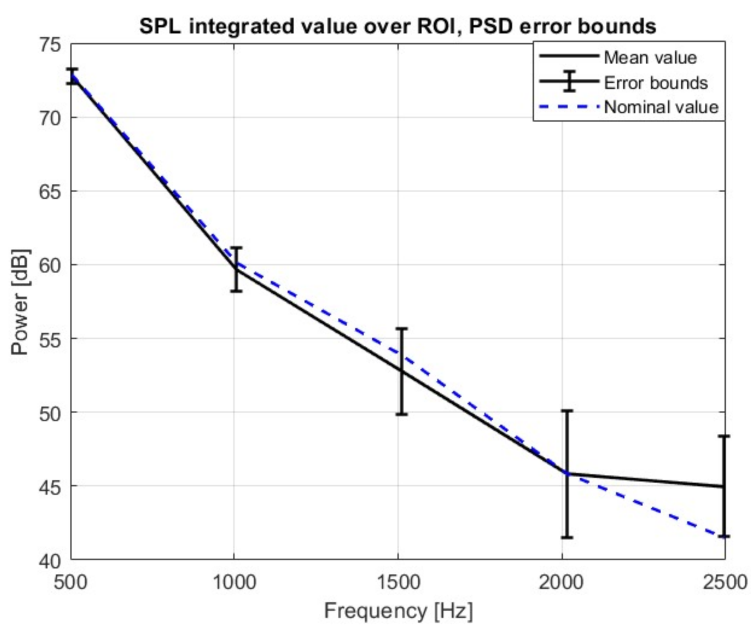

Figure 38: SPL of the integrated sound power across the frequency spectrum defined from section 5.1.5, along with its error bounds, from the Monte Carlo multivariate perturbation simulation.

6 Discussion

From the experimental model, the high uncertainty level caused from the cross spectral matrix, which leads to the sound power to vary within 13.2 dB, is mainly due to the fact that a low signal to noise ratio SNR of around 7 dB was present during the measuring as seen from figure 28. This low SNR comes from the fact that there is an important contribution of background noise. This background noise causes the microphones to capture not only the intended signal but also unrelated noise sources from the Trailing edge noise of the Airfoil. As a result from that, the spectral signal from all of the microphones have bad coherence, and that leads to a significant increase in uncertainty to the CBF output. In addition, the airfoil used in the experiment had a large camber. To minimize the lift and to reduce the risk of additional noise mechanisms, a low angle of attack was used. However, the airfoil still generated other noise mechanisms, and that contributed to the background noise, which interfered with the TE sound mechanism which was the focus of this research. Also, the wind tunnel's test chamber, had exposed screws and wall voids, which may also have further increased the background noise. Unfortunately, an alternative airfoil with lower camber was not available. As a recommendation for future studies, an airfoil with reduced camber should be used to minimize background noise and hence improving measurement quality. Finally, implementing a microphone calibration method could enhance the spectral coherence between all the microphones. A speaker would be required to be placed inside the wind tunnel with no flow being present, near the airfoil's position. The speaker would then play sounds at given frequencies to simulate noise. This process would help in determining the microphone response and would allow for the creation of a correction factor before beamforming occurs to correct the microphones recording the sound pressure.

For the analytical model because of the computational limitations, only 70000 samples were used for creating a time pressure signal, compared to 1200000 samples recorded in the experimental case. This leads to a relatively poor frequency resolution of 171 Hz. Consequently, when I had to analyze the CBF for a specific frequency, the closest discrete frequency which was available from the sampled data had to be used, and that introduced additional limitations to the model's precision.

In conclusion, with these recommended improvements, a more sophisticated model could be developed to more accurately quantify the uncertainty intervals of the conventional beamforming algorythm and localizing the sound sources on a flying aircraft or other flying objects.

7 Conclusions

The Monte Carlo simulations for both the analytical model and the experimental case are designed to capture the worst case uncertainty in the beamforming parameters. Therefore, the uncertainty bounds of the integrated sound power which is computed across the full frequency spectrum is representing the upper bounds of potential error. The analytical model has evaluated how specific variable uncertainties (discussed in section 3.1) impact the fundamental beamforming design, without being influenced by any real world factors such as background noise. In contrast, the experimental model evaluated how those variable uncertainties impacted the CBF output differently under real conditions.

7.1 Analytical line source CBF

The uncertainty of the analytical line source beamforming model was evaluated. It was shown that the uncertainty of the Conventional Beamforming output was relatively small for both low and high perturbation levels of each input variable used. Each simulation took six hours around to complete 1000 iterations.

Considering only the quantified uncertainty at the trailing edge location of the mid-span ($x = y = 0$), the CBF output uncertainty was found to be most impacted by microphone sensitivity perturbations. The microphone sensitivity perturbations created a variation by ±0.16 dB around the perturbed computed mean in sound pressure level with using a 95 % confidence level at 10 percent perturbation of the nominal microphone sensitivity for sound waves emitted at 2 kHz from the TE. Those were followed by the microphone phase perturbations, which were the second largest contribution of uncertainty to the CBF output. Perturbing the microphone phases with a standard deviation of 10 degree caused a sound pressure level variation by ±0.11 dB at 2kHz.

Afterwards, all variables (discussed in section 3.1) were perturbed simultaneously by considering the largest possible perturbations for input variable used. For the multivariate perturbed CBF output with a 95% confidence level, the uncertainty bounds were approximately ±0.19 dB around the mean at 2 kHz. Now considering the quantified uncertainty over an area around the trailing edge (ROI), the integrated sound power variation around the mean was evaluating over the frequency range of 500 to 5000 Hz. At 2 khz the sound varied by ±0.23 dB and as the frequency increased further, at 5 kHz the SPL variation of the integrated sound power reached ±1.38 dB around the mean.

7.2 Experimental CBF

This section concludes the uncertainty analysis of the experimental model. Each simulation took 11 hours around to complete 1000 iterations. The uncertainty analysis was performed at a 95 % confidence level. The most dominant contributions to the simulation uncertainty are coming from the cross spectral matrix and array broadband distance perturbations.

For sound waves emitted at 2 kHz from the TE, considering only the quantified uncertainty at the trailing edge location of the mid-span ($x = y = 0$), for the perturbed CSM, the input variable leads the sound pressure level to have a variation of ±6.69 dB around the perturbed computed mean. By increasing the amount of effective segments, only slightly reduces this uncertainty, with the variation decreasing to ±6.58 dB. In addition, perturbing the array broadband distance by 45 mm uncertainty leads to a sound pressure level variation of ±7.31 dB. Increasing the perturbation to 90 mm doesn't increase the variation in SPL but completely delocalizes the source. Besides from those two dominant perturbation mechanisms, the microphone locations being perturbed is the third largest contributor to the uncertainty in the beamforming output. At 2kHz, a worst case perturbation of 10 mm to all microphones introduces a sound pressure level variation of ±1 dB.

After all variables were perturbed simultaneously, the sound pressure level varied within ±1.69 dB at 1 kHz. Increasing the frequency to 2.5 kHz enhanced the sound pressure level variation to ±5.99 dB. This study indicates that with increasing frequency from the sound source leads to greater uncertainty in the sound power estimation. Now considering the quantified uncertainty over an area around the trailing edge (ROI), integrating the sound power over the region of interest, the SPL variation of the integrated sound power at 1 kHz is ±1.46 dB. Increasing the frequency to 2.5 kHz increases the uncertainty of the CBF output to ±3.40 dB around the trailing edge of the airfoil.

References

[1] R.K. Amiet. Refraction of sound by a shear layer. *Journal of Sound and Vibration*, 58:467–482, 07 1978.

[2] Christopher J. Bahr, William M. Humphreys Jr., Daniel Ernst, Thomas Ahlefeldt, Carsten Spehr, Antonio Pereira, Quentin Leclère, Christophe Picard, Ric Porteous, Danielle J. Moreau, Jeoffrey Fischer, and Con J. Doolan. A comparison of microphone phased array methods applied to the study of airframe noise in wind tunnel testing. *AIAA/CEAS Aeroacoustics Conference, AIAA Aviation Forum*, 23rd:12–16, June 2017.

[3] Knox Eugene C Braslow Albert L. Simplified method for determination of critical height of distributed roughness particles for boundary-layer transition at mach numbers from 0 to 5. *NASA Technical Reports Server*, pages 10–16, 09 1958.

[4] Andrew Bray and Mine Çetinkaya Rundel. Foundations for statistical inference - confidence intervals. https://www2.stat.duke.edu/courses/Spring16/sta101.001/post/labs/confidence_intervals.html. Accessed 12/11/2024.

[5] Matlab Help center. Spectrogram using short-time fourier transform. https://nl.mathworks.com/help/signal/ref/spectrogram.html. Accessed 12/11/2024.

[6] PAUL K. CHANG. Chapter ii - steady separation of incompressible laminar flow from two-dimensional surfaces. *Science direct*, pages 55–60, 02 1970.

[7] Tarik Yardibi Fei Liu § Drew Wetzel Brandon Bertolucci Chris Bahr, Nikolas S. Zawodny and Louis Cattafesta. Shear layer time-delay correction using a non-intrusive acoustic point source. *International Journal of Aeroacoustics*, 23:1–32, 10 2011.

[8] Leandro de Santana. Fundamentals of acoustic beamforming. *ST organization*, pages 1–26, - -.

[9] Richard Fitzpatrick. Approximate solutions of boundary layer equations. *Professor of Physics The University of Texas at Austin*, page 1, 03 2016.

[10] Richard Fitzpatrick. Von kármán momentum integral. *Professor of Physics The University of Texas at Austin*, page 1, 03 2016.

[11] geeksforgeeks contributors. Standard normal distribution. https://www.geeksforgeeks.org/standard-normal-distribution/. Accessed 12/11/2024.

[12] B D Hall. Calculating measurement uncertainty for complex-valued quantities. *Measurement science and technology*, 14:368–375, 09 2002.

[13] A. Belšak M. Čudina J. Prezelj, P. Lipar. On acoustic very near field measurements. *Mechanical Systems and Signal Processing*, 40:194–207, 02 2012.

[14] Cansev Küçükosman. Semi-analytical approaches for the prediction of the noise produced by ducted wind turbines. *TU Delft*, pages 15–20, 01 2019.

[15] Olivier Ledoit. Honey, i shrunk the sample covariance matrix. *UPF Economics and Business Working Paper*, 691:1–22, 11 2003.

[16] Thomas Fritsch Martin CR. Where does the 1.22 come from in rayleigh criterion for circular apertures. https://physics.stackexchange.com/questions/696980/where-does-the-1-22-come-from-in-rayleigh-criterion-for-circular-apertures. Accessed 12/11/2024.

[17] Daniel Saromo Mori Matias Valdenegro-Toro. A deeper look into aleatoric and epistemic uncertainty disentanglement. *Groningen University*, pages 1–11, 9 2021.

[18] Pieter; Carpio Alejandro Rubio; Zamponi Riccardo; Luesutthiviboon Salil; Malgoezar Anwar M.N.; Snellen Mirjam; Schram Christophe; Simons Dick G. Merino-Martínez, Roberto; Sijtsma. Integration methods for distributed sound sources. *Sage Journals Home*, 18:1–27, 06 2019.

[19] Stefan Oerlemans. Detection of aeroacoustic sound sources on aircraft and wind turbines. *University of Twente*, pages 1–40, 9 2009.

[20] Jérôme Antoni Quentin Leclere Pieter Sijtsma, Alice Dinsenmeyer. Beamforming and other methods for denoising microphone array data. *AIAA/CEAS Aeroacoustics conference*, pages 2–10, 05 2019.

[21] H. Pishro-Nik. 7.1.2 central limit theorem. https://www.probabilitycourse.com/chapter7/7_1_2_central_limit_theorem.php. Accessed 12/11/2024.

[22] Marijn Sanders. Study on the application of digital mems microphones for aeroacoustic noise source localization for large drones. *ST organization*, pages 10–12, 01 2017.

[23] Ennes Sarradj, Gert Herold, Pieter Sijtsma, Roberto Merino-Martinez, Anwar Malgoezar, Mirjam Snellen, Thomas F. Geyer, Christopher J. Bahr, Ric Porteous, Danielle J. Moreau, and Con J. Doolan. A microphone array method benchmarking exercise using synthesized input data. *AIAA/CEAS Aeroacoustics Conference, AIAA Aviation Forum*, AIAA 2017-3719:10–16, June 2017.

[24] Prof. Dr.-Ing. Heiko Schmidt and Prof. Dr.-Ing. Christoph Egbers. Benchmarking array analysis methods. *AIAA/CEAS Aeroacoustics Conference*, page 1, 06 2017.

[25] Pieter Sijtsma. Phased array beamforming applied to wind tunnel and fly-over tests. *National Aerospace Laboratory NLR*, pages 1–40, 12 2010.

[26] N. Zawodnyb F. Liub L.N. Cattafesta IIIb J.Lia T. Yardibia, C. Bahrb. Uncertainty analysis of the standard delay-and-sum beamformer and array calibration. *Journal of Sound and Vibration*, 329:1–29, 05 2009.

[27] Marco (2021) Taboga. "cholesky decomposition", lectures on matrix algebra. https://www.statlect.com/matrix-algebra/Cholesky-decomposition. Accessed 12/11/2024.

[28] CAE technical team support. microphone array bionic m 112 acoustic camera. https://pdf.directindustry.com/pdf/cae-software-und-systems-gmbh/microphone-array-bionic-m-112-acoustic-camera/188642-752191.html. Accessed 12/04/2025.

Appendices

A Wave equation derivation from balance equations

Starting with the mass equation:

$$\frac{\partial \rho}{\partial t} + \frac{\partial(\rho v_i)}{\partial x_i} = 0 \tag{62}$$

Linearising by replacing the density ρ with $\rho_0 + \rho'$ (where ρ_0 is a constant and ρ' is varying) and assuming that $\rho' << \rho_0$ for all acoustic waves:

$$\frac{\partial \rho}{\partial t} + \frac{\partial(\rho v_i)}{\partial x_i} = \frac{\partial \rho'}{\partial t} + \frac{\partial(\rho_0 v_i)}{\partial x_i} + \frac{\partial(\rho' v_i)}{\partial x_i} \approx \frac{\partial \rho'}{\partial t} + \rho_0 \frac{\partial(v_i)}{\partial x_i} \approx 0 \tag{63}$$

The mass equation is next differentiated with respect to space becoming:

$$\frac{\partial}{\partial t}\left(\frac{\partial \rho'}{\partial t}\right) + \frac{\partial}{\partial t}\left(\rho_0 \frac{\partial v_i}{\partial x_i}\right) \approx 0 \tag{64}$$

$$\approx \frac{\partial^2 \rho'}{\partial t^2} + \rho_0 \frac{\partial^2 v_i}{\partial x_i \partial t} \approx 0 \tag{65}$$

For small linear pressure perturbations in a stationary fluid: $p' = c_0^2 \rho'$:

$$\frac{1}{c_0^2} \frac{\partial^2 p'}{\partial t^2} \approx -\rho_0 \frac{\partial^2 v_i}{\partial x_i \partial t} \tag{66}$$

Now with the momentum equation:

$$\frac{\partial(\rho v_i)}{\partial t} + \frac{\partial(\rho v_i v_j + p_{ij})}{\partial x_j} = 0 \tag{67}$$

Applying Linearisation again:

$$\frac{\partial(\rho v_i)}{\partial t} + \frac{\partial(\rho v_i v_j + p_{ij})}{\partial x_j} \approx \tag{68}$$

$$\approx \rho_0 \frac{\partial v_i}{\partial t} + \frac{\partial(\rho_0 + \rho')(v_i v_j)}{\partial x_j} + \frac{\partial(p_0 + p')}{\partial x_i} \tag{69}$$

$$\approx \rho_0 \frac{\partial v_i}{\partial t} + \rho_0 \frac{\partial(v_i v_j)}{\partial x_j} + \frac{\partial \rho'(v_i v_j)}{\partial x_j} + \frac{\partial(p_0 + p')}{\partial x_i} \tag{70}$$

since ρ' is small:

$$\approx \rho_0 \frac{\partial v_i}{\partial t} + \rho_0 \frac{\partial(v_i v_j)}{\partial x_j} + \frac{\partial(p_0 + p')}{\partial x_i} \approx 0 \tag{71}$$

In a still standing fluid the mean pressure gradient is zero: $p_0 = 0$, hence:

$$\rho_0 \frac{\partial v_i}{\partial t} + \rho_0 \frac{\partial (v_i v_j)}{\partial x_j} + \frac{\partial p'}{\partial x_i} \approx 0 \tag{72}$$

Also the velocity perturbation of the wave is assumed to be small compared to the speed of sound. To this account:

$$\rho_0 \frac{\partial v_i}{\partial t} + \frac{\partial p'}{\partial x_i} \approx 0 \tag{73}$$

The momentum equation is then differentiated with respect to time:

$$\frac{\partial}{\partial xi}\left(\rho_0 \frac{\partial v_i}{\partial t}\right) + \frac{\partial}{\partial xi}\left(\frac{\partial p'}{\partial x_i}\right) \approx 0 \tag{74}$$

$$\approx \rho_0 \frac{\partial^2 v_i}{\partial xi \partial t} + \frac{\partial^2 p'}{\partial x_i^2} \approx 0 \tag{75}$$

Combining the mass and momentum equations, equations 66 and 75 respectively:

$$\frac{1}{c_0^2}\frac{\partial^2 p'}{\partial t^2} - \frac{\partial^2 p'}{\partial x_i^2} = 0 \; or \; \frac{1}{c_0^2}\frac{\partial^2 p'}{\partial t^2} - \nabla^2 p' = 0 \tag{76}$$

The wave equation shown above is also called the Alembert wave equation and is a pressure varying equation dependent on space and time. This equation, describes the propagation of small pressure disturbances in a homogeneous free field. By adding a sound source q to the equation, and multiplying it to the Dirac Delta function $\delta(\vec{x} - \vec{x_0})$ accounts for both generation and propagation of sound from a source. The non-homogeneous wave equation then becomes:

$$\frac{1}{c_0^2}\frac{\partial^2 p'}{\partial t^2} - \nabla^2 p' = q(t)\delta(\mathbf{x} - \mathbf{x_0}) \tag{77}$$

k is called the wave number and is symbolized as: $k = \omega / c_0 = 2\pi f_j / c0$. The solution of the non homogeneous free field equation is given as [8]:

$$p(\mathbf{x}, \mathbf{x_0}, t) = \frac{q(\mathbf{x_0}, t - \frac{||\mathbf{x} - \mathbf{x_0}||}{c_0})}{4\pi ||\mathbf{x} - \mathbf{x_0}||} \tag{78}$$

$\mathbf{x_0}$ is the source location and $\mathbf{x}$ is the observer location in the far field [8]. As can be seen from the equation, $4\pi||\mathbf{x} - \mathbf{x_0}||$ is the spherical spreading, and the larger the distance between the source $\mathbf{x_0}$ and the observer $\mathbf{x}$, the larger the spherical spreading factor is. Hence, the propagated pressure to the observer decreases as the sound wave travels by the spherical propagation factor [19].

B Frequency domain beamforming, sound power derivation

$$Z_o(f) = \sum_{m=1}^{N} v_{m,o} p_m(f) e^{-i\omega\delta t_{m,o}} \tag{79}$$

It can be rewritten as [8]:

$$Z_o(f) = g^{\dagger}_{m,o}(f) p_m(f) \tag{80}$$

Where $g_{m,o}(f)$ is the steering vector which is dependent on both the microphone with index notation m, grid search location with index notation o and on the frequency which the steering vector is operated at. The steering vector is:

$$g_{m,o}(f) = v_{m,o} e^{-2\pi i f \delta t_{m,o}} \tag{81}$$

The symbol † represents the complex conjugate of the complex value of $g_{m,o}$. Therefore the complex conjugate of $g_{m,o}$, is:

$$g^{\dagger}_{m,o}(f) = v_{m,o} e^{i2\pi f \delta t_{m,o}} \tag{82}$$

So far we have the output of the Conventional Beamformer $Z_o(f)$. To get the total power $L_o(f)$ of that output:

$$L_o(f) = |Z_o(f)|^2 \tag{83}$$

The total energy of a signal is split across positive and negative frequencies. However since a one-sided spectrum is used (see section 2.3) that accounts for only positive values. Therefore to account only for the positive values, the power output is divided by 2:

$$L_o(f) = \frac{1}{2} |Z_o(f)|^2 \tag{84}$$

$$= \frac{1}{2} Z_o(f) Z^*_o(f) \tag{85}$$

$$= \frac{1}{2} (g^{\dagger}_{m,o} p_m)(g^{\dagger}_{m,o} p_m)^* \tag{86}$$

$$= g^{\dagger}_{m,o} (\frac{1}{2} p_m p^{\dagger}_m) g_{m,o} \tag{87}$$

C Shear layer correction using Amiet theory

A challenge arises in the experimental setup that was not present in the analytical model, the airfoil is positioned within a potential flow interacting with the shear flow. As a result, the data obtained from the phased array does not account for shear layer effects, which can cause the apparent source location to be shifted downstream along the wind tunnel flow. To correct for this, Amiet's shear layer correction will be applied.

The deflection of the ray path representing the direction of sound propagation from the trailing edge depends on the thickness of the shear layer. In this section, a planar shear layer correction model developed by Amiet [1] will be discussed. This correction adjusts both the angle and the effective propagation distance of the sound wave, and consequently, it also modifies the amplitude recorded by the microphones. In the figure below (figure 39a), the shear layer effect is illustrated, showing a deflected acoustic ray, shown as being split into two segments of lengths r_1 and r_2 respectively. In the following section, a numerical solution will be presented for determining these ray lengths and the corresponding travel time $\delta_{t_{amiet}}$ for the sound wave along those paths. In figure 39b, the ray paths from each of the 33 microphones from the NASA 2 (Revision 2) experimental data benchmark from [24] are computed from the numerical method explained in this section. These rays travel through the shear layer, and as expected, the sound source appears shifted downstream in the flow when conventional beamforming is applied.

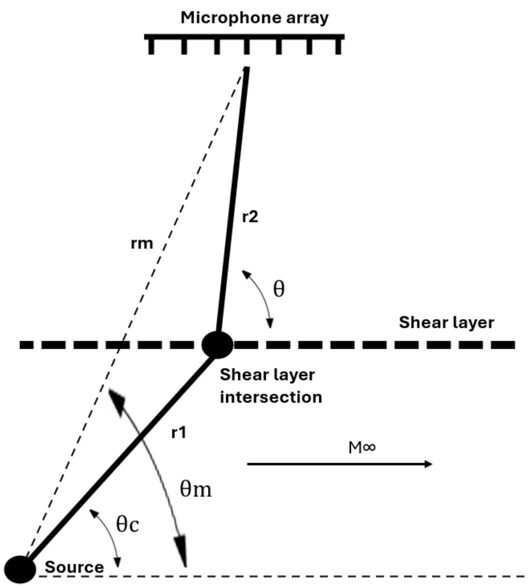

(a)

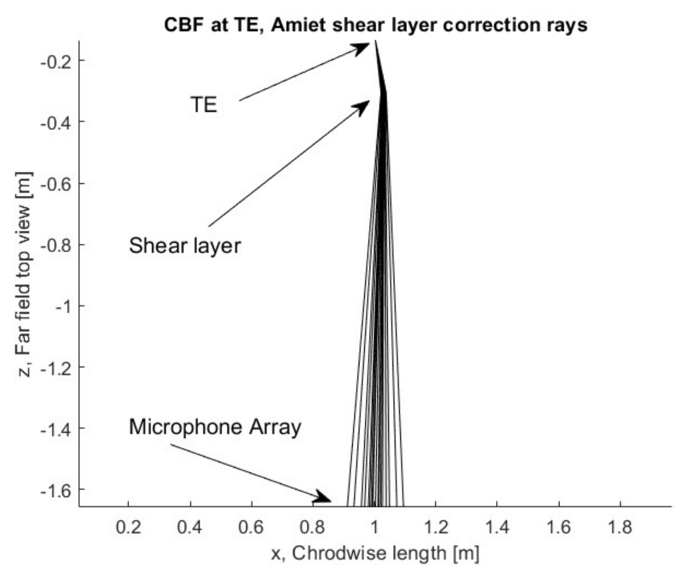

(b)

Figure 39: Figure 39a shows a schematic of the shear layer effect on a deflected acoustic ray, while figure 39b shows ray paths from all 33 microphones of NASA revision 2 benchmark to the sound source, the flow direction is from left to right in the chordwise direction of the airfoil

The microphone positions are denoted by x_m, y_m and z_m with microphone index m, while the shear layer intersection point where ray 1 and ray 2 meet is represented by the coordinates x_i, y_i, z_i with ray path index i.

The solution to Amiet's theory, as presented by Amiet [1], is obtained by solving the two equations.

$$F_0(x_i, y_i) = \frac{x_i}{\sqrt{x_i^2 + \beta^2(y_i^2 + z_i^2)}} - \beta^2 \frac{(x_m - x_i)}{\sqrt{(x_m - x_i)^2 + (y_m - y_i)^2 + (z_m - z_i)^2}} - M_x = 0 \tag{88}$$

$$F_1(x_i, y_i) = \frac{y_i}{\sqrt{x_i^2 + \beta^2(y_i^2 + z_i^2)}} - \frac{(y_m - y_i)}{\sqrt{(x_m - x_i)^2 + (y_m - y_i)^2 + (z_m - z_i)^2}} = 0 \tag{89}$$

In addition for the speed of sounds of c_0 and c_1 corresponding to ray 2 and ray 1 respectively:

$$c_0^2 = c_{0_x}^2 + c_{0_y}^2 + c_{0_z}^2 \tag{90}$$

$$c_1^2 = c_{1_x}^2 + c_{1_y}^2 + c_{1_z}^2 \tag{91}$$

The speed of sound in the air region through which ray 2 travels is known. However, in the air region where ray 1 travels, the speed of sound c_1 may differ and must be determined accordingly due to the shear layer being present. Where looking at the geometric relations from figure 39a, C. Bahr gives those relations [7] :

$$c_{0_x} = c_{1_x} - U_\infty = c_1 \frac{x_i}{\sqrt{x_i^2 + y_i^2 + z_i^2}} - M_\infty c_0 \tag{92}$$

$$c_{0_y} = c_{1_y} = c_1 \frac{y_i}{\sqrt{x_i^2 + y_i^2 + z_i^2}} \tag{93}$$

$$c_{0_z} = c_{1_z} = c_1 \frac{z_i}{\sqrt{x_i^2 + y_i^2 + z_i^2}} \tag{94}$$

Substituting those equations above (92- 94), c_1, c_0 and x_i,y_i and z_i relations can be found:

$$c_1 = \frac{x_i}{\sqrt{x_i^2 + y_i^2 + z_i^2}} M_\infty c_0 + \sqrt{\left(\frac{x_i}{\sqrt{x_i^2 + y_i^2 + z_i^2}} M_\infty c_0\right)^2 + c_0^2 - (M_\infty c_0)^2} \tag{95}$$

First the search grid and microphone location is defined along with a given speed of sound c_0, Mach number M_∞ and shear layer location z_i. Afterwards, F_1 and F_0 are then evaluated numerically for x_i and y_i. Once x_i and y_i are determined, they are then filled in the equation 95 and c_1 is then found. By defining the shear layer intersection coordinates (x_i and y_i), the ray distances r_1 and r_2 can be calculated using the Euclidean distance formula. The speed of sound c_1 is then used to compute the ray total propagation time $\delta_{t_{amiet}}$ and distance R_a which those include the shear layer delay.

$$\delta_{t_{amiet}} = \frac{r_1}{c_1} + \frac{r_2}{c_0} \tag{96}$$

and

$$R_a = r_1 + r_2 \tag{97}$$

x_i and y_i need to be found, hence the Newton method will be applied which uses the first order Taylor series expansion to find the non linear solutions: x_i and y_i. Those solutions are contained in the functions: F_1 and F_0. As a first step their partial derivative is taken with respect to x_i and y_i. The derivatives of F_0 and F_1 are then assembled to a Jacobian matrix:

$$J(xi, yi) = [\frac{\partial F_0}{\partial x_i}(x_i, y_i), \frac{\partial F_0}{\partial y_i}(x_i, y_i), \frac{\partial F_1}{\partial x_i}(x_i, y_i), \frac{\partial F_1}{\partial y_i}(y_i, y_i)] \tag{98}$$

and the F matrix is:

$$F(xi, yi) = [F_0(x_i, y_i), F_1(x_i, y_i)] \tag{99}$$

To define F, and consequently x_i and y_i, at each iteration k, $F(xi, yi)$ is approximated linearly using the first order Taylor expansion around the current guess x_k.

First order Taylor Series:

$$f(x_{k+1}) \approx f(x_k) + f(x_k)'(x_{k+1} - x_k) = 0 \tag{100}$$

In our case x_k is a guessed vector containing two values, one for x_i and one for y_i. For this reason, the guessed vector is symbolized as: $\mathbf{x_k}$. Applying this to the Amiet's equation case:

$$F(\mathbf{x_k} + \Delta_x) \approx F(\mathbf{x_k}) + J(\mathbf{x_k}) \cdot (\mathbf{x_{k+1}} - \mathbf{x_k}) = 0 \tag{101}$$

$$J(\mathbf{x_k}) \cdot (\mathbf{x_{k+1}} - \mathbf{x_k}) = -F(\mathbf{x_k}) \tag{102}$$

From the form above (equation 102), the equation is solved for $\mathbf{x_{k+1}}$ as seen with equation 103.

$$\rightarrow \mathbf{x_{k+1}} = \mathbf{x_k} - J^{-1}(\mathbf{x_k}) \cdot F(\mathbf{x_k}) \tag{103}$$

Equation 103 is iterated using the index k, and the iteration continues until the norm of $F(\mathbf{x_k})$ becomes sufficiently small so that $F(\mathbf{x_k}) \approx 0$ as initially stated. Only then the method will have converged and therefore only when the method converges: $\mathbf{x_{k+1}} = [x_i, y_i]$.

D Xfoil Turbulent Boundary layer computation

Pohlhausen [6] approximates the dimensionless velocity profile $f(\eta)$ by the following fourth order polynomial:

$$f(\eta) = \frac{U}{U_e}(\eta) = 2\eta - 2\eta^3 + \eta^4 + \Lambda\left(\frac{\eta}{6} - \frac{\eta^2}{2} + \frac{\eta^3}{2} - \frac{\eta^3}{6}\right) \tag{104}$$

$f(\eta)$ should be within 0 and 1, and Λ should be within -12 and 12. In addition, $\eta = \frac{y(t)}{\delta(x)}$, $y(t)$ is the normal distance from the surface of the airfoil and therefore η cant be greater than 1 as that would indicate a location outside the boundary layer.

The displacement thickness δ^* and momentum thickness θ are computed by XFOIL for both the upper and lower surfaces of the airfoil, as shown in Table 7. These values can also be calculated using the von Kármán momentum integral equations (Equations 105 and 106), which are simplified forms that include the dimensionless velocity profile function $f(\eta)$ [10].

$$\delta^* = \delta\left(\frac{3}{10} - \frac{\Lambda}{120}\right) \tag{105}$$

$$\theta = \delta\left(\frac{37}{315} - \frac{\Lambda}{945} + \frac{\Lambda^2}{9072}\right) \tag{106}$$

Combining those two equations for $H = \frac{\delta^*}{\theta}$, Λ which is the Pohlhausen parameter can be determined [9]:

$$H(\Lambda) = \frac{\delta^*}{\theta} = \frac{\frac{3}{10} - \frac{\Lambda}{120}}{\frac{37}{315} - \frac{\Lambda}{945} - \frac{\Lambda^2}{9072}} \tag{107}$$

Therefore, a value for Λ which satisfies the boundary layer shape factor H obtained from XFOIL at 8 % chord ($x = 0.08$) can be determined. With δ^* and θ known from Xfoil (see table 7), and Λ calculated using equation 107 (see Λ value in table 8), the boundary layer thickness δ at 8 % chord position can then be found by solving either of the von Karman momentum integral equations (Equations 105 or 106) for δ. δ is used to define η across the normal distance from the surface of the airfoil. δ value is listed in table 8 for both the upper and lower airfoil sections. The non dimensional velocity $f(\eta)$ is then defined for both the upper and lower airfoil sections, and is then dimensionalized by using equation:

$$u(y) = (0.99U_e)f\left(\frac{y(t)}{\delta(x)}\right) \quad , \quad x = 0.08 \; for \; 8\% \; chordlength \tag{108}$$

Where U_e is the flow velocity at the edge of the boundary layer and when the pressure drops, the flow can accelerate faster than the free stream velocity as seen also with figure 40b.

Table 7: Boundary layer values at 8 % chord computed by XFOIL

Upper airfoil section H value :	2.3616
Upper airfoil section δ^* value :	3.001e-04
Upper airfoil section η value :	0.808
Upper airfoil section U_e value :	67.4847 $[m/s]$
Upper airfoil section θ value :	1.2594e-04
Lower airfoil section H value :	2.3023
Lower airfoil section δ^* value :	2.8512e-04
Lower airfoil section η value :	0.845
Lower airfoil section U_e value :	73.6705 $[m/s]$
Lower airfoil section θ value :	1.2251e-04

Table 8: Pohlhaussen computed values at 8 % chord

Upper airfoil section Λ value :	9.61
Upper airfoil section δ value :	0.001364
Lower airfoil section Λ value :	7.0610
Lower airfoil section δ value :	0.001182

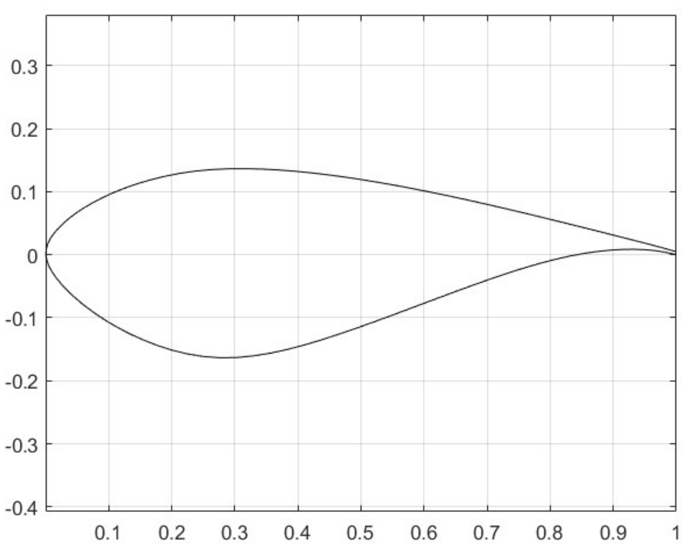

(a)

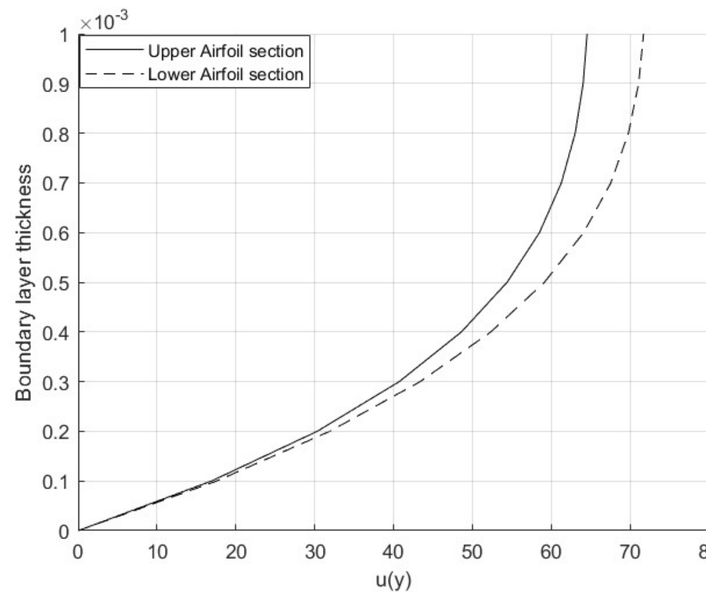

(b)

Figure 40: Figure 40a shows the contour plot of the DU97-W-300 Airfoil with normalized chordlength. Figure 40b shows the velocity distribution along the boundary layer throughout the surface of the airfoil

E Microphone individual coordinates

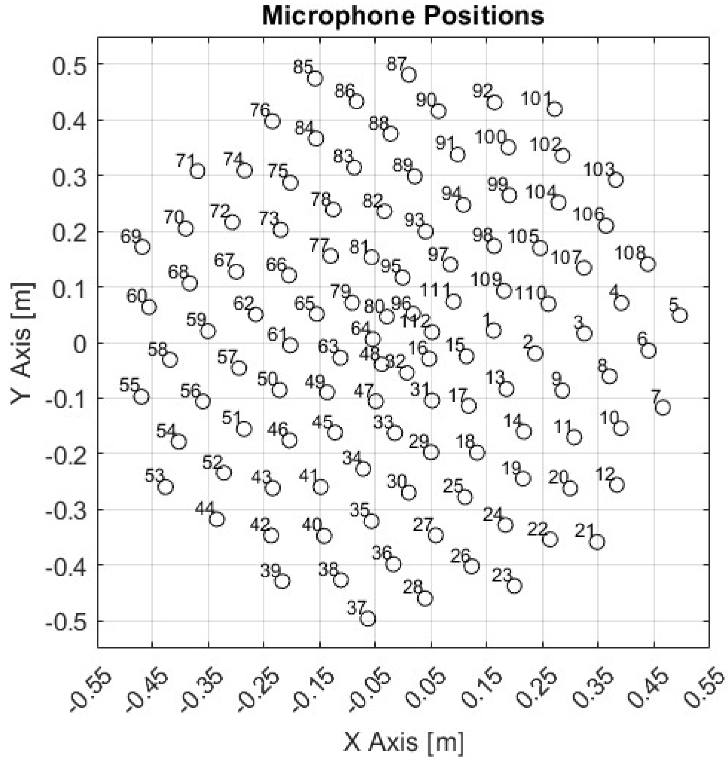

Figure 41: Individual microphone coordinates numbered and plotted

F Monte Carlo simulations, Gaussian distributions

F.1 Analytical case simulations

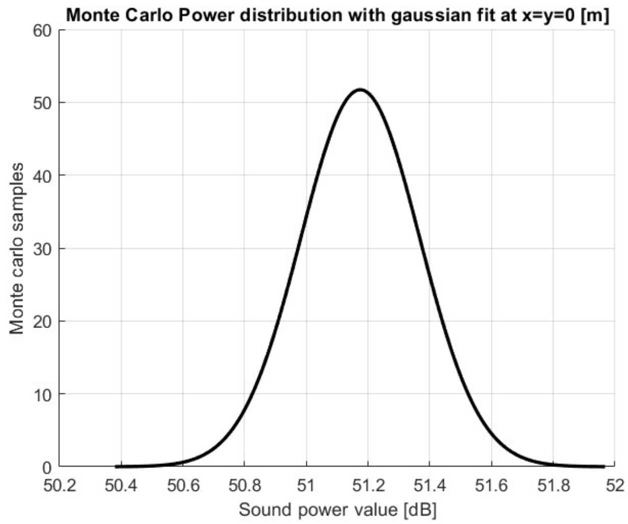

Figure 42: Gaussian distribution of SPL from the multivariate perturbation simulation

Frequency [kHz]	0.5	1	2	3	4	5
std [dB]:	0.08	0.08	0.10	0.10	0.12	0.13
95 % higher bound [dB]:	53.79	54.03	51.37	49.16	47.28	45.56
95 % lower bound [dB]:	53.46	53.69	50.98	48.75	46.82	45.07
Mean [dB]:	53.62	53.86	51.18	48.96	47.05	45.32
Median [dB]:	53.63	53.86	51.17	48.96	47.05	45.31
Nominal [dB]:	53.80	53.99	51.31	49.1	47.2	45.46

Table 9: Statistical summary of the multivariate perturbation simulation across the frequency spectrum at the source location ($x = y = 0$ [m]).

Frequency [kHz]	0.5	1	2	3	4	5
std [dB]:	0.08	0.09	0.11	0.68	0.70	0.70
95 % higher bound [dB]:	55.00	58.83	63.44	63.10	53.87	52.36
95 % lower bound [dB]:	54.67	58.47	62.98	60.43	51.11	49.60
Mean [dB]:	54.84	58.65	63.21	61.77	52.49	50.98
Median [dB]:	54.85	58.65	63.22	61.75	52.45	50.99
Nominal [dB]:	55.02	58.81	63.482	60.96	52.33	51.62

Table 10: Statistical summary of the SPL of the integrated sound power under multivariate perturbations across the frequency spectrum.

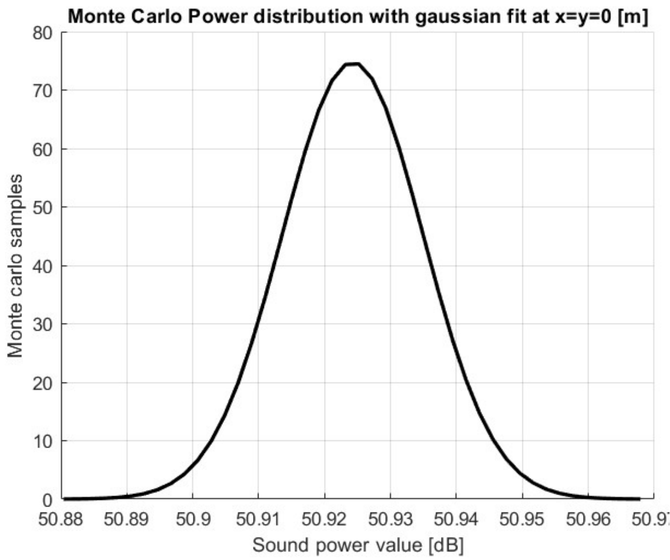

(a)

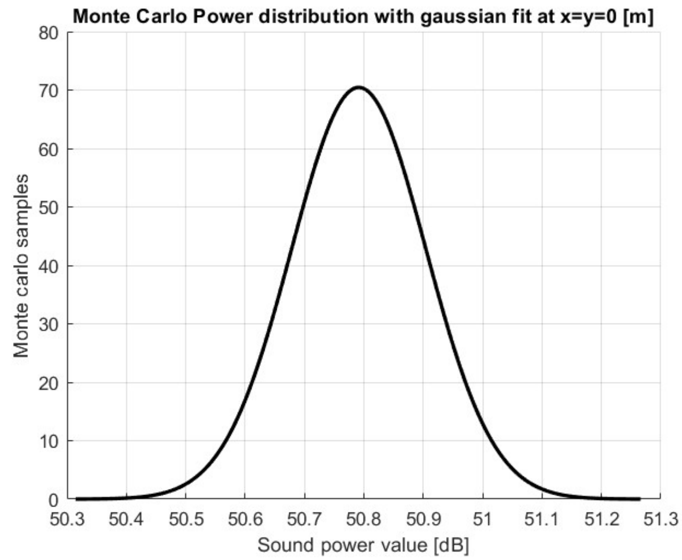

(b)

Figure 43: Figure 43a shows the Gaussian distribution of SPL which results from the phase perturbation simulation with a standard deviation of 1 degree, while figure 43b shows the result for a standard deviation of 10 degree.

Metric [m]	$x = -0.2$	$x = -0.1$	$x = 0$
std [dB]:	0.02	0.01	0.005
95% higher bound [dB]:	45.07	49.93	50.93
95% lower bound [dB]:	44.98	49.89	50.91
Mean [dB]:	45.03	49.91	50.92
Median [dB]:	45.03	49.91	50.92
Nominal [dB]:	45.03	49.91	50.92

(a)

Metric [m]	$x = -0.2$	$x = -0.1$	$x = 0$
std [dB]:	0.23	0.09	0.06
95% higher bound [dB]:	45.34	49.96	50.90
95% lower bound [dB]:	44.43	49.59	50.68
Mean [dB]:	44.88	49.77	50.79
Median [dB]:	44.88	49.78	50.79
Nominal [dB]:	45.03	49.91	50.92

(b)

Table 11: Table 11a presents a statistical summary from the microphone phase perturbation simulation with a standard deviation of 1 degree. Similarly, Table 11b provides a statistical summary from the microphone phase perturbation simulation with a standard deviation of 10 degree.

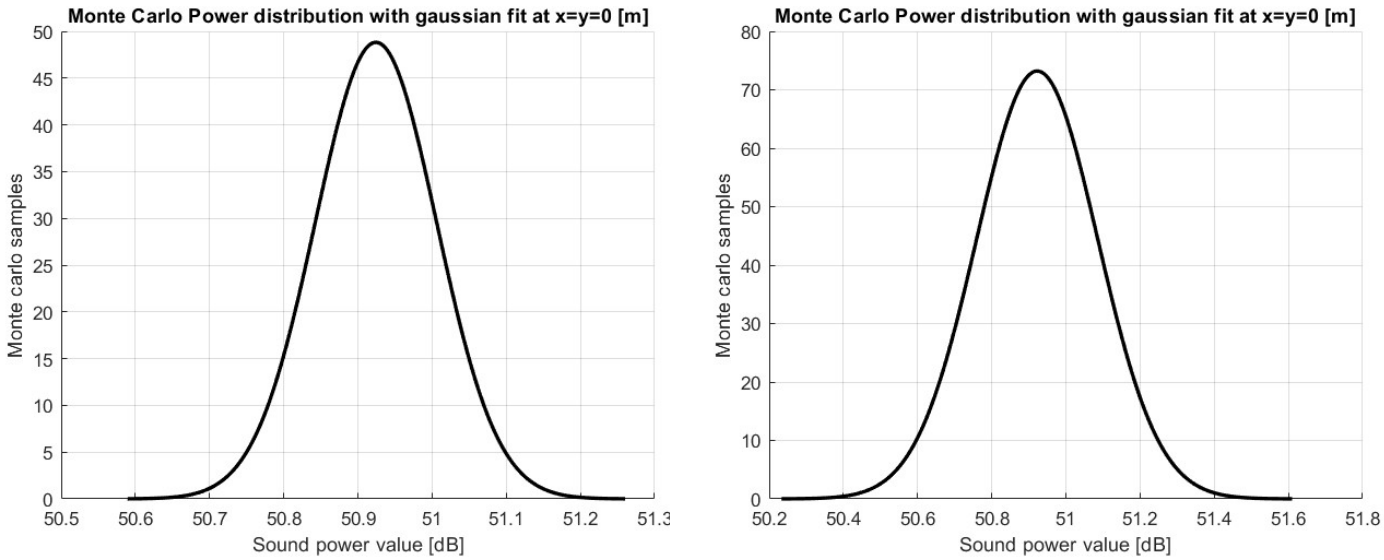

(a) (b)

Figure 44: Figure 44a shows the Gaussian distribution of SPL which results from the microphone sensitivity perturbation simulation with a 5 % standard deviation, while figure 44b shows the result for a standard deviation of 10 %.

Metric [m]	$x = -0.2$	$x = -0.1$	$x = 0$
std [dB]:	0.06	0.04	0.04
95% higher bound [dB]:	45.14	49.99	51.01
95% lower bound [dB]:	44.91	49.83	50.84
Mean [dB]:	45.03	49.91	50.92
Median [dB]:	45.03	49.91	50.92
Nominal [dB]:	45.03	49.91	50.92

(a)

Metric [m]	$x = -0.2$	$x = -0.1$	$x = 0$
std [dB]:	0.12	0.08	0.08
95% higher bound [dB]:	45.25	50.07	51.09
95% lower bound [dB]:	44.79	49.74	50.76
Mean [dB]:	45.02	49.91	50.92
Median [dB]:	45.02	49.90	50.92
Nominal [dB]:	45.03	49.91	50.92

(b)

Table 12: Table 12a presents a statistical summary from the microphone sensitivity perturbation simulation with a standard deviation of 5%. Similarly, Table 12b provides a statistical summary from the microphone sensitivity perturbation simulation with a standard deviation of 10%.

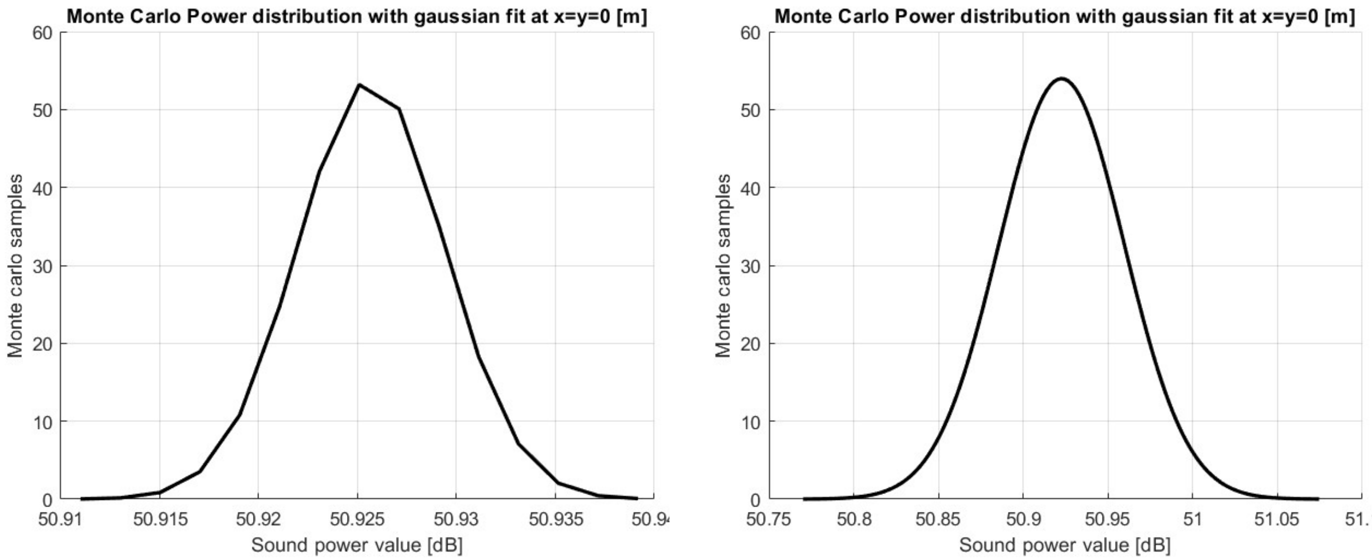

(a) (b)

Figure 45: Figure 45a shows the Gaussian distribution of SPL which results from the microphone location perturbation simulation with a standard deviation of 1 mm, while figure 45b shows the result for a standard deviation of 10 mm.

Metric [m]	$x = -0.2$	$x = -0.1$	$x = 0$
std [dB]:	0.006	0.002	0.002
95% higher bound [dB]:	45.04	49.91	50.93
95% lower bound [dB]:	45.02	49.91	50.92
Mean [dB]:	45.03	49.91	50.92
Median [dB]:	45.03	49.91	50.92
Nominal [dB]:	45.03	49.91	50.92

(a)

Metric [m]	$x = -0.2$	$x = -0.1$	$x = 0$
std [dB]:	0.06	0.02	0.02
95% higher bound [dB]:	45.15	49.95	50.96
95% lower bound [dB]:	45.90	49.86	50.88
Mean [dB]:	45.02	49.91	50.92
Median [dB]:	45.02	49.90	50.92
Nominal [dB]:	45.03	49.91	50.92

(b)

Table 13: Table 13a presents a statistical summary from the microphone location perturbation simulation with a standard deviation of 1mm. Similarly, Table 13b provides a statistical summary from the microphone location perturbation simulation with a standard deviation of 10 mm.

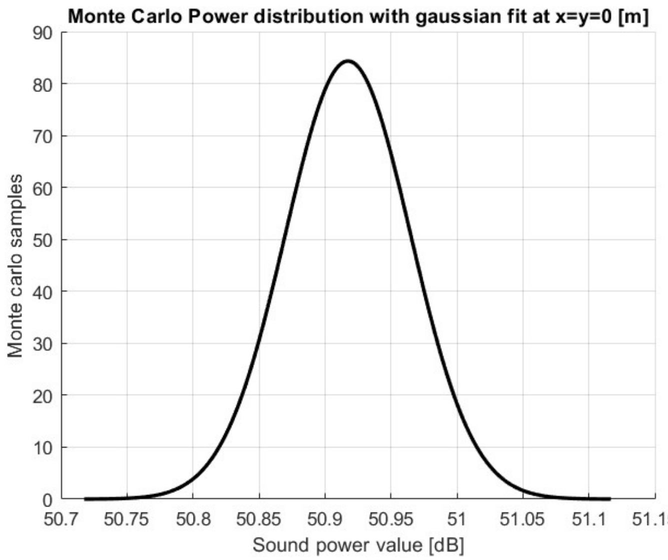

(a)

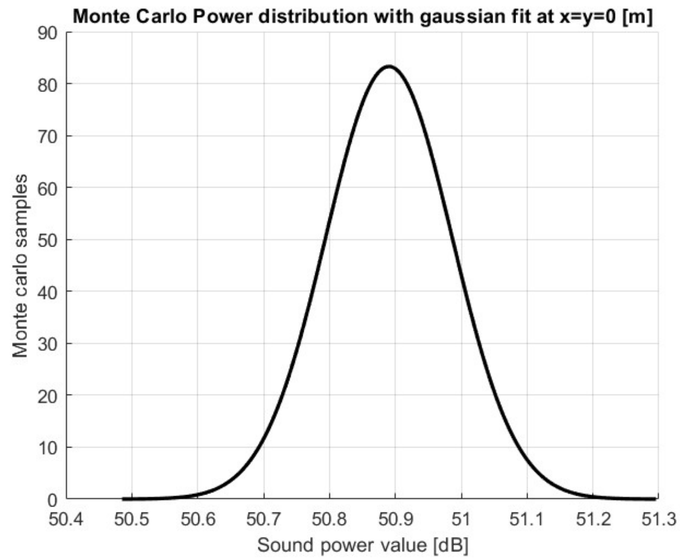

(b)

Figure 46: Figure 46a shows the Gaussian distribution of SPL which results from the array distance perturbation simulation with a standard deviation of 2.5%, while figure 46b shows the result for a standard deviation of 5%.

Metric [m]	$x = -0.2$	$x = -0.1$	$x = 0$
std [dB]:	0.08	0.03	0.02
95% higher bound [dB]:	45.16	49.96	50.96
95% lower bound [dB]:	44.84	49.84	50.87
Mean [dB]:	44.99	49.90	50.92
Median [dB]:	45.00	49.90	50.92
Nominal [dB]:	45.03	49.91	50.92

(a)

Metric [m]	$x = -0.2$	$x = -0.1$	$x = 0$
std [dB]:	0.16	0.06	0.05
95% higher bound [dB]:	45.23	49.98	50.99
95% lower bound [dB]:	44.59	49.74	50.79
Mean [dB]:	44.91	49.86	50.89
Median [dB]:	44.91	49.86	50.89
Nominal [dB]:	45.03	49.91	50.92

(b)

Table 14: Table 14a presents a statistical summary from the array broadband distance perturbation simulation with a standard deviation of 45mm. Similarly, Table 14b provides a statistical summary from the array broadband distance perturbation simulation with a standard deviation of 90mm.

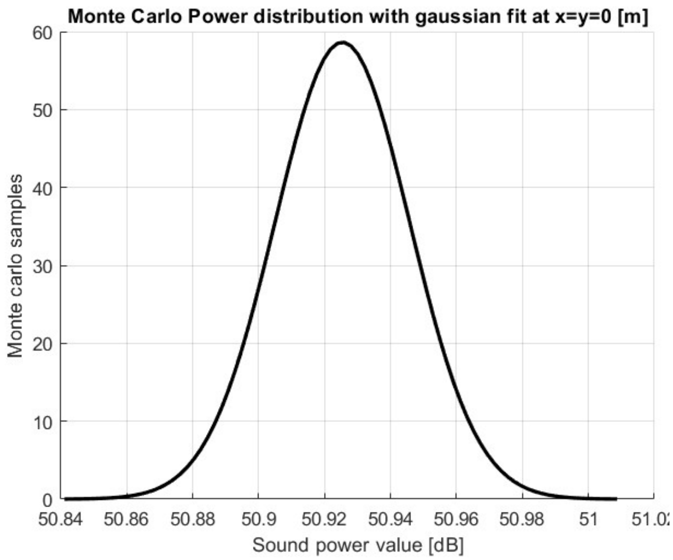

(a)

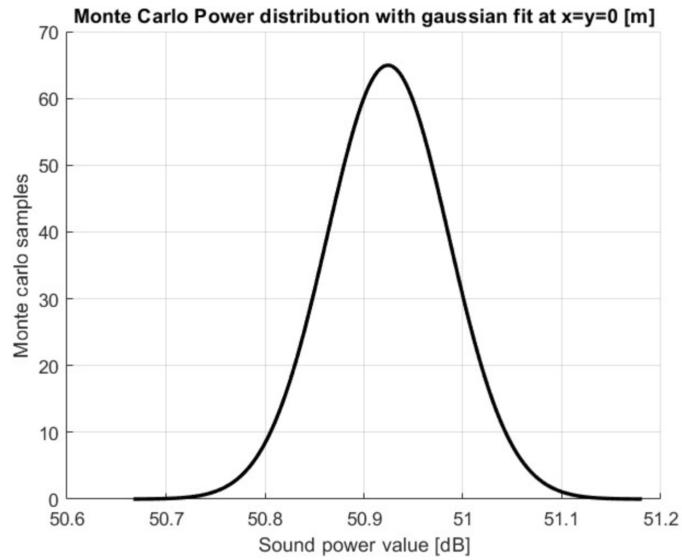

(b)

Figure 47: Figure 47a shows the Gaussian distribution of SPL which results from the temperature perturbation simulation with a standard deviation of 1 kelvin, while figure 47b shows the result for a standard deviation of 3 kelvin.

Metric [m]	$x = -0.2$	$x = -0.1$	$x = 0$
std [dB]:	0.04	0.01	0.01
95% higher bound [dB]:	45.10	49.94	50.94
95% lower bound [dB]:	44.95	49.88	50.90
Mean [dB]:	45.03	49.91	50.92
Median [dB]:	45.03	49.91	50.92
Nominal [dB]:	45.03	49.91	50.92

(a)

Metric [m]	$x = -0.2$	$x = -0.1$	$x = 0$
std [dB]:	0.11	0.04	0.03
95% higher bound [dB]:	45.25	49.99	50.98
95% lower bound [dB]:	44.80	49.82	50.86
Mean [dB]:	45.02	49.91	50.92
Median [dB]:	45.03	49.91	50.92
Nominal [dB]:	45.03	49.91	50.92

(b)

Table 15: Table 15a presents a statistical summary from the temperature perturbation simulation with a standard deviation of 1 kelvin. Similarly, table 15b provides a statistical summary from the temperature perturbation simulation with a standard deviation of 3 kelvin.

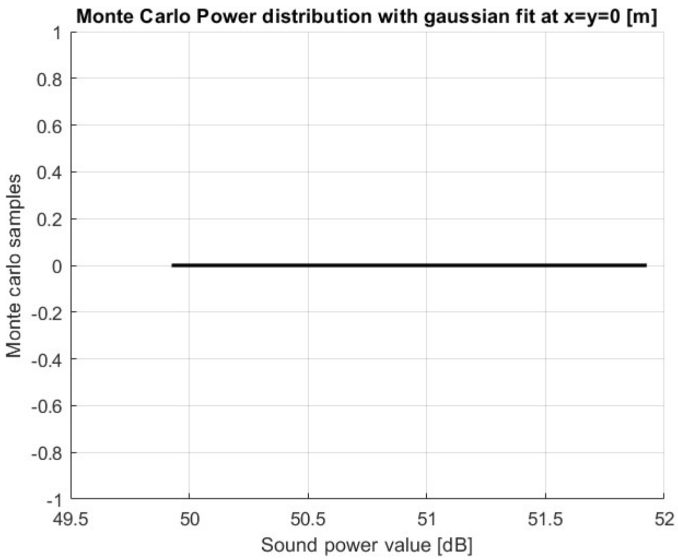

(a)

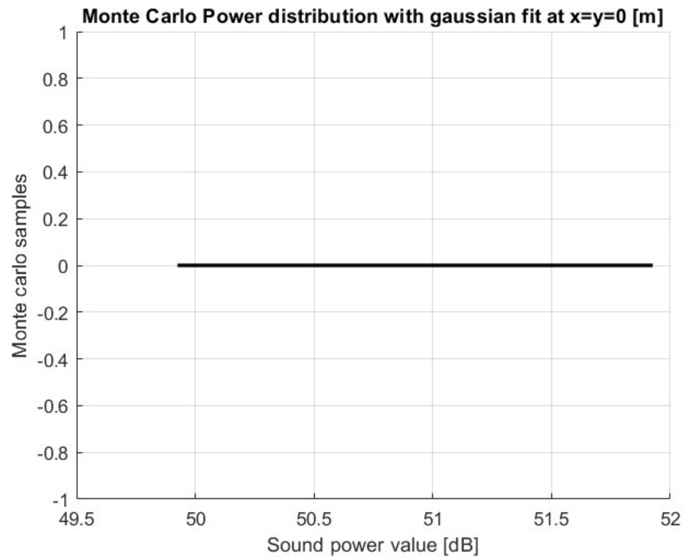

(b)

Figure 48: Figure 48a shows the Gaussian distribution of SPL which results from the CSM perturbation with 500 effective segments, while figure 48b shows the result for 1000 effective segments.

Metric [m]	$x = -0.2$	$x = -0.1$	$x = 0$
std [dB]:	1.59e-5	5.10e-6	4.00e-5
95% higher bound [dB]:	45.03	49.91	50.92
95% lower bound [dB]:	45.03	49.91	50.92
Mean [dB]:	45.03	49.91	50.92
Median [dB]:	45.03	49.91	50.92
Nominal [dB]:	45.03	49.91	50.92

(a)

Metric [m]	$x = -0.2$	$x = -0.1$	$x = 0$
std [dB]:	1.561e-5	5.061e-5	4.047e-5
95% higher bound [dB]:	45.03	49.91	50.92
95% lower bound [dB]:	45.03	49.91	50.92
Mean [dB]:	45.03	49.91	50.92
Median [dB]:	45.03	49.91	50.92
Nominal [dB]:	45.03	49.91	50.92

(b)

Table 16: Table 16a presents a statistical summary from the CSM perturbation simulation with 500 effective segments. Similarly, Table 16b provides a statistical summary from the CSM perturbation simulation with 1000 effective segments.

F.2 Experimental case simulations

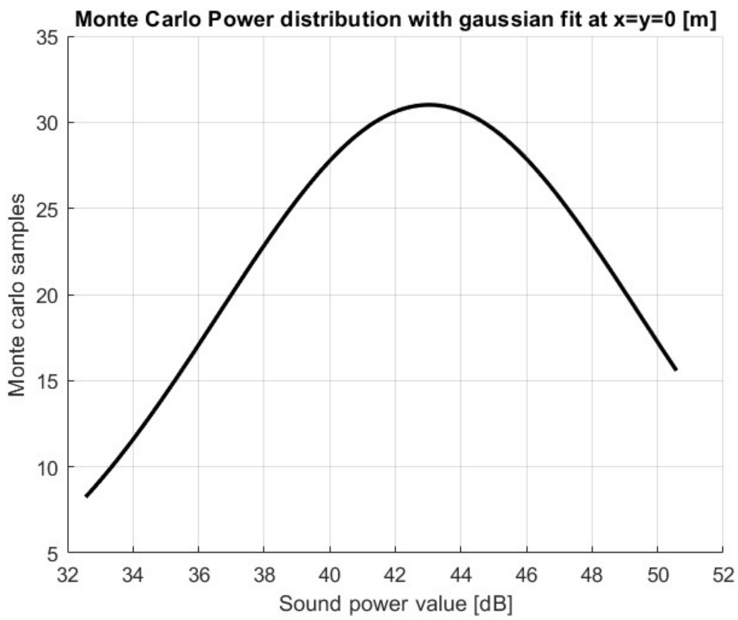

Figure 49: Gaussian distribution of SPL from the multivariate perturbation simulation

Frequency [kHz]	0.5	1	1.5	2	2.5
std [dB]:	0.25	0.86	2.12	3.28	3.05
95 % higher bound [dB]:	72.46	59.89	54.71	49.46	46.91
95 % lower bound [dB]:	71.45	56.50	46.38	36.59	34.93
Mean [dB]:	71.95	58.20	50.55	43.03	40.92
Median [dB]:	71.96	58.26	50.98	43.62	41.26
Nominal [dB]:	72.00	58.65	51.30	43.85	38.18

Table 17: Statistical summary of the multivariate perturbation simulation across the frequency spectrum at the source location ($x = y = 0$ [m]).

Frequency [kHz]	0.5	1	1.5	2	2.5
std [dB]:	0.25	0.74	1.47	2.19	1.74
95 % higher bound [dB]:	73.27	61.10	55.65	50.10	48.37
95 % lower bound [dB]:	72.28	58.18	49.88	41.53	41.57
Mean [dB]:	72.78	59.64	52.76	45.82	44.97
Median [dB]:	72.78	59.69	53.00	45.88	45.02
Nominal [dB]:	72.87	60.11	53.86	45.84	41.58

Table 18: Statistical summary of the SPL of the integrated sound power under multivariate perturbations across the frequency spectrum.

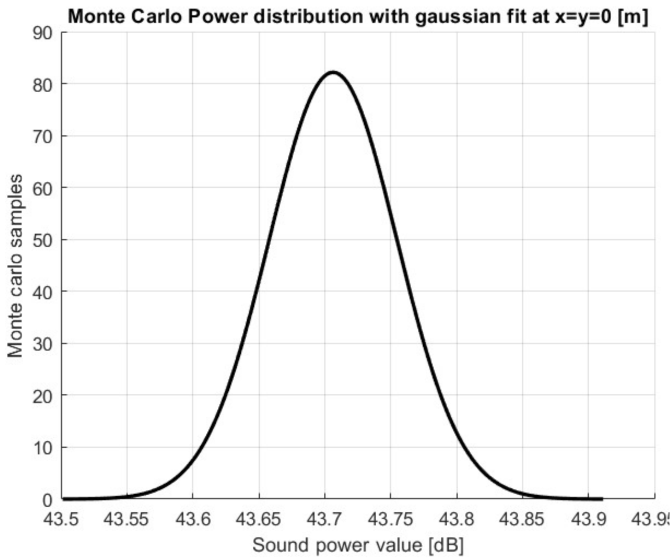

(a)

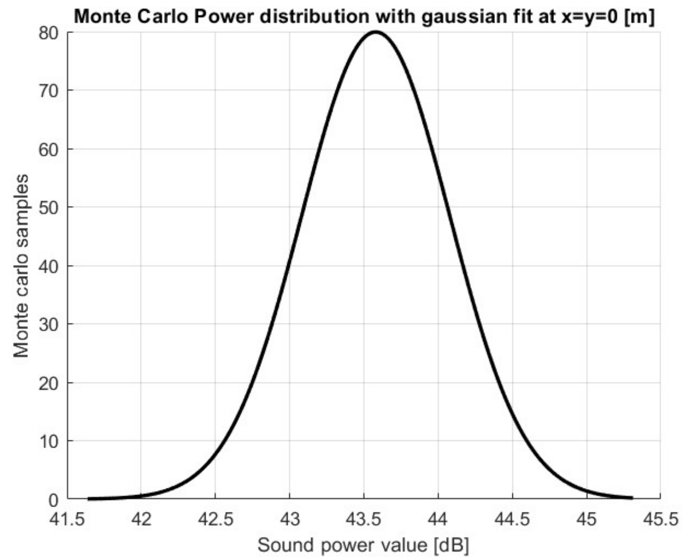

(b)

Figure 50: Figure 50a shows the Gaussian distribution of SPL which results from the phase perturbation simulation with a standard deviation of 1 degree, while figure 50b shows the result for a standard deviation of 10 degree.

Metric [m]	$x = -0.2$	$x = -0.1$	$x = 0$
std [dB]:	0.05	0.03	0.02
95% higher bound [dB]:	40.19	43.17	43.75
95% lower bound [dB]:	39.99	43.06	43.66
Mean [dB]:	40.09	43.11	43.71
Median [dB]:	40.09	43.11	43.71
Nominal [dB]:	40.09	43.11	43.71

(a)

Metric [m]	$x = -0.2$	$x = -0.1$	$x = 0$
std [dB]:	0.54	0.29	0.25
95% higher bound [dB]:	41.01	43.55	44.08
95% lower bound [dB]:	38.88	42.42	43.08
Mean [dB]:	39.94	42.98	43.58
Median [dB]:	39.97	42.99	43.59
Nominal [dB]:	40.09	43.11	43.71

(b)

Table 19: Table 19a presents a statistical summary from the microphone phase perturbation simulation with a standard deviation of 1 degree. Similarly, Table 19b provides a statistical summary from the microphone phase perturbation simulation with a standard deviation of 10 degree.

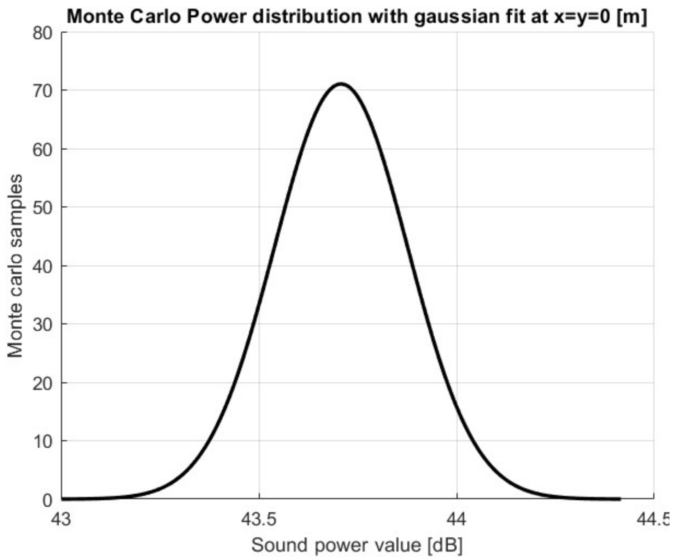

(a)

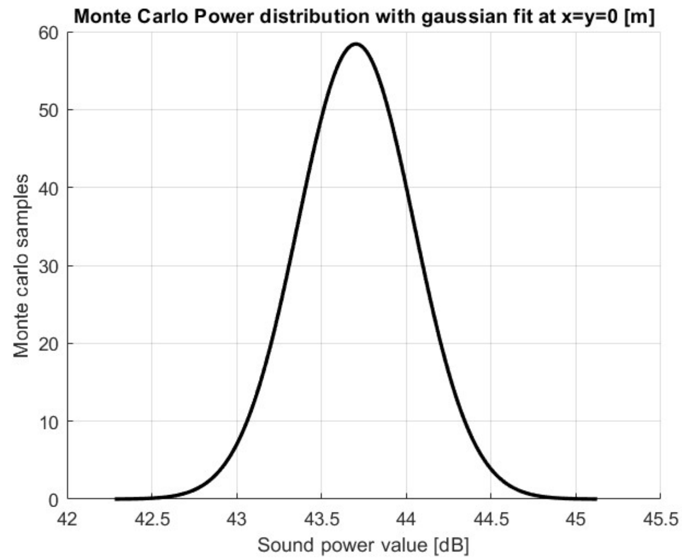

(b)

Figure 51: Figure 51a shows the Gaussian distribution of SPL which results from the microphone sensitivity perturbation simulation with a 5 % standard deviation, while figure 51b shows the result for a standard deviation of 10 %.

Metric [m]	$x = -0.2$	$x = -0.1$	$x = 0$
std [dB]:	0.14	0.09	0.08
95% higher bound [dB]:	40.37	43.30	43.88
95% lower bound [dB]:	39.81	42.93	43.54
Mean [dB]:	40.09	43.11	43.71
Median [dB]:	40.09	43.11	43.70
Nominal [dB]:	40.09	43.11	43.71

(a)

Metric [m]	$x = -0.2$	$x = -0.1$	$x = 0$
std [dB]:	0.29	0.19	0.17
95% higher bound [dB]:	40.64	43.48	44.04
95% lower bound [dB]:	39.52	42.74	43.36
Mean [dB]:	40.08	43.11	43.70
Median [dB]:	40.07	43.10	43.70
Nominal [dB]:	40.091	43.11	43.71

(b)

Table 20: Table 20a presents a statistical summary from the microphone sensitivity perturbation simulation with a standard deviation of 5%. Similarly, Table 20b provides a statistical summary from the microphone sensitivity perturbation simulation with a standard deviation of 10%.

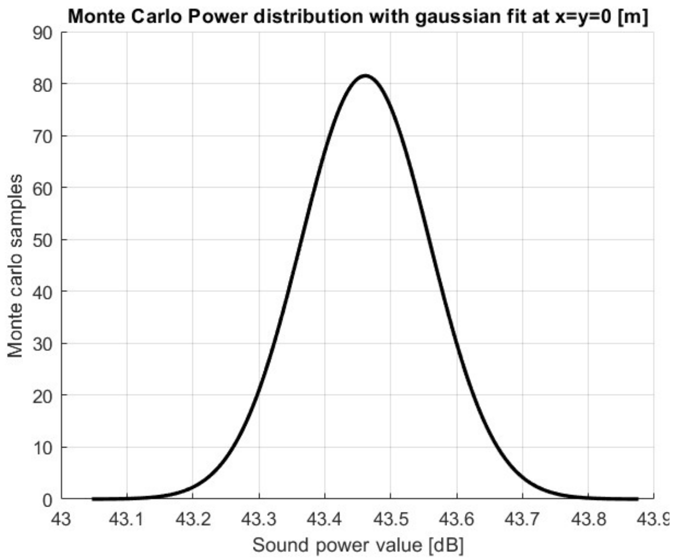

(a)

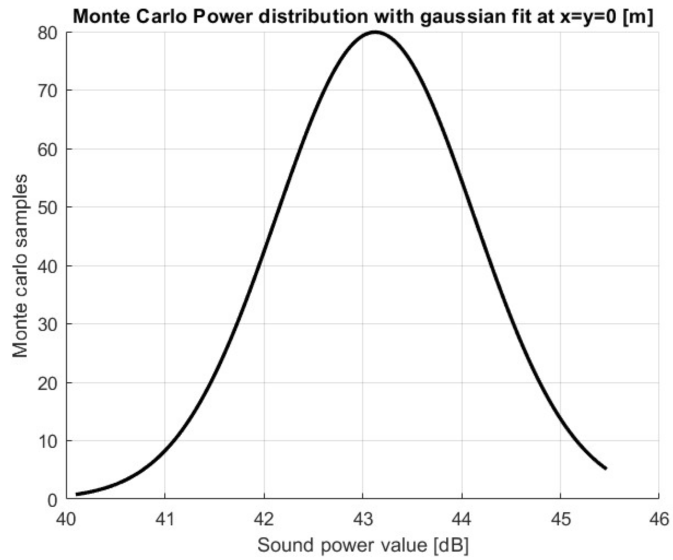

(b)

Figure 52: Figure 52a shows the Gaussian distribution of SPL which results from the microphone location perturbation simulation with a standard deviation of 1 mm, while figure 52b shows the result for a standard deviation of 10 mm.

Metric [m]	$x = -0.2$	$x = -0.1$	$x = 0$
std [dB]:	0.10	0.05	0.05
95% higher bound [dB]:	40.29	43.05	43.56
95% lower bound [dB]:	39.88	42.83	43.36
Mean [dB]:	40.08	42.94	43.46
Median [dB]:	40.09	42.94	43.46
Nominal [dB]:	40.09	43.11	43.71

(a)

Metric [m]	$x = -0.2$	$x = -0.1$	$x = 0$
std [dB]:	0.87	0.55	0.51
95% higher bound [dB]:	42.18	43.81	44.12
95% lower bound [dB]:	38.77	41.67	42.13
Mean [dB]:	40.48	42.74	43.13
Median [dB]:	40.56	42.78	43.17
Nominal [dB]:	40.09	43.11	43.71

(b)

Table 21: Table 21a presents a statistical summary from the microphone location perturbation simulation with a standard deviation of 1mm. Similarly, Table 21b provides a statistical summary from the microphone location perturbation simulation with a standard deviation of 10 mm.

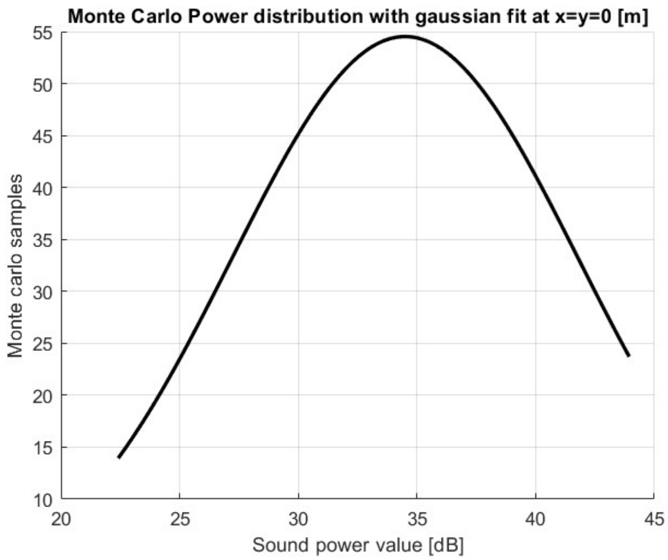

(a)

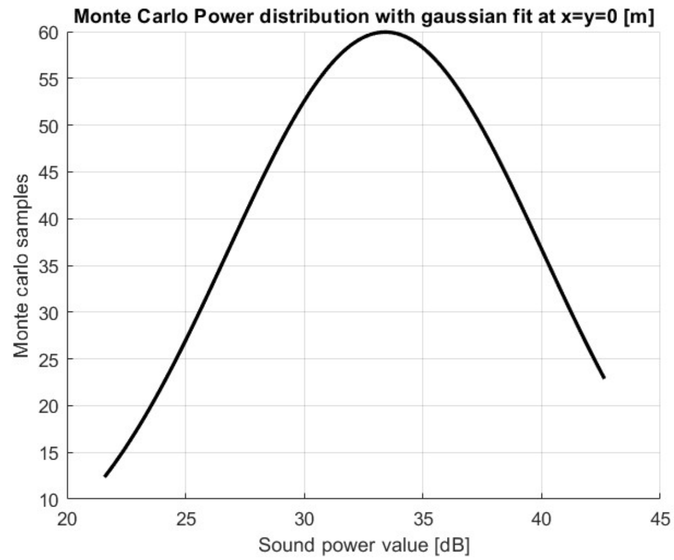

(b)

Figure 53: Figure 53a shows the Gaussian distribution of SPL which results from the array distance perturbation simulation with a standard deviation of 2.5%, while figure 53b shows the result for a standard deviation of 5%.

Metric [m]	$x = -0.2$	$x = -0.1$	$x = 0$
std [dB]:	3.50	3.67	3.73
95% higher bound [dB]:	40.65	41.49	41.81
95% lower bound [dB]:	26.91	27.08	27.18
Mean [dB]:	33.78	34.28	34.50
Median [dB]:	34.11	34.75	35.05
Nominal [dB]:	40.09	43.11	43.71

(a)

Metric [m]	$x = -0.2$	$x = -0.1$	$x = 0$
std [dB]:	3.40	3.43	3.39
95% higher bound [dB]:	40.21	40.03	40.06
95% lower bound [dB]:	26.87	26.59	26.75
Mean [dB]:	33.54	33.31	33.41
Median [dB]:	34.13	33.80	33.98
Nominal [dB]:	40.09	43.11	43.71

(b)

Table 22: Table 22a presents a statistical summary from the array broadband distance perturbation simulation with a standard deviation of 45mm. Similarly, Table 22b provides a statistical summary from the array broadband distance perturbation simulation with a standard deviation of 90mm.

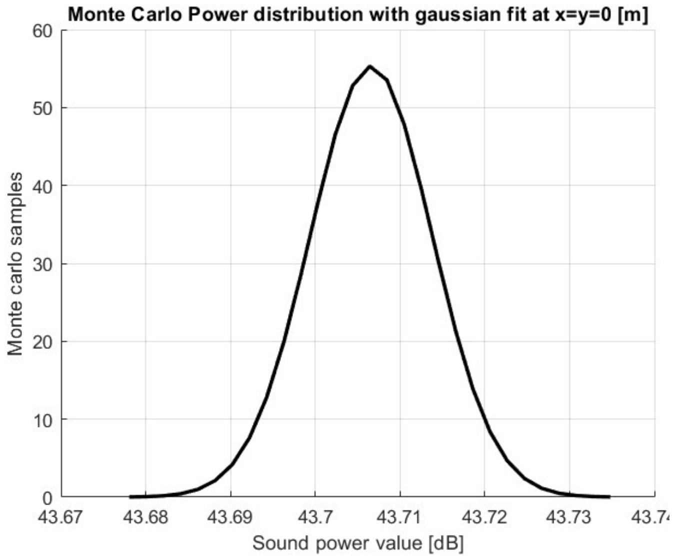

(a)

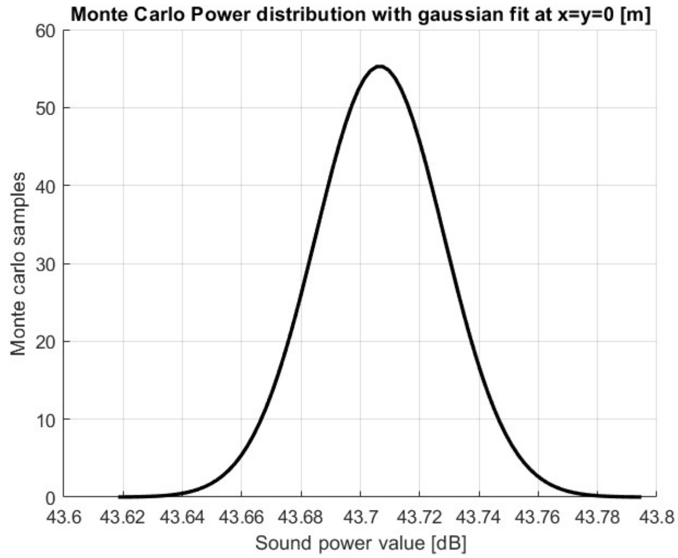

(b)

Figure 54: Figure 54a shows the Gaussian distribution of SPL which results from the temperature perturbation simulation with a standard deviation of 1 kelvin, while figure 54b shows the result for a standard deviation of 3 kelvin.

Metric [m]	$x = -0.2$	$x = -0.1$	$x = 0$
std [dB]:	0.02	0.006	0.004
95% higher bound [dB]:	40.12	43.12	43.71
95% lower bound [dB]:	40.06	43.10	43.70
Mean [dB]:	40.09	43.11	43.71
Median [dB]:	40.09	43.11	43.71
Nominal [dB]:	40.09	43.11	43.71

(a)

Metric [m]	$x = -0.2$	$x = -0.1$	$x = 0$
std [dB]:	0.05	0.02	0.01
95% higher bound [dB]:	40.20	43.15	43.73
95% lower bound [dB]:	39.99	43.08	43.68
Mean [dB]:	40.09	43.11	43.71
Median [dB]:	40.09	43.11	43.70
Nominal [dB]:	40.09	43.11	43.70

(b)

Table 23: Table 23a presents a statistical summary from the temperature perturbation simulation with a standard deviation of 1 kelvin. Similarly, Table 23b provides a statistical summary from the temperature perturbation simulation with a standard deviation of 3 kelvin.

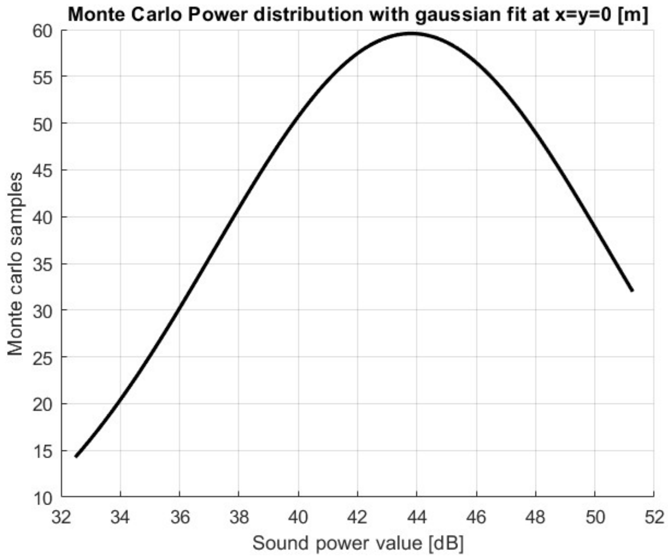

(a)

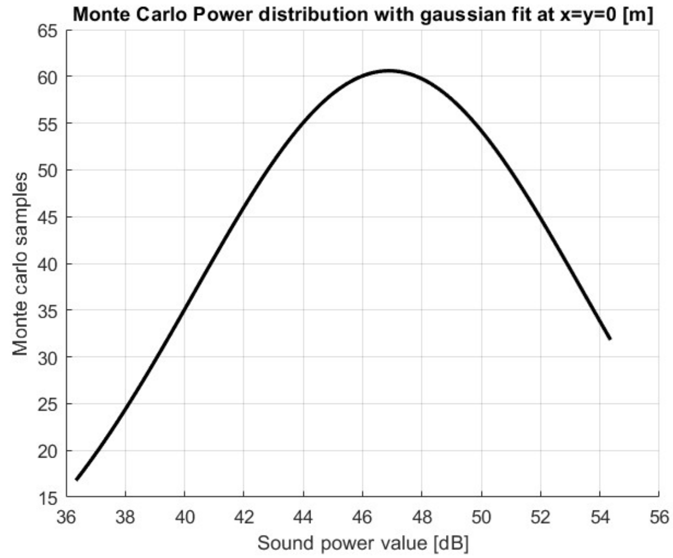

(b)

Figure 55: Figure 55a shows the Gaussian distribution of SPL which results from the CSM perturbation with 500 effective segments, while figure 55b shows the result for 1000 effective segments.

Metric [m]	$x = -0.2$	$x = -0.1$	$x = 0$
std [dB]:	3.30	3.35	3.42
95% higher bound [dB]:	49.39	50.24	50.50
95% lower bound [dB]:	36.46	37.12	37.11
Mean [dB]:	42.92	43.68	43.80
Median [dB]:	43.29	44.23	44.37
Nominal [dB]:	40.09	43.11	43.71

(a)

Metric [m]	$x = -0.2$	$x = -0.1$	$x = 0$
std [dB]:	3.28	3.41	3.36
95% higher bound [dB]:	52.47	53.29	53.47
95% lower bound [dB]:	39.61	39.92	40.30
Mean [dB]:	46.04	46.61	46.89
Median [dB]:	46.42	47.13	47.39
Nominal [dB]:	40.09	43.11	43.71

(b)

Table 24: Table 24a presents a statistical summary from the CSM perturbation simulation with 500 effective segments. Similarly, Table 24b provides a statistical summary from the CSM perturbation simulation with 1000 effective segments.

Acknowledgments

I want to thank all the people who have supported me throughout this research. I dedicate this work to my grandmother, Elli Zaverdas, and my grandfather, Nikos Katsantonis, who are watching over me from the sky. Finally, I want to express my deepest gratitude to my Father, Mother, Twin Brother, and to my Girlfriend for their great support and encouragement. Their belief in me helped to push me every single day over the past nine months to work harder and stay focused on making this possible.